Doctoral Thesis

Synthesis of Two- and Three-Dimensional Carbon-Based Materials and Their Applications

Seo-Yoon Bae

Department of Energy Engineering

Graduate School of UNIST

2016

Synthesis of Two- and Three-Dimensional Carbon-Based Materials and Their Applications

Seo-Yoon Bae

Department of Energy Engineering

Graduate School of UNIST

Synthesis of Two- and Three-Dimensional Carbon-Based Materials and Their Applications

A thesis
submitted to the Graduate School of UNIST
in partial fulfillment of the
requirements for the degree of
Doctor of Philosophy

Seo-Yoon Bae

01. 13. 2016

Approved by

Advisor
Jong-Beom Baek

Synthesis of Two- and Three-Dimensional Carbon-Based Materials and Their Applications

Seo-Yoon Bae

This certifies that the dissertation of Seo-Yoon Bae is approved.

01. 13. 2016

signature

Advisor: Prof. Jong-Beom Baek

signature

Prof. Myoung Soo Lah: Thesis Committee Member #1

signature

Prof. Hoi Ri Moon: Thesis Committee Member #2

signature

Prof. Dong Wook Chang: Thesis Committee Member #3

signature

Prof. Hu Young Jeong: Thesis Committee Member #4;

Abstract

Due to abundant carbon reserves (15th most element in the earth's crust) and light weight advantage, carbon based materials have been studied to replace rare and expansive inorganic materials in energy materials. Since the discovery of graphene, two dimensional structure, in 2004, two dimensional carbon materials have attracted the attention of researchers from around the globe. Keeping in view the importance of carbon materials, we first produced edge-selective functionalized graphene (EFG) for the production of large-area uniform graphene film for transparent and flexible electrode and transistor by top-down method from graphite to graphene. The resultant graphene films show ambipolar transport properties with sheet resistances of 0.52-3.11 kΩ/sq at 63-90% optical transmittance. EFG allows solution processing methods for the scalable production of electrically conductive, optically transparent, and mechanically robust flexible graphene films for use in practice. Secondary, we designed and synthesized two dimensional benzimidazole based network polymer for counter electrode in dye-sensitized solar cell (DSSC) to replace platinum. We confirm the effect of thermal annealing and additives of iron from T-HPBI for electrocatalytic activity from the symmetrical dummy cell with two identical electrodes. Furthermore, we also designed and synthesized three-dimensional polymer through solid-state reaction without catalyst at low-temperature for solid sorbent for CO_2 capture. The reaction is triggered by metastable crystal lattice energy below its crystal melting temperature. The driving force for the reaction is systematically studied with single-crystal X-ray diffraction and differential scanning calorimetry.

Contents

List of Figures

image of "edge-on" view, suggestive of edge functionalization at higher magnification from square in panel a. Scale bar is 20 nm.

Figure 1.5. (a) XRD diffraction patterns: pristine graphite (red); PPA/P_2O_5-treated graphite (blue); EFG (hot pink). The relative peak intensity of PPA/P_2O_5-treated graphite was stronger than that of 'pristine' graphite. The result implied that PPA/P_2O_5 did not damaged but purified graphite. On the other hand, unlike graphene oxide (GO), the peak intensity of EFG is approximately 10% to that of pristine graphite and the interlayer distance of EFG remains almost constant, indicating that basal plane is not functionalized. The intensity was approximately 90 % decreased due to the delaminating of graphite into a few layers of graphite (few-layer graphene sheets). The degree of exfoliation from pristine graphite into EFG in solid state could be approximately estimated. XPS spectra of pristine graphite and EFG: (b) full spectra; (c) carbon survey; (d) oxygen survey. EFG shows no additional oxygen content beyond the value calculated on the basis of yield from the edge-selective functionalization.

Figure 1.6. (a) EFG in a various solvents for dispersibility test: (top row) as soon as EFG dispersed; (bottom row) after one week (1, H_2O; 2, MeOH; 3, EtOH; 4, acetic acid; 5, toluene; 6, DMAc; 7, heptane; 8, acetone; 9, benzene; 10, dichloromethane; 11, THF; 12, pyridine; 13, NMP). Among them, DMAc, dichloromethane, THF and NMP show stronger Tyndall effect, indicating that larger amount of EFG stays in supernatant. (b) EFG solution (ca. 0.8 mg/mL) in dichloromethane. The color of EFG solution is dark black, implying that EFG maintains original conjugated structure at basal plane. On the other hand, the color of GO solution is light transparent yellow. (c) 'Pristine' graphite dispersed in NMP (0.1 mg/mL). It was sediment after a day, leaving clear solution. It is an indication that pristine graphite dispersion in NMP is not thermodynamically stable (kinetic dispersion).

Figure 1.7. Calculated model geometry of EFG that shows polar interaction (14.7 kJ/mol) between carbonyl group at the edge and dichloromethane. The phenyl ring on EB group is vertically aligned to the graphene plane.

Figure 1.8. (a) Schematic presentation of as-cast EFG film on SiO_2 surface. (b) Schematic presentation of heat-treated EFG (HEFG) film on SiO_2 surface. (c) SEM image of as-cast EFG film drop-coated on SiO_2 surface from dichloromethane solution and then dried. (d) SEM image obtained on the surface of HEFG film at 600 ℃ under argon atmosphere for 3 h. The peeled-off area was scratched with a sharp metal tip, and this allowed discriminating the very smooth film from the SiO_2 surface substrate. (e) Edge-on SEM image of peeled-off area of HEFG film. Scale bar is 300 nm. (f) SEM image of the fracture surface of HEFG film on a SiO_2 surface. Scale bar is 300 nm. (g) TEM image of the surface of HEFG film. (h) TEM image focused on junction of HEFG at high magnification. (i) Selected area electron diffraction (SAED) pattern of HEFG film.

Figure 1.9. (a) Schematic presentation of EFG deposition on an SiO_2 surface with diluted solution. (b) SEM image obtained from diluted EFG solution on an SiO_2 surface. (c) Size distribution of EFG by using image analyzer software. Grain size distribution is in the range of 0.2-2.2 μm and average size is 0.97 μm.

Figure 1.10. (a) Raman spectra obtained along the red line from left to right on confocal optical microscopy image in (b). (b) Confocal D and G band optical microscopy image of EFG on silicon substrate. The image cannot resolve clear edge boundary due to the fluorescent nature of EFG.

Figure 1.11. (a)-(f) AFM images (top-left: 3D and top-right: height) and topographic height profiles (bottom) obtained from EFG dispersion in dichloromethane and coated on an SiO_2 surface. In all cases, the EFG with approximately ~1 μm width and a few-microns length could be clearly observed. The

maximum heights of few-layer graphene sheet(s) are in the range of 1.2-3.0 nm. The most importantly, the sharp height profiles at the edges of EFG are due to the presence of EBA grafts, which are covalently attached to sp^2 bonded C-H sites on the edges of graphite.

Figure 1.12. (a) AFM image of scratched HEFG film on a SiO_2 surface. (b) SEM image of scratched HEFG film debris. (c) AFM image of scratched HEFG film and height profile obtained across the lines. (d) SEM image obtained from HEFG film, showing uniformity of the film surface.

Figure 1.13. (a) Photograph of HEFG film on SiO_2 surface; (b) photograph of PMMA spin-coated on HEFG (HEFG/PMMA) film by spin coating; (c) freestanding HEFG/PMMA after SiO_2 surface eching; (d) 2 in. by 2 in. HEFG on PET (HEFG/PET) film.

Figure 1.14. (a) Optical transmittance with respect to wavelength; (b) transmittance vs sheet resistance curve.

Figure 1.15. I-Vg curve of a field-effect transistor of HEFG film. The measurement was carried out in vacuum and bias voltage between source and drain electrodes was 0.1 V. The inset is an optical microscopy image of the device with the channel length of 4 μm.

Figure 2.1. Schematic presentation for the formation of H-HPBI in PPA. The condensation reaction between hexaaminobenzene and tricarboxylic was conducted in PPA medium.

Figure 2.2. Schematic presentation for the formation of H-HPBI in PPA. The condensation reaction between hexaaminobenzene and tricarboxylic was conducted in PPA medium.

Figure 2.3. Photographs of reaction of HPBIs in PPA. (a-d) H-HPBI: (a) Hexaaminobenzene in PPA at room temperature, (b) Changing of color from peach to blue and addition of trimesic acid after removing HCl, (c) Reaction flask at the final stage of reaction with high viscosity, (d) Black powder after post-treatment. (e-h) T-HPBI: (e) Tetraaminobenzene in PPA at room temperature, (f) Changing of color from white to orange and addition of trimesic acid after removing HCl, (g) Reaction flask at the final stage of reaction with high viscosity, (h) Brown powder after post-treatment.

Figure 2.4. The mechanism of benzimidazole compounds in polyphosphoric acid.

Figure 2.5. (a) FT-IR (KBr pellet) spectra of HPBIs confirming the formation of benzimidazole linkage. (b) XPS survey spectra of HPBIs. (c) Powder XRD diffraction patterns of HPBIs.

Figure 2.6. (a-c) High resolution XPS spectra of H-HPBI: (a) C1s, (b) N1s and (c) O1s. (d-f) High resolution XPS spectra of T-HPBI: (a) C1s, (b) N1s and (c) O1s.

Figure 2.7. Repeating units of HPBIs: (a) H-HPBI and (b) T-HPBI

Figure 2.8. TGA thermograms of HPBIs in air (a) and nitrogen (b) atmosphere. Which was measured after pre-annealing to 200 ℃ (20 ℃/min) to remove trapped water in materials and the heating rate is 10 ℃/min.

Figure 2.9. SEM images of HPBIs: (a-c) H-HPBI and (d-f) T-HPBI. Scale bars are 1 μm.

Figure 3.4. (a) Schematic representation of the reaction from as-grown HEA single crystals to polyHEA (gray: carbon, red: oxygen, blue: hydrogen). The dotted line represents lattice energy in crystal of as-grown HEA single crystal. DSC thermograms of samples obtained with a heating rate of 10 ℃ min^{-1}: (b) 1st heating scan of ground HEA crystals after grinding of as-grown bulk HEA single crystals. Inset is photograph of ground HEA crystals. (c) 1st heating scan of as-grown bulk HEA single crystals. Inset is photograph of bulk HEA single crystals. (d) Energy diagrams of as-grown bulk and ground HEA single crystals based on DSC thermograms. ΔH_0: Lattice energy in bulk and ground HEA single crystals. In case of ground HEA crystals with high surface area, the lattice is completely decomposed but the lattice of bulk HEA crystals is partially decomposed during heating with 10 ℃/min. Consequentially, lattice energy between ground and bulk HEA crystal is different at the moment of reaction due to kinetics difference according to difference of crystal size. ΔH_1: Included lattice energy in bulk HEA crystals at the time of reaction. In this step, the lattice in crystal absorb kinetic energy from trapped acetone and water during heating. ($\Delta H_1 > 0$, ΔH_1: enthalpy change in state 1) ΔH_2: Absorbed lattice energy in bulk HEA crystals is released as heat energy and kinetic energy of molecules ($\Delta H_2 < 0$). ΔH_3: Cyclotrimerization of entire ethynyl groups in HEA occur ($\Delta H_3 < 0$, $\alpha = 1$, α: conversion ratio of ethynyl groups in HEA). ΔH_4: Cyclotrimerization of neighboring ethynyl groups in HEA occur ($\Delta H_4 < 0$, $0 < \alpha < 1$, $|\Delta H_4| << |\Delta H_3|$). ΔH_B is enthalpy change of as-grown bulk HEA crystals ($\Delta H_B = \Delta H_2 + (\Delta H_0 - \Delta H_2) + \Delta H_3$, $|\Delta H_B| = 2.34|\Delta H_G|$). ΔH_G is enthalpy change of ground HEA crystals ($\Delta H_G = \Delta H_0 + \Delta H_4$). Inset is DSC thermograms of as-grown bulk (pink) and ground (green) HEA single crystals showing amount of exothermic heat with respect to time.

Figure 3.5. DSC thermograms obtained with a ramping rate of 10 ℃/min under nitrogen: (a) Ground HEA crystals and (b) Triethynylbenzene.

Figure 3.6. (a) Ball and Stick style diagram of crystallographic asymmetric unit of the HEA from single-crystal X-ray diffraction. (gray: HEA, red: acetone, blue: water) (d) Experimentally determined and simulated powder XRD patterns of HEA.

Figure 3.7. (a-f) Photographs of reaction from HEA to polyHEA at different timeframes. The images were captured by high-speed camera. (g) SEM images of polyHEA (Scale bar is 2 μm). (h) TEM image of polyHEA.

Figure 3.8. NMR spectra of as-grown bulk HEA crystal and ground HEA crystal from grinding bulk HEA crystal. After grinding, the amount of acetone is decreased but the quantity of water is increased due to large surface area of ground HEA crystal for trapping the moisture in air. 400 MHz 1H NMR of bulk HEA crystals (CDCl3, δ = ppm): 1.538 (0.87, H2O), 2.171 (0.59, Acetone), 3.260 (2.61, ≡C-H), 5.341 (1.00, CH), 7.508 (2.85, Ar-H). 400 MHz 1H NMR of ground HEA crystals (CDCl3, δ = ppm): 1.537 (1.45, H2O), 2.171 (0.19, Acetone), 3.259 (2.56, ≡C-H), 5.342 (1.00, CH), 7.508 (2.68, Ar-H).

Figure 3.9. Photographs of reactions: (a) Morphology change of as-grown bulk HEA single crystals by heat-gun according to time in argon atmosphere. Heating rate of heat-gun is 23 ℃/s. (b) Morphology change of as-grown bulk HEA single crystals in oil-bath according to time in argon atmosphere. Heating rate of oil-bath is 1.4 ℃/s. (c) Morphology change of ground HEA crystals by heat-gun according to time in argon atmosphere. Heating rate of heat-gun is 23 ℃/s. (d) Morphology change of ground HEA crystals in oil-bath according to time in argon atmosphere. Heating rate of oil-bath is 1.4 ℃/s.

Figure 3.10. Energy diagrams of as-grown bulk HEA single crystals with different heating rate by heat-gun and in oil bath. ΔH_{H1}: Lattice energy of as-grown bulk HEA at the moment of reaction by heat gun. ΔH_{O1}: Lattice energy of as-grown bulk HEA crystals at the moment of reaction in oil bath. In oil bath

for gradually heating, lattice in crystal is slowly decomposed and lattice energy reduced. ($\Delta H_{H1} > \Delta H_{O1}$) ΔH_{H2}: Absorbed lattice energy (ΔH_{H1}) is released to heat energy and kinetic energy of molecules. ΔH_{O2}: Absorbed lattice energy (ΔH_{O1}) is released to heat energy and kinetic energy of molecules. ($|\Delta H_{H2}| > |\Delta H_{O2}|$) ΔH_{H3} and ΔH_{O3}: Cyclotrimerization of entire ethynyl group in HEA occur ($\alpha = 1$, α: conversion ratio of ethynyl group in HEA, $\Delta H_{H3} = \Delta H_{O3}$). Inserts are photographs of the moment of cyclotrimerization of reaction by heat-gun and in oil bath. Crucial difference of released energy between by heat-gun (instant heating) and in oil bath (gradually heating) is lattice energy difference between ΔH_{H2} and ΔH_{O2} at the moment of trigger reaction.

Figure 3.11. The reaction of as-grown bulk HEA single crystals under gradually elevated temperature in oil bath: (**a**) Photograph and (**b**) SEM image. The reaction of as-grown bulk HEA single crystals under suddenly elevated temperature using heat-gun. (**c**) Photograph and (**d**) SEM image. (Scale bar: 10 μm) The morphology of heating in oil-bath is smaller pore size and denser than the morphology of heating by heat-gun.

Figure 3.12. (a) DSC thermogram of 1st heating scan of as-grown bulk HEA single crystals obtained with a heating rate of 2 ℃/min. In case of a heating rate of 2 ℃/min, the reaction temperature is lower than that of 10 ℃/min about 12 ℃ because the measurement with heating rate of 2 ℃/min give enough time to absorb heat. Same phenomenon can be found in literature (10 ℃/min *vs.* 1 ℃/ min in TGA).[39] (b) DSC thermograms of as-grown bulk HEA single crystals showing amount of exothermic heat with respect to time according to different heating rate.

Figure 3.13. (a) Solid-state ^{13}C NMR spectrum of polyHEA. (b) FT-IR (KBr pellet) spectra of polyHEA (blue) and HEA (red). Inset is a magnification of the black dot rectangle area. XPS survey spectra of polyHEA: (c) full spectrum, (d) C1s and (e) O1s.

List of Tables

Abbreviations

1. AFM: Atomic force microscopy
2. BDL: Below detection limit
3. BET: Brunauer-Emmett-Teller
4. CE: Counter electrode
5. CVD: Chemical vapor deposition
6. DMAc: N,N-dimethylacetamide
7. DSC: Differential scanning calorimetry
8. DSSCs: Dye-sensitized solar cells
9. EA: Elemental analyse
10. EB: 4-Ethylbenzoyl
11. EBA: 4-Ethylbenzoic acid
12. EC: Equivalent circuit
13. EDS: Energy dispersive X-ray spectroscopy
14. EFG: Edge-selective functionalization of graphite
15. EIS: Electrochemical impedance spectroscopy
16. e-spray: Electrostatic spray
17. Fe@HT-HPBI: Heat-treated Fe@T-HPBI
18. Fe@T-HPBI: T-HPBI contained 0.01 wt% iron
19. FE-SEM: Field emission scanning electron microscopy
20. FE-TEM: Field emission transmission electron microscope
21. FT-IR: Fourier transform infrared
22. FTO: Fluorine-doped SnO2

23. GO: Graphene oxide
24. HBA: 2,3,6,7,14,15-Hexabromo-9,10-dihydro-9,10-[1,2]benzenoanthracene
25. HEA: 2,3,6,7,14,15-Hexaethynyl-9,10-dihydro-9,10-[1,2]benzenoanthracene
26. HEFG: Heat-treated EFG
27. H-HPBI: Holypolybenzimidazole synthesized from hexaaminobenzene
28. HMSA: 2,3,6,7,14,15-Hexakis((trimethylsilyl)ethynyl)-9,10-dihydro-9,10-[1,2] benzenoanthracene
29. HPBI: Holypolybenzimidazole
30. HT-HPBI: Heat-treated T-HPBI
31. ITO: Indium tin oxide
32. NMP: N-methyl-2-pyrrolidone
33. P_2O_5: Phosphorus pentoxide
34. PCE: Power conversion efficiency
35. PET: Poly(ethylene terephthalate)
36. PMMA: Poly(methylmethaacrylate)
37. polyHEA: Polymerized HEA
38. PPA: Polyphosphoric acid
39. Pt: Platinum
40. rGO: Reduced graphene oxide
41. SAED: Selected area electron diffraction
42. SiO_2: Silicon oxide
43. TAB: 1,2,4,5-Tetraaminobenzene
44. T_d: Degradation temperature
45. TGA: Themogravimetric analysis
46. THF: Tetrahydrofuran
47. T-HPBI: Holypolybenzimidazole synthesized from tetraaminobenzene

48. TMC: Transition metal compound
49. VASP: Vienna Ab Initio Simulation Package
50. XPS: X-ray photoelectron spectroscopy
51. XRD: X-ray diffraction

I. Large-Area Graphene Films by Simple Solution Casting of Edge-Selectively Functionalized Graphite

1.1 Abstract

We report edge-selective functionalization of graphite (EFG) for the production of large-area uniform graphene films by simply solution-casting EFG dispersions in dichloromethane on silicon oxide substrates, followed by annealing. The resultant graphene films show ambipolar transport properties with sheet resistances of 0.52-3.11 kΩ/sq at 63-90% optical transmittance. EFG allows solution processing methods for the scalable production of electrically conductive, optically transparent, and mechanically robust flexible graphene films for use in practice.

1.2 Introduction

Exfoliation of graphite, including into individual layers (graphene), is of great interest due to the exceptional mechanical strength,[1] thermal conductivity,[2] and electronic properties[3] characteristics of graphene platelets. As a result, graphene is attractive for a wide range of potential applications in composites,[4] energy related systems,[5] sensors,[6] and others.[7-9] Graphene is a promising material for replacing indium tin oxide (ITO) in transparent conductive flat panels.[10] Currently, ITO is widely used as the transparent electrode in flat panel displays, because it has a relatively high electrical conductivity and optical transmittance with a very good stability to moisture and harsh environmental conditions.[11] However, indium is expensive and has a limited reserve in nature. In addition, ITO is not appropriate for flexible display devices due to limitations in its mechanical and optical properties.

Recently, Hong et al. have demonstrated the feasibility for the use of large-area graphene films as the transparent conductor in flexible polymer film-based flat panel electronics.[12] These graphene films were grown on nickel (Ni)[10] and copper (Cu)[12-13] substrates at 1000 ℃ under a reduced pressure by chemical vapor deposition (CVD) process and then transferred onto polymer films. Unfortunately, these methods are not sufficiently cost and time effective to be commercially viable for mass production.[14] To meet commercial demands, new materials or processing methods would be essential. In this regard, graphene oxide (GO) has been investigated as a chemical alternative for mass production of graphene films by solution-based processes.[15] However, GO has poor quality and requires reduction, which has a limited conversion to reduced graphene oxide (rGO).[16] Hence, the original graphene structure from GO cannot be efficiently restored.

Here, we report the formation of large area, flexible, conductive, and transparent graphene films via a simple solution casting of exfoliated platelets from edge-selectively functionalized graphite (EFG). The newly developed edge-selective functionalization method enabled us to achieve exfoliation of "pristine" graphite into individual graphene and few-layer graphene platelets in a scalable and simple manner.[17] For example, most of the 4-substituted benzoic acids can be used as "molecular wedges" and covalently attached to the edge of graphite. The edge groups on graphite are mainly sp^2-bonded C-H groups, a reactive site for "direct" Friedel-Crafts acylation in polyphosphoric acid (PPA)/phosphorus pentoxide (P_2O_5).

1.3 Materials and Instrumentation

All reagents and solvents were purchased from Aldrich Chemical Inc., and used as received, unless otherwise mentioned. 4-Ethylbenzoic acid as a reactive molecular wedge was purified by recrystallization from heptanes (mp = 112-113 ℃). Graphite (99.9%purity, stock no. 1250HT, CAS no. 7782-42-5, Lot no.1250-100907) was obtained from Nanostructured & Amorphous Materials Inc., USA, and used as received.

Raman spectra were taken with HeNe laser (532 nm) as the excitation source by using combined AFM and confocal Raman microscope (Alpha 300S, WITec, Germany). Themogravimetric analysis (TGA) was conducted in air and nitrogen atmospheres at a heating rate of 10 and 1 C/min using a TA Hi-Res TGA 2950 thermogravimetric analyzer. The field emission scanning electron microscopy (FE-SEM) used in this work was LEO 1530FE and FEI NanoSem 200. The field emission transmission electron microscope (FE-TEM) employed in this work was a FEI Tecnai G2 F30 S-Twin. The operating voltage was 200 kV. The samples were prepared by dispersion in N-methyl-2-pyrrolidone (NMP). X-ray photoelectron spectroscopy (XPS) was performed with Thermo Fisher K-alpha. Elemental analysis (EA) was conducted with Thermo Scientific Flash 2000. Atomic force microscopy (AFM) analysis was conducted with Veeco Multimode V. X-ray diffraction (XRD) patterns were recorded with Rigaku D/Max2500/PC. The fieldeffect transistor was fabricated by transferring the HEFG film on prepatterned electrodes, which were defined on SiO_2/Si (300 nm thick SiO_2 layer on a highly doped p-type Si(100)) substrates by addressing Cr (5 nm)/Au (20 nm) electrodes by using a conventional photolithography (photoresist: AZ7210). The channel length was 4 μm. I-Vg curve of a field-effect transistor was obtained by using a semiconductor analyzer (Keithley 4200). The measurement was carried out in vacuum and bias voltage of 0.1 V between source and drain electrodes.

1.4 Experiment Section

1.4.1 Procedure for the Functionalization of Graphite with 4-Ethylbenzoic Acid in Polyphosphoric Acid (PPA)/Phosphorus Pentoxide (P_2O_5).

Graphite was functionalized with 4-ethylbenzoic acid (EBA) in a 250 mL resin flask equipped with a high-torque mechanical stirrer and the nitrogen inlet and outlet. Into the flask, EBA (0.5 g, 16.65 mmol), graphite-powder (0.5 g), PPA (83% P_2O_5 assay: 100.0 g) and P_2O_5 (25 g) were placed and stirred under dry nitrogen purge at 130 ℃ for 72 h. The initial black mixture became lighter and viscous as the functionalization onto graphite progressed. At the end of the reaction, the color of the mixture turned dark green, and water was added into the flask. The resulting tanned brown precipitate was collected by suction filtration, Soxhlet extracted with water for 3 days to completely remove reaction medium, and then with methanol for 3 more days to get rid of unreacted EBA and low molar mass impurities. Finally, the sample was freeze-dried under reduced pressure (0.5 mmHg) at 120 ℃ for 72 h to give 0.58 g (60% yield) of tanned brown powder (**Figure 1.2b**). Anal. Calcd. for $C_{71.57}H_9O$: C, 97.17%; H, 1.02%; O, 1.81%. Found: C, 95.71%; H, 1.03%; O, 1.59%.

The amount of EFG dispersed in each solvent was calculated as described as follows: (1) a given amount of EFG was dispersed in the solvent with magnetic stirring; (2) the dispersion was allowed to sediment overnight (12 h); (3) it was then centrifuged and the centrifuged portion and supernatant were then separated; (4) solvent was removed from the centrifuged portion; (5) the residual solid from the centrifuged portion was weighed; (6) the amount of exfoliated EFG in the supernatant was estimated by subtracting the residual weight from the centrifuged portion from the original EFG weight added in the first step.

1.4.2 Computation

The Vienna Ab Initio Simulation Package (VASP) with the Perdew-Burke-Ernzerhof version of the gradient corrected functional was used. The projector-augmented-wave pseudopotential was employed for the atomic potential, and the plane-wave basis set was used with the energy cutoff of 400 eV.[18]

Here, a graphene fragment is modeled by the zigzag-edged graphene ribbon. The binding strength between dichloromethane solvent molecules and the ethyl-benzoyl terminal groups was calculated as shown in **Figure 1.7**. The adsorption strength of the solvent molecules was found to be 14.7 kJ/mol. During delamination, the van der Waals interaction between neighboring layers in graphite competes with the attraction force between the edge-functional groups and solvent molecules. The van der Waals attraction between solvent molecules and the surface of graphene also contributes to the energetics of delamination.

1.5 Results and Discussion

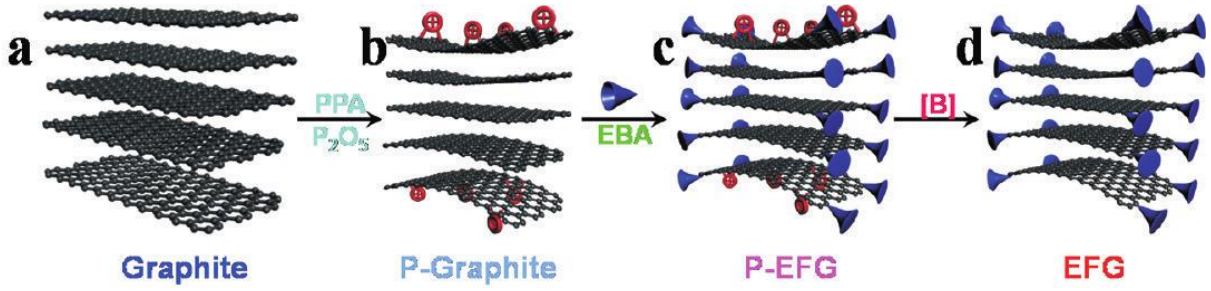

Figure 1.1. (a-d) Functionalization of 4-ethylbenzoic acid (EBA) onto the edge of "pristine" graphite in polyphosphoric acid (PPA)/phosphorus pentoxide (P_2O_5) to produce edge-selectively functionalized graphite (EFG). P-graphite, P-EFG and [B] stand for protonated graphite, protonated EFG, and base treatment, respectively.

From the elemental analysis (**Table 1.1**), the possible available sp^2 bonded C-H sites at the edges could be calculated to be about one per every 45 carbons. Hence, a sufficient number of "wedge" molecules necessary for exfoliation can be attached around graphite by treating it with 4-ethylbenzoic acid (EBA) in the reaction medium PPA/ P_2O_5 at 130 ℃ (**Figure 1.1a-c**). The EFG was then completely worked-up and analyzed (**Figure 1.1d** and **Figure 1.2a**) prior to dispersing in organic solvents.

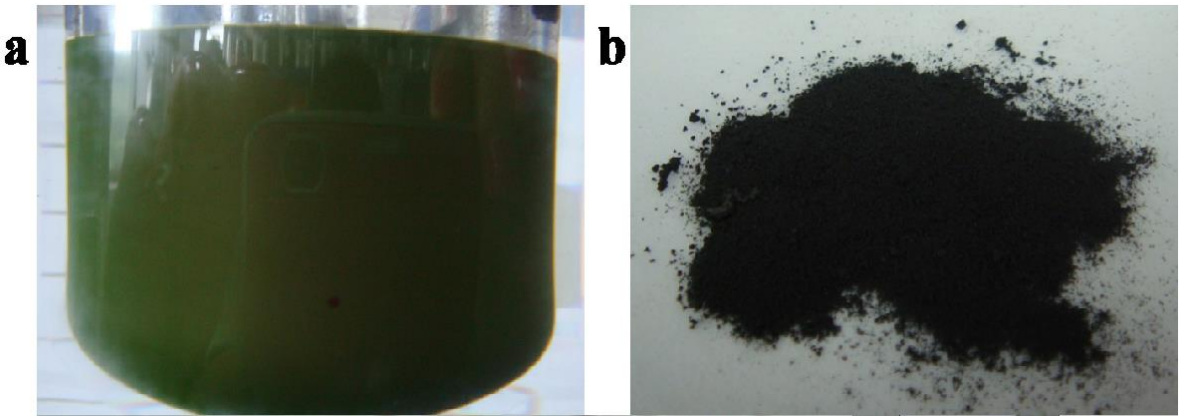

Figure 1.2. Digital images: (a) reaction flask at the final stage of reaction between 'pristine' graphite and EBA in PPA/P_2O_5 medium at 130 ℃. The reaction mixture emits green color due to edge-

functionalization and uniform dispersion. (b) Isolated EFG in solid state after complete work-up.

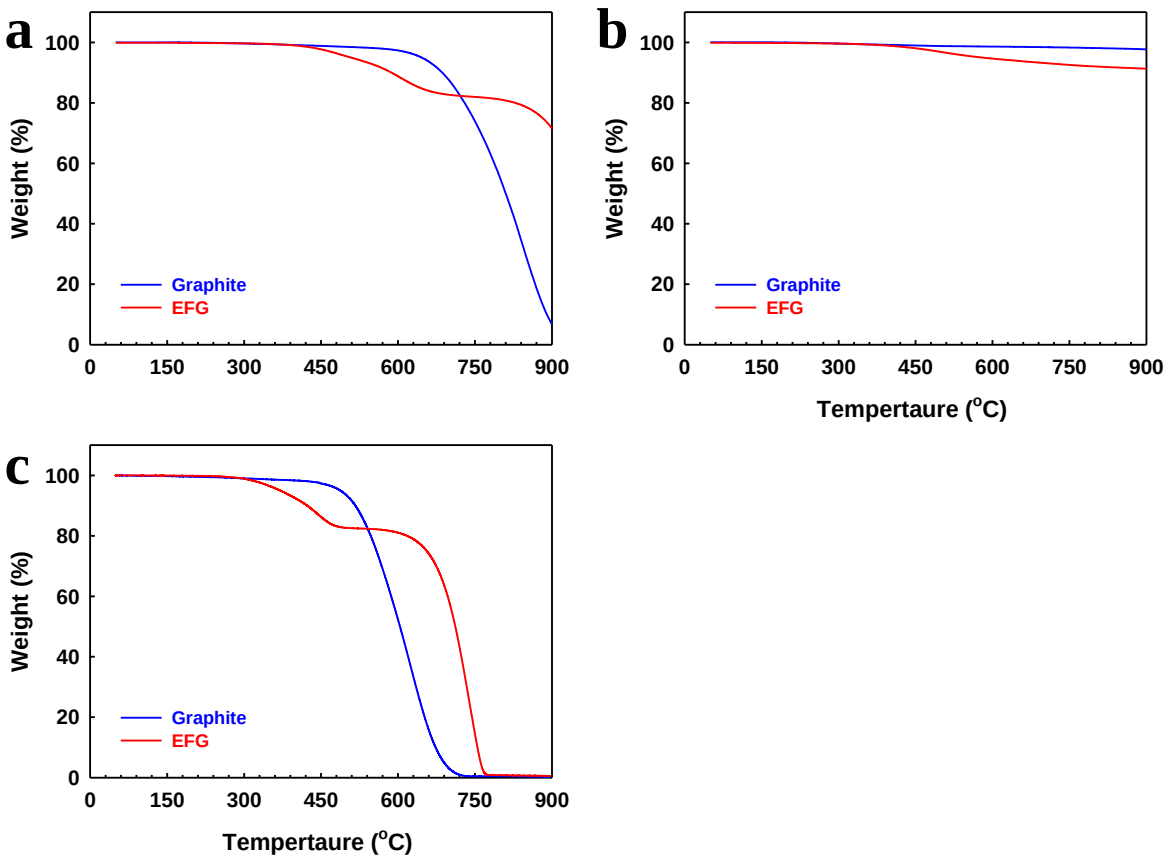

Figure 1.3. TGA thermograms obtained with (a) a heating rate of 10 ℃/min in air, (b) a heating rate of 10 ℃/min in nitrogen, (c) a heating rate of 1 ℃/min in air. Both 'pristine' graphite and EFG obtained with a heating rate of 1 ℃/min displayed very similar thermograms to those obtained with a ramp rate of 10 ℃/min. Both samples had degradation temperatures downshifted approximately 180 ℃ and the stepwise weight loss of EFG was evident leaving almost the same amount of char yield (15 wt %) at the plateau region at 540 ℃. Hence, the higher thermo-oxidative stability of EFG after charring of the EBA moiety is not due to blocking of the oxidant (kinetic effect).

Thermogravimetric analysis (TGA) was used to determine the amount of EBA grafted onto the graphite. As can be seen in **Figure 1.3a**, graphite is thermooxidatively stable up to 650 ℃ in air, while the EFG shows stepwise weight losses. We assign the first weight loss at about 400 ℃, which continues until about 720 ℃, to the EBA moiety being thermally "stripped off". Hence, the degree of functionalization can be quantified by the weight loss of EFG up to about 720 ℃ and it is approximately 15 wt %. The degree of functionalization was 76.5% of the available sp^2 bonded C-H sites. The temperature where the second weight loss starts is approximately 850 ℃, or 200 ℃ higher than that of pristine graphite (650 ℃), suggesting that carbon cations, anions, and/or radicals generated during heating (charring) of the 4-ethylbenzoyl (EB) moiety at the edges of EFG provide an in situ carbon feedstock for "healing" inherent defects on graphite and/or "edge-welding" (cross-linking) graphene platelets.[19] The high char yield (91 wt %) of EFG at 720 ℃ in a nitrogen atmosphere (**Figure 1.3b**) was much higher than that in dry air (85 wt %), suggesting that the formation of large-area graphene films could be possible via solution casting and subsequent "edge welding" by thermal annealing at elevated temperature.

To evaluate whether the "char" at the edges blocks oxidants from accessing the interior of the EFG, and hence keeps the graphitic plane structure intact, TGA thermograms were obtained with a ramp rate of 1 ℃/min (**Figure 1.3c**). The thermograms for both graphite and EFG were very similar to those obtained with a ramp rate of 10 ℃/min (see **Figure 1.3a**). Both samples had degradation temperatures down-shifted approximately 180 ℃ and the stepwise weight loss of mass in the EFG was evident leaving almost the same amount of char yield (15 wt %) at the plateau region at 540 ℃. Hence, the higher thermo-oxidative stability of EFG after charring of the EBA moiety is not due to blocking of the oxidant (kinetic effect). More importantly, the fact that there is no weight loss around 100-200 ℃, characteristic of interlamellar water in graphite oxide due to its hygroscopic nature,[20] strongly suggests that the graphite is not oxidized during the edge-functionalization in a mild PPA/P_2O_5 medium.

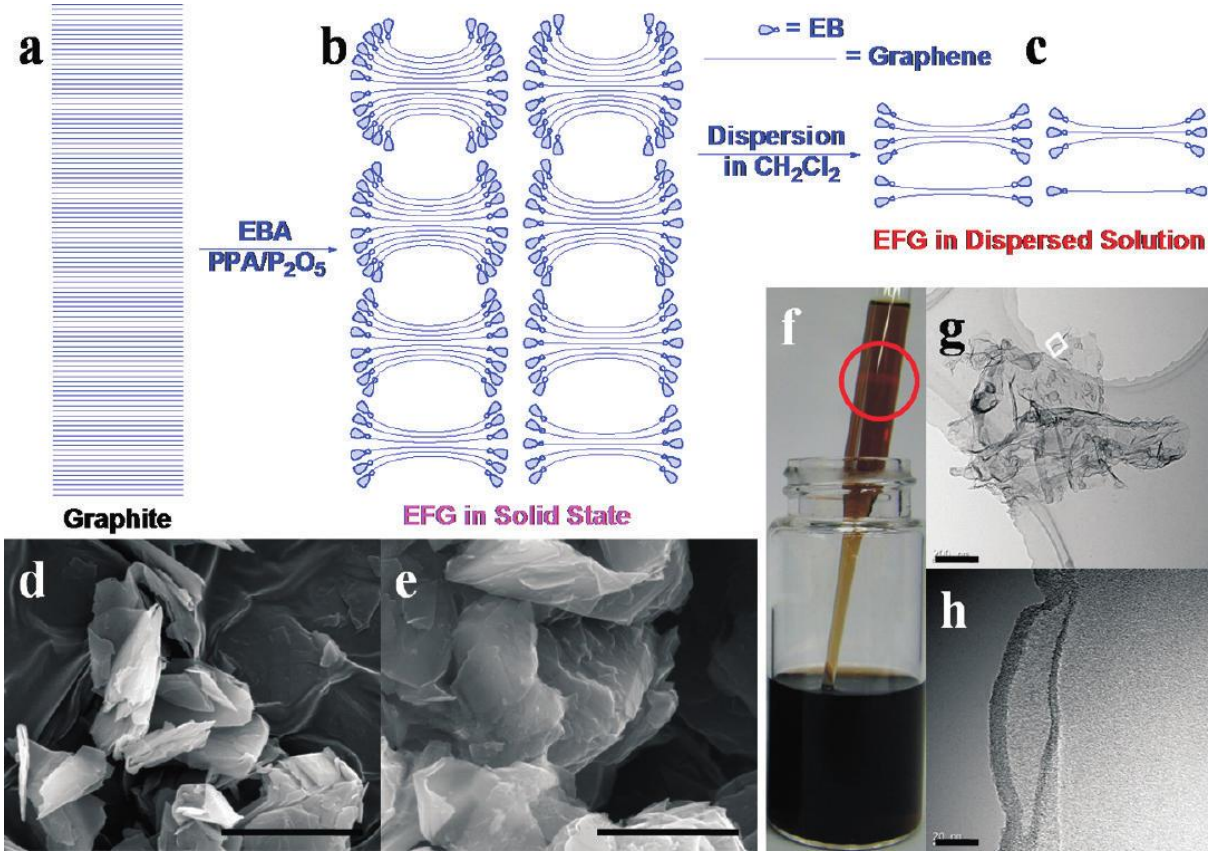

Figure 1.4. (a) Schematic presentation of pristine graphite. (b) Idealized structure of edge-functionalized graphite (EFG) in solid state. (c) Idealized structure of EFG in dispersed solution. (d) SEM image of pristine graphite (50000 x). (e) SEM image of EFG (50000 x) in solid state. Scale bars are 2 μm. (f) EFG-dispersed solution in dichloromethane. (g) TEM image of EFG on holey carbon grid. The thin EFG platelets are wrinkled and crumpled due to their flexibility. Scale bar is 200 nm. (h) TEM image of "edge-on" view, suggestive of edge functionalization at higher magnification from square in panel a. Scale bar is 20 nm.

The covalently linked edge groups provide steric repulsion to open pristine graphite edges (**Figure 1.4a**) and thus, the EFG in solid state should consist of many stacks of graphene layers as schematically shown in **Figure 1.4b**. The partially edge-delaminated EFG allows efficient solvent penetration for the further exfoliation of EFG into few-layer graphene platelets and graphene in solution (**Figure 1.4c**). Wide-angle X-ray diffraction (XRD) patterns (**Figure 1.5a**) were applied to the same amount of pristine graphite, PPA/P_2O_5-treated graphite, and EFG to estimate the degree of exfoliation and functionalization of the basal plane; the peak intensity of EFG in the solid state is 10% of that of the precursor graphite with almost the same peak location at 26.58° (0.333 Å), indicating the efficient dispersion in solvents through a kind of "unzipping" mechanism schematically shown in **Figure** 1.4a-c and without basal plane functionalization. In a control experiment, graphite was exposed to the same reaction conditions used for the EFG synthesis in the absence of EBA to test if the reaction medium PPA/P_2O_5 could damage (oxidize) graphite. XRD patterns show that the peak intensity of PPA-treated graphite is stronger than that of graphite with the same peak location at 26.50° (0.334 Å) (**Figure 1.5a**). This implies that the PPA-treated graphite is not chemically altered but has increased crystallinity by selectively etching off of amorphous carbon attached to the surface of graphite. Further evidence for the structural integrity of the EFG basal plane region comes from the elemental (EA, **Table 1.1**) and XPS (**Figure 1.5b-d**) analyses, which revealed that there was no additional oxygen content beyond the value calculated on the basis of yield from the edge selective functionalization. Scanning electron microscopy (SEM) of the precursor graphite powder shows that its surfaces are "clean and smooth" (**Figure 1.4d**), while the SEM image of bulk EFG in solid state shows fuzzier surfaces (**Figure 1.4e**), indicating that the attachment of EBA expanded the edge. Indeed, EFG is an ideal precursor (**Figure 1.4b**) for further exfoliation into scalable and high-quality individual graphene and few layer graphene platelets (**Figure 1.4c**).

Table 1.1. Elemental analysis for 'pristine' graphite and EFG

Sample	Formula		C (%)	H (%)	O (%)	C/H	C/O
Pristine Graphite	C∞	Calcd.	100	0	0	-	-
		Found	98.22	0.18	BDL	45.4	-
EFG	$C_{71.57}H_9O$	Calcd.	97.17	1.02	1.81	8.0	71.6
		Found	95.71	1.03	1.59	7.8	80.2

Theoretical C content for pristine graphite is assumed to be 100%, if negligible amount of edge chemical composition is ignored. Elemental analysis of pristine graphite shows CHO contents of 98.22, 0.18 and 0.00%, respectively. (BDL= Below detection limit) The theoretical CHO values of EFG are calculated based on final yield. That is, assuming that the amount of graphite remains constant, that of EBA is estimated. Empirical C value (95.71%) obtained from EFG is 1.47% lower than calculated value (97.17%). Considering the experimental C content (98.22%) of pristine graphite, the C values from theoretical and experimental contents are agreed well. In addition, empirical O content (1.59%) is also agreed well with theoretical one (1.81%). The C/H ratio of 'pristine' graphite was 45.4. The experimental C/O ratio of EFG was 80.2, indicating that there was no additional oxygen content beyond the value calculated on the basis of yield from the edge-selective functionalization.

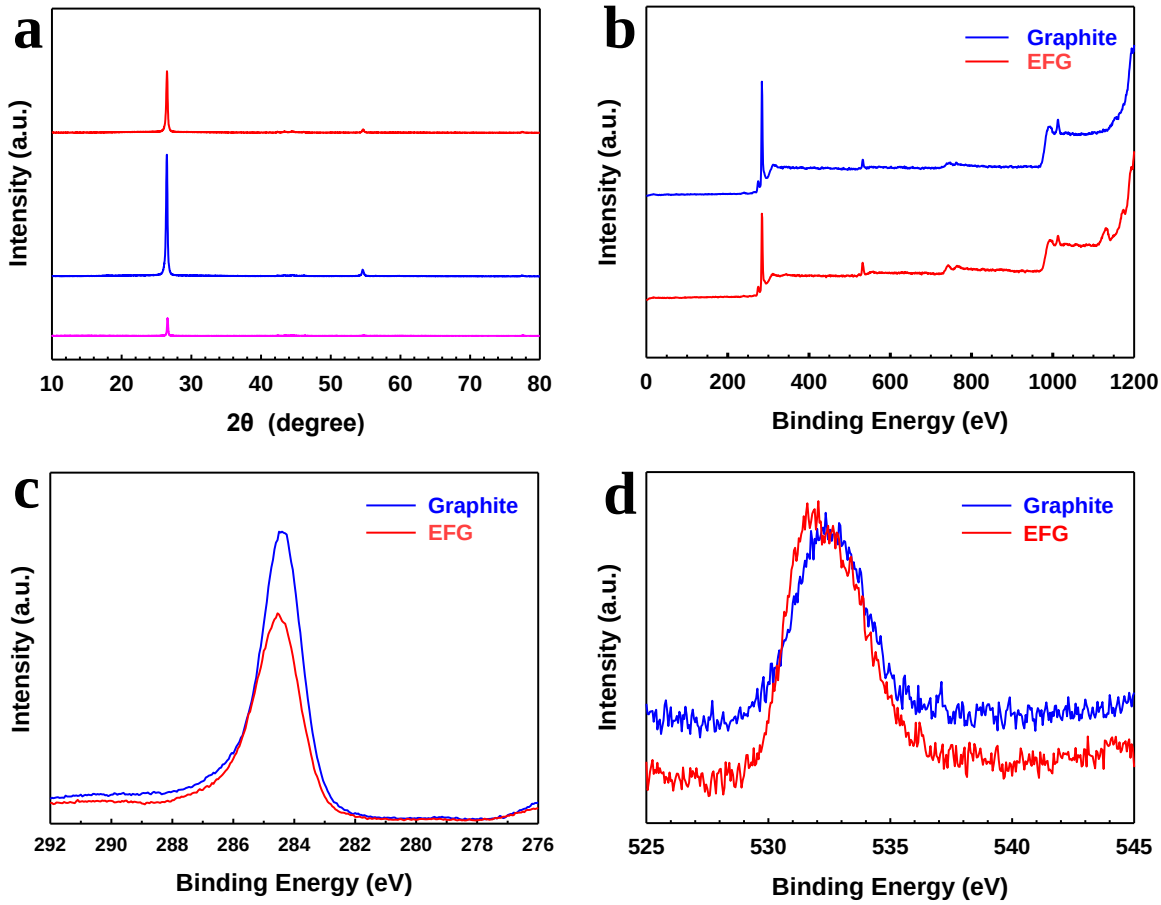

Figure 1.5. (a) XRD diffraction patterns: pristine graphite (red); PPA/P_2O_5-treated graphite (blue); EFG (hot pink). The relative peak intensity of PPA/P_2O_5-treated graphite was stronger than that of 'pristine' graphite. The result implied that PPA/P_2O_5 did not damaged but purified graphite. On the other hand, unlike graphene oxide (GO),[21] the peak intensity of EFG is approximately 10% to that of pristine graphite and the interlayer distance of EFG remains almost constant, indicating that basal plane is not functionalized. The intensity was approximately 90 % decreased due to the delaminating of graphite into a few layers of graphite (few-layer graphene sheets). The degree of exfoliation from pristine graphite into EFG in solid state could be approximately estimated. XPS spectra of pristine graphite and EFG: (b) full spectra; (c) carbon survey; (d) oxygen survey. EFG shows no additional oxygen content beyond the value calculated on the basis of yield from the edge-selective functionalization.

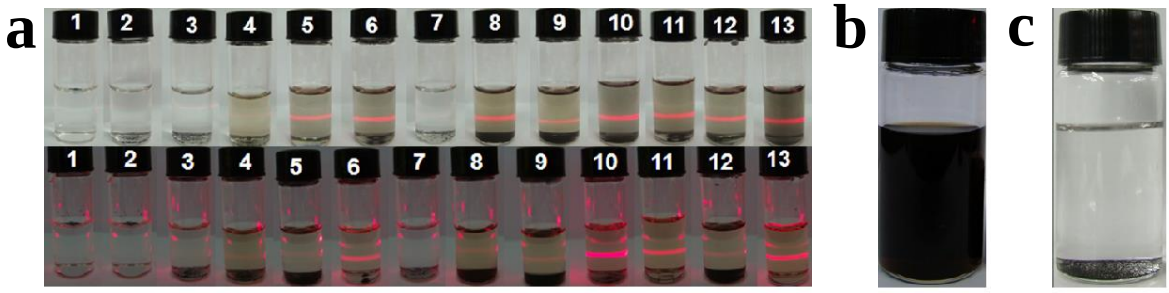

Figure 1.6. (a) EFG in a various solvents for dispersibility test: (top row) as soon as EFG dispersed; (bottom row) after one week (1, H_2O; 2, MeOH; 3, EtOH; 4, acetic acid; 5, toluene; 6, DMAc; 7, heptane; 8, acetone; 9, benzene; 10, dichloromethane; 11, THF; 12, pyridine; 13, NMP). Among them, DMAc, dichloromethane, THF and NMP show stronger Tyndall effect, indicating that larger amount of EFG stays in supernatant. (b) EFG solution (ca. 0.8 mg/mL) in dichloromethane. The color of EFG solution is dark black, implying that EFG maintains original conjugated structure at basal plane. On the other hand, the color of GO solution is light transparent yellow.[22] (c) 'Pristine' graphite dispersed in NMP (0.1 mg/mL). It was sediment after a day, leaving clear solution. It is an indication that pristine graphite dispersion in NMP is not thermodynamically stable (kinetic dispersion).

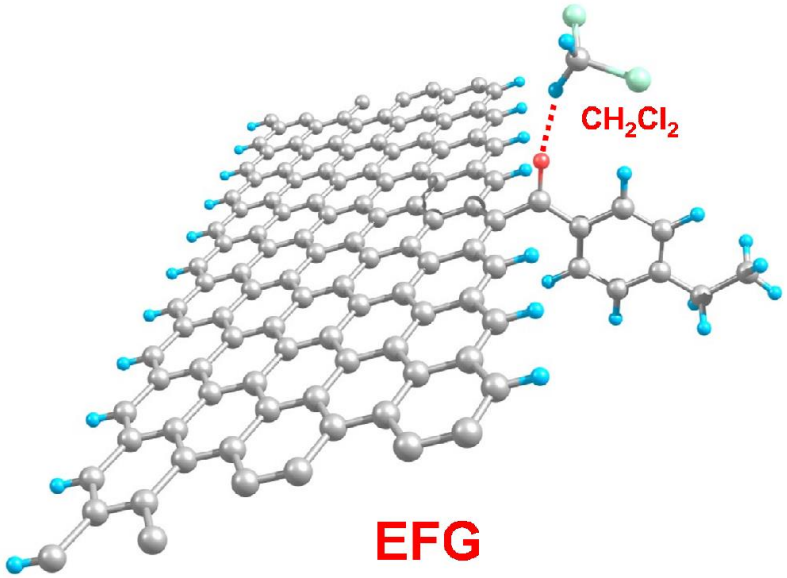

Figure 1.7. Calculated model geometry of EFG that shows polar interaction (14.7 kJ/mol) between

carbonyl group at the edge and dichloromethane. The phenyl ring on EB group is vertically aligned to the graphene plane.

The exfoliation/dispersibility of EFG was tested at room temperature in various solvents, namely water, methanol, ethanol, acetic acid, toluene, N,N-dimethylacetamide (DMAc), heptane, acetone, benzene, dichloromethane, tetrahydrofuran (THF), pyridine and N-methyl-2-pyrrolidone (NMP) (**Figure 1.6a**). It was found that the EFG could be dispersed in all of these solvents, and among them the dispersions in dichloromethane yielded the highest concentration at room temperature. Without physical agitation of any kind (e.g., it is known that sonication of certain types can damage the carbon framework[23]), the EFG was readily exfoliated to achieve stable dispersions with concentrations as high as 0.8 mg/mL in dichloromethane (**Figure 1.6b**). Mechanical (magnetic) stirring favored more rapid dispersion. The amount of EFG dispersed in each solvent was calculated as described in the experimental section (see Methods). The maximum concentration for a long-term (months) stable dispersion achieved is 8 higher than that reported for dispersions of graphite (0.1 mg/mL) in NMP,[24] which was found to be stable only for days after sonication (see below). Unlike aqueous dispersions of graphite oxide (light yellow),[25] the color of the EFG dispersion in dichloromethane is dark brown due to high conjugation in the undamaged basal planes (**Figure 1.4f**, **Figure 1.6b**). Tyndall scattering (red circle, **Figure 1.4f**) was observed with a hand-held laser pointer, demonstrating formation of colloid. After several months of standing in ambient condition, the supernatant from the dichloromethane dispersion at 0.8 mg/mL concentration remained visually unchanged with no sedimentation evident to the eye.

On the other hand, the dispersion of graphite in NMP was readily separated,[24] indicating that the dispersion was not thermodynamically stable leaving an essentially clear liquid after 1 day (**Figure 1.6c**). Molecular dynamics simulations suggest that the good dispersibility is because the phenyl rings on the EB groups are vertically aligned to the graphene plane, leading to a strong steric hindrance for reaggregration of the dispersed graphene platelets (**Figure 1.7** and detailed computation conditions are described in the Methods section). Transmission electron microscope (TEM) images show the presence

of graphene platelets (**Figure 1.4g**) with functionalized edges (**Figure 1.4h**).

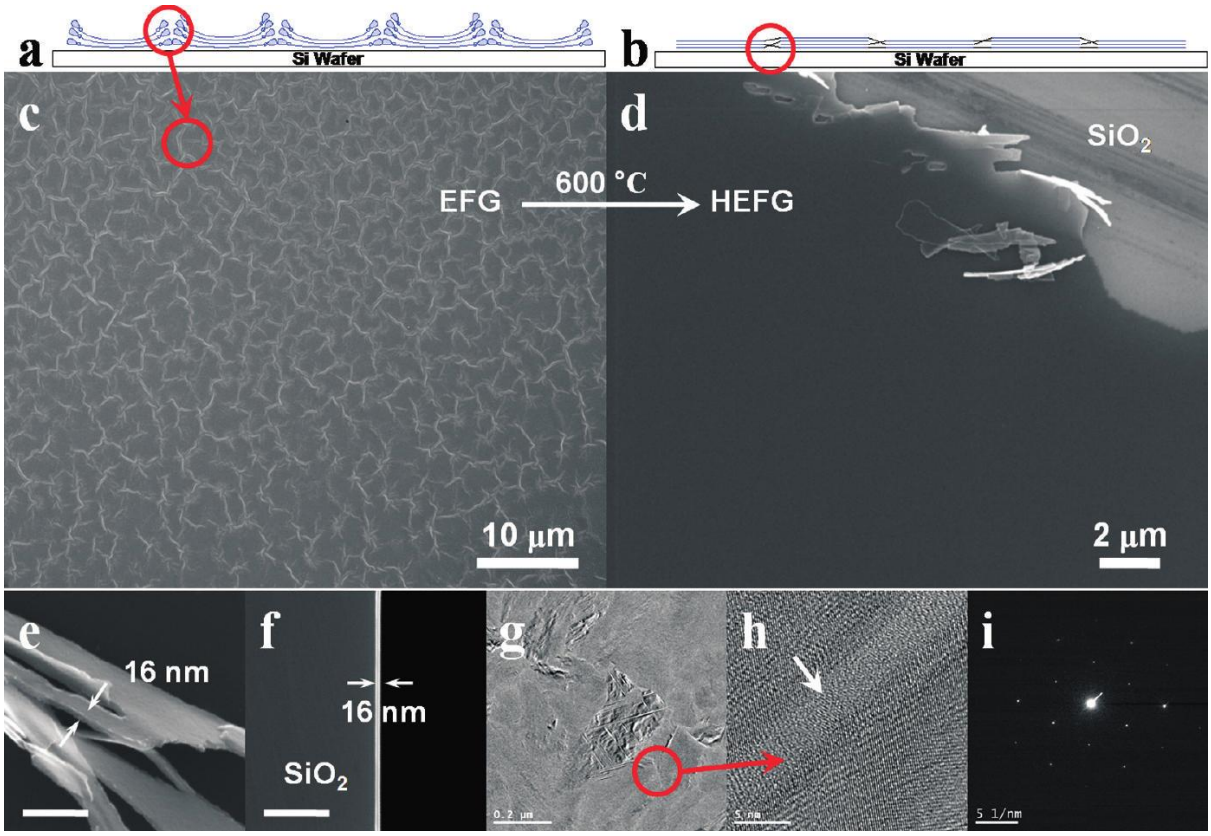

Figure 1.8. (a) Schematic presentation of as-cast EFG film on SiO_2 surface. (b) Schematic presentation of heat-treated EFG (HEFG) film on SiO_2 surface. (c) SEM image of as-cast EFG film drop-coated on SiO_2 surface from dichloromethane solution and then dried. (d) SEM image obtained on the surface of HEFG film at 600 ℃ under argon atmosphere for 3 h. The peeled-off area was scratched with a sharp metal tip, and this allowed discriminating the very smooth film from the SiO_2 surface substrate. (e) Edge-on SEM image of peeled-off area of HEFG film. Scale bar is 300 nm. (f) SEM image of the fracture surface of HEFG film on an SiO_2 surface. Scale bar is 300 nm. (g) TEM image of the surface of HEFG film. (h) TEM image focused on junction of HEFG at high magnification. (i) Selected area electron diffraction (SAED) pattern of HEFG film.

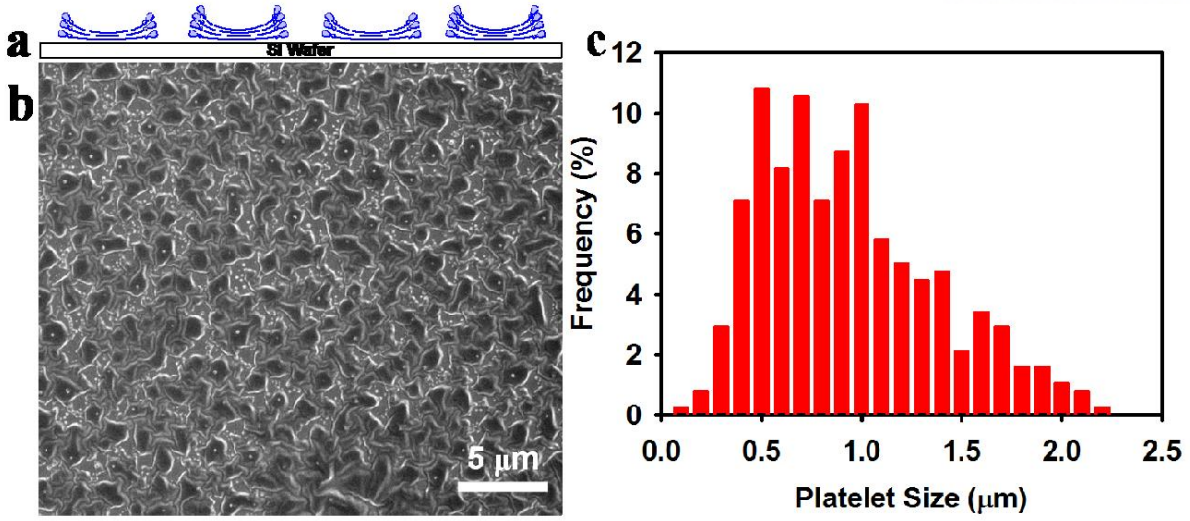

Figure 1.9. (a) Schematic presentation of EFG deposition on a SiO_2 surface with diluted solution. (b) SEM image obtained from diluted EFG solution on a SiO_2 surface. (c) Size distribution of EFG by using image analyzer software. Grain size distribution is in the range of 0.2-2.2 μm and average size is 0.97 μm.

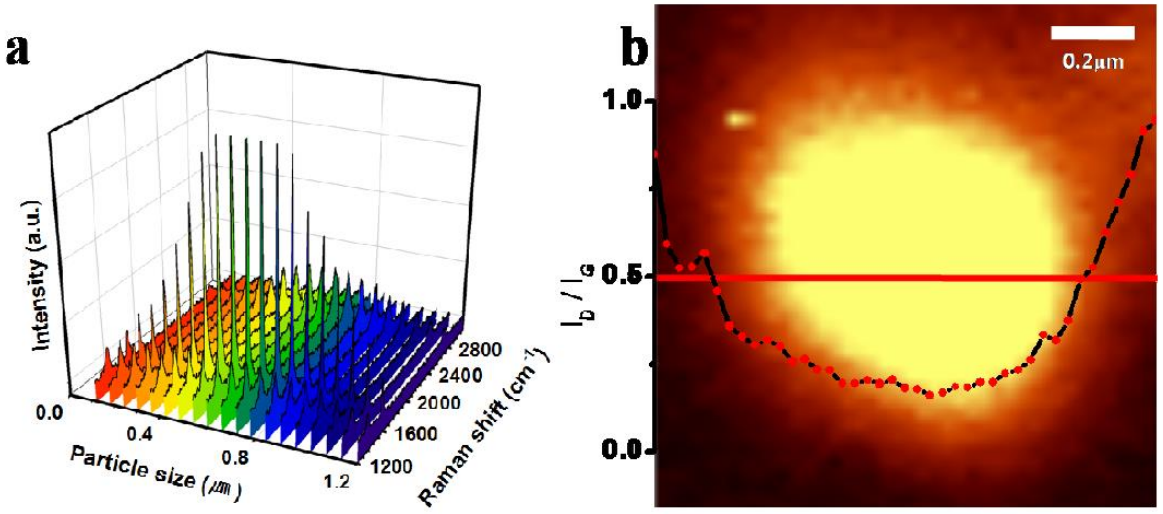

Figure 1.10. (a) Raman spectra obtained along the red line from left to right on confocal optical microscopy image in (b). (b) Confocal D and G band optical microscopy image of EFG on silicon substrate. The image cannot resolve clear edge boundary due to the fluorescent nature of EFG.

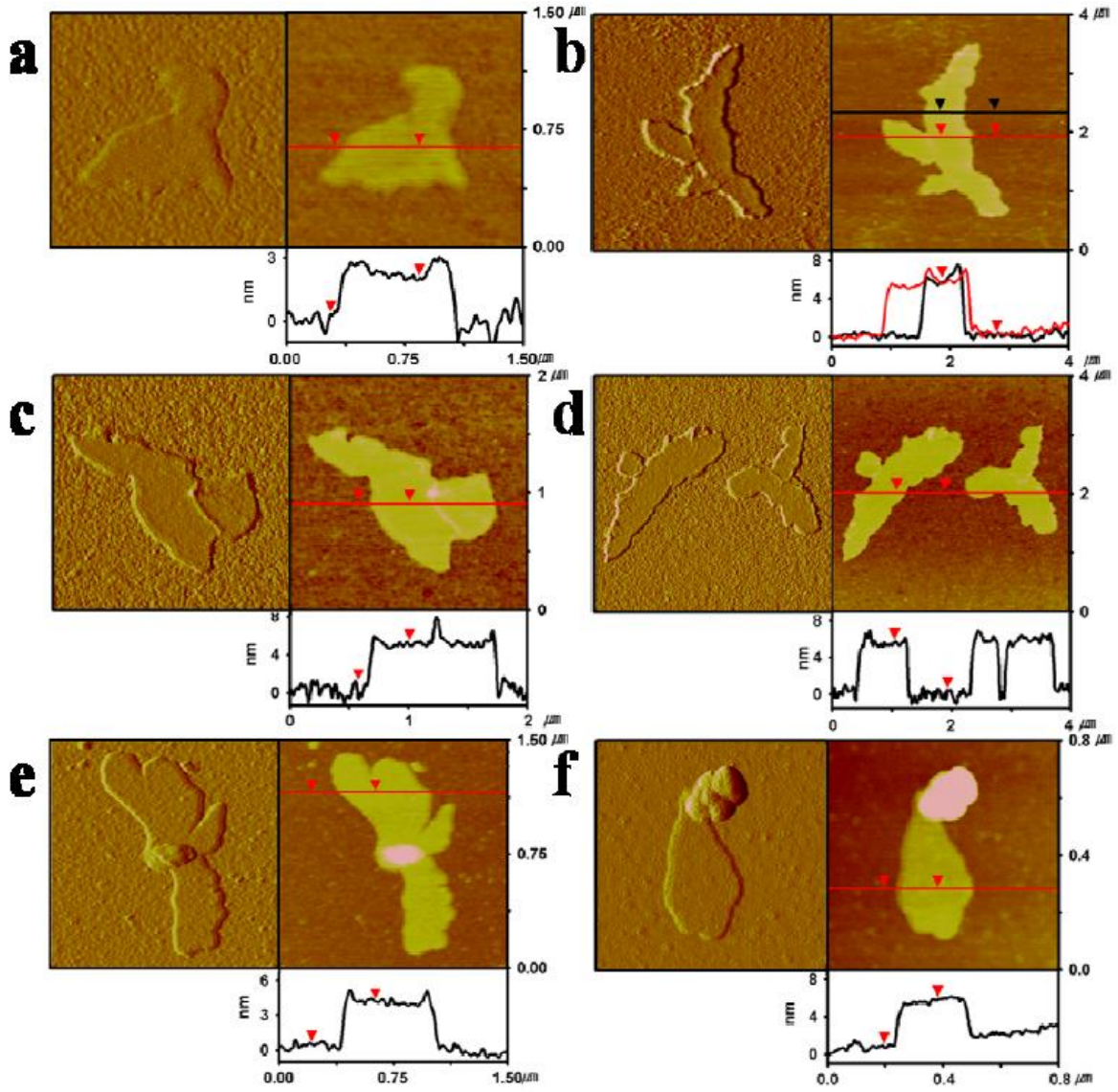

Figure 1.11. (a)-(f) AFM images (top-left: 3D and top-right: height) and topographic height profiles (bottom) obtained from EFG dispersion in dichloromethane and coated on a SiO_2 surface. In all cases, the EFG with approximately ~1 μm width and a few-microns length could be clearly observed. The maximum heights of few-layer graphene sheet(s) are in the range of 1.2-3.0 nm. The most importantly, the sharp height profiles at the edges of EFG are due to the presence of EBA grafts, which are covalently attached to sp^2 bonded C-H sites on the edges of graphite.[26]

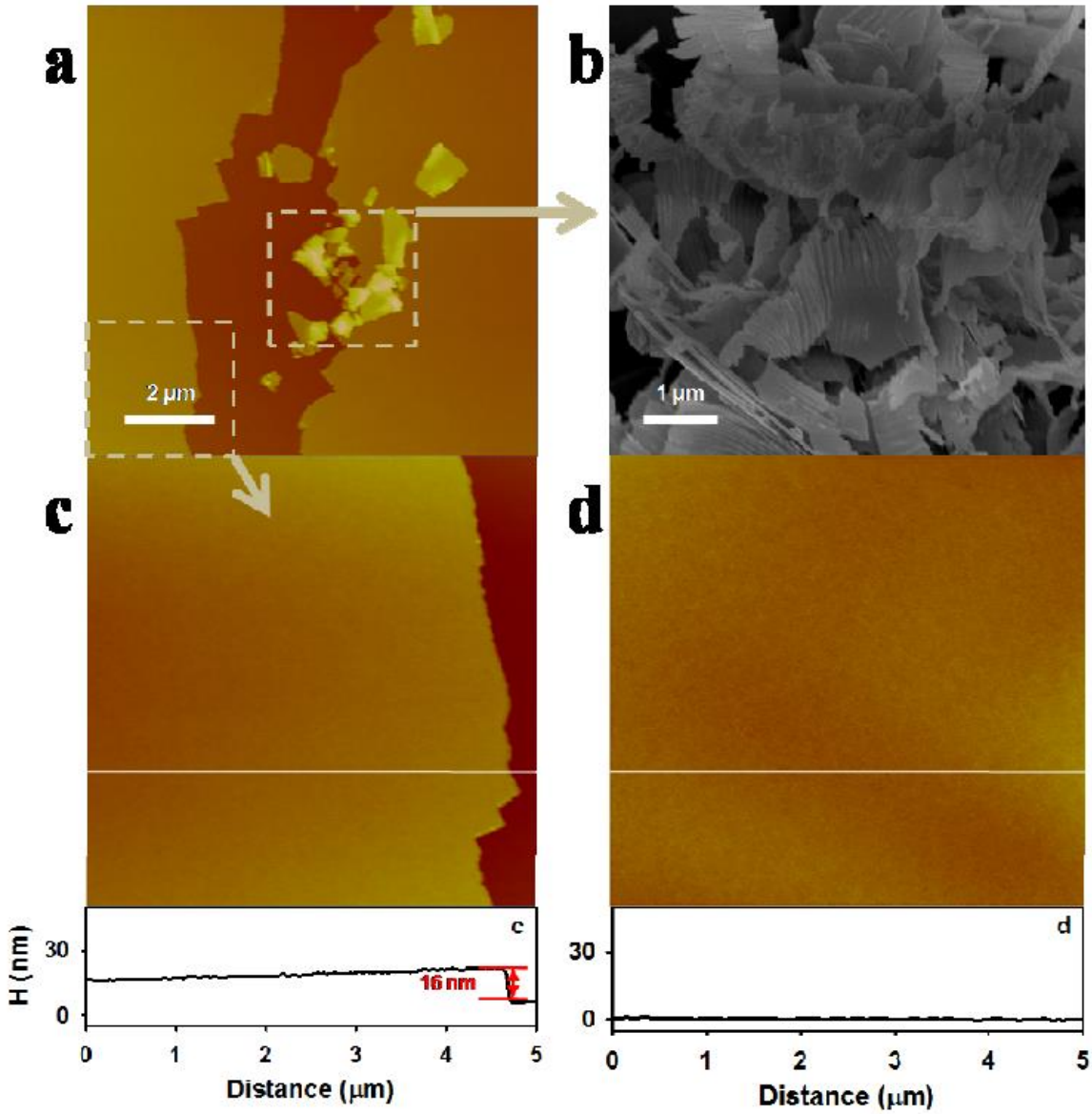

Figure 1.12. (a) AFM image of scratched HEFG film on a SiO_2 surface. (b) SEM image of scratched HEFG film debris. (c) AFM image of scratched HEFG film and height profile obtained across the lines. (d) SEM image obtained from HEFG film, showing uniformity of the film surface.

The SEM image of a solution-cast EFG film deposited on silicon oxide (SiO_2, 300 nm) surface from a diluted solution in dichloromethane shows individualized EFG platelets, as schematically illustrated in Supporting Information, **Figure 1.9a**. The lateral width distribution of EFG platelets (**Figure 1.9b**) was determined by an image analyzer to be in the range of 0.2-2.2 μm (**Figure 1.9c**); the average lateral size was approximately 1.0 μm. AFM images of platelets, deposited from EFG further diluted in dichloromethane on a SiO_2 surface, were used to estimate thicknesses of the platelets (**Figure 1.11**). The maximum heights of few-layer graphene platelets are in the range of 1.2-5.0 nm. As a result of the edge functionalization with EBA, the edge of EFG is not as sharp as graphene obtained from micromechanical exfoliation[27] or of reduced graphene oxide (rGO) platelets.[24] Together with Raman spectroscopy (**Figure 1.10**) and confocal optical microscopy image (**Figure 1.10**), the object shown at the edge of the EFG platelet in **Figure 1.11a** is interpreted to be a fewlayer EFG with its edge higher than its interior due to the presence of EB moieties at the edge.[28] The height profiles of platelets indicate that the maximum thickness of such platelets is less than 5 nm (**Figure 1.11**). The average lateral width from many other AFM images is ~1.0 μm. The width distribution from the AFM imaging agrees with the SEM result (see **Figure 1.9**). The concentrated EFG dispersion in dichloromethane was drop-coated on a SiO_2 surface. The SEM image shows platelets on the surface over a large area with many wrinkles (**Figure 1.8c**), as depicted in a schematic illustration shown in **Figure 1.8a**. The as-cast film shows high sheet resistance (~108 kΩ/sq) likely due to the edge groups at the boundaries between platelets contributing high contact resistance. Upon heat treatment at 600 ℃ in argon for 3 h, the edge EB moieties could act as an in situ feedstock for carbon to "weld" the graphene platelets thus forming a largearea graphene film (**Figure 1.8b** and **Figure 1.12**). Indeed, the SEM image of the heat-treated EFG (HEFG) film shows a uniform surface (**Figure 1.8d**). This film was scratched with a sharp metal (**Figure 1.8d** and **Figure 1.12a**). The thickness of the HEFG film was determined to be 16 nm by SEM images (**Figure 1.8e,f**) and AFM images using tapping mode (**Figure 1.12c**). Welded boundaries of HEFG could be distinguished from the surface of HEFG thin film (red circle, **Figure 1.8g**). The boundary of platelets, where thermal welding was assumed to occur during heat-treatment, can be

clearly seen at high magnification (**Figure 1.8h**). Selected area electron diffraction (SAED) indicates that the HEFG film has high crystallinity (**Figure 1.8i**). These results demonstrate that large-area graphene films can be achieved by solution casting.

The 16 nm thick film had an average sheet resistance of 1.3 kΩ/sq. This value is a few orders of magnitude lower than that of the chemically rGO.[29-30] The observed reduction in sheet resistance through heating the EFG film supports the concept of edge chemistry "boundary welding" that is in a good agreement with the TGA results (see **Figure 1.1b-c**).[19]

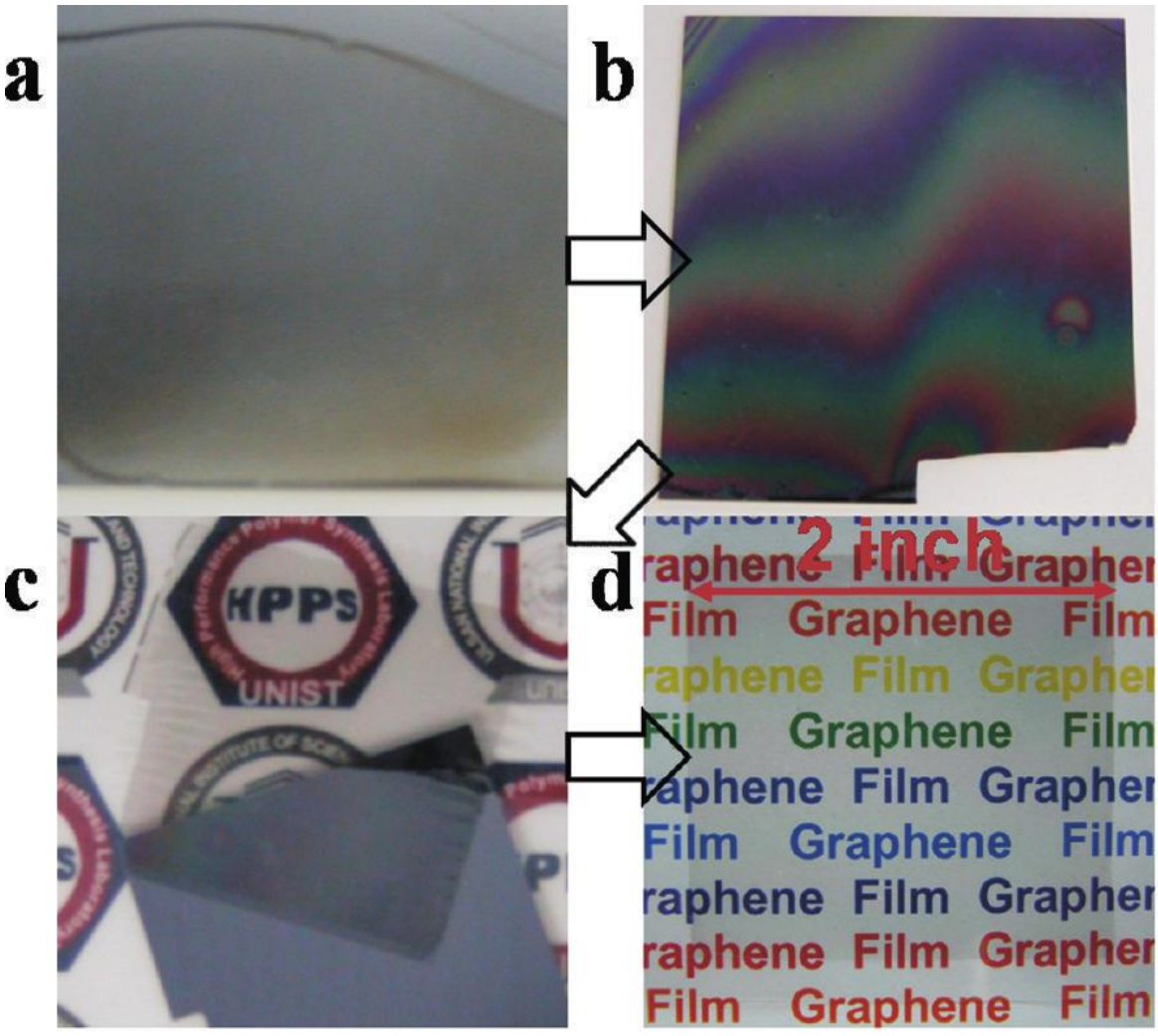

Figure 1.13. (a) Photograph of HEFG film on SiO_2 surface; (b) photograph of PMMA spin-coated on HEFG (HEFG/PMMA) film by spin coating; (c) freestanding HEFG/PMMA after SiO_2 surface eching; (d) 2 in. by 2 in. HEFG on PET (HEFG/PET) film.

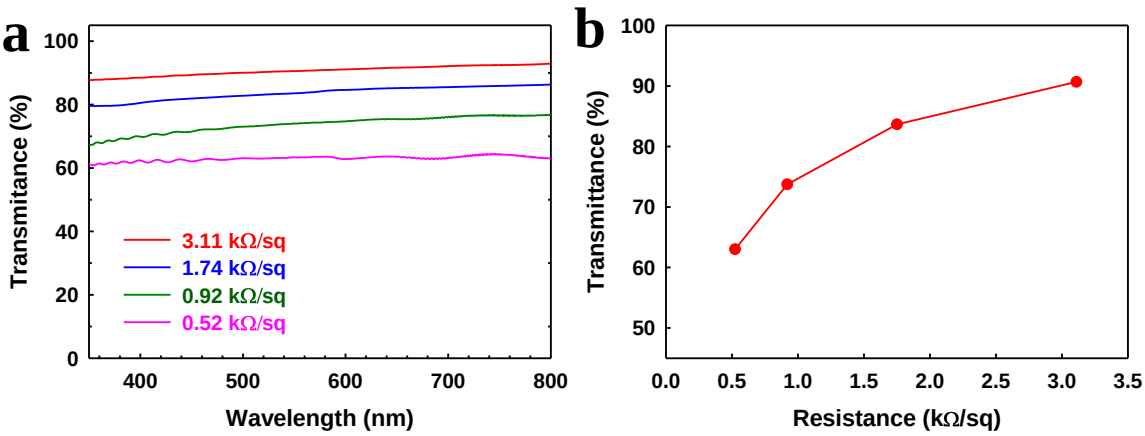

Figure 1.14. (a) Optical transmittance with respect to wavelength; (b) transmittance vs sheet resistance curve.

Large-area graphene films were made with different EFG concentrations in dichloromethane. These solutions were drop-coated onto a SiO_2 surface and subsequently heat-treated at 600 ℃ in argon for 3 h (**Figure 1.13a**). To transfer the solution-cast HEFG films onto other substrates, poly(methylmethaacrylate) (PMMA) solution in tetrahydrofuran (THF) was spin coated on such a HEFG film (**Figure 1.13b**). The SiO_2 layer was etched off by floating on aqueous 1M hydrofluoric acid (HF) solution (**Figure 1.13c**). Then, the HEFG on PMMA (HEFG/PMMA) film was transferred to poly(ethylene terephthalate) (PET) film and the PMMA was washed off by immersing in acetone to produce HEFG on PET(HEFG/PET) (**Figure 1.13d**). Four different HEFG/PET films with approximately 2 x 2 in. dimensions were tested, though many larger HEFG films on various substrates can be readily prepared through the similar procedure.

The optical transmittances and sheet resistances of the films were measured by using UV-vis spectroscopy and four-point probe, respectively. The optical transmittances are in the range of 63-90% (**Figure 1.14a**) with sheet resistances of 0.52-3.11 kΩ/sq (**Figure 1.14b**).

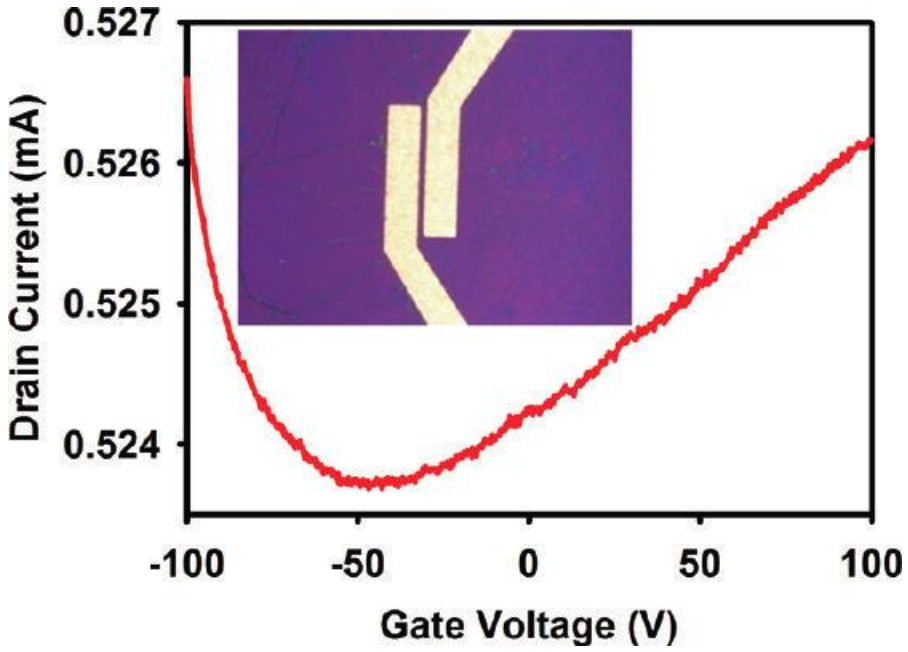

Figure 1.15. I-Vg curve of a field-effect transistor of HEFG film. The measurement was carried out in vacuum and bias voltage between source and drain electrodes was 0.1 V. The inset is an optical microscopy image of the device with the channel length of 4 μm.

Although these optoelectronic properties are still not as good as those of the CVD grown graphene film,[12] solution casting has many advantages in processing over the CVD process, indicating cost and scalability to very large area. **Figure 1.15** shows I-V characteristics of a field-effect transistor of HEFG film that was transferred onto a SiO_2 (300 nm)/Si wafer with prepatterned gold electrodes. The film shows ambipolar behavior with a Dirac point around ~50 V.[31]

1.6 Conclusion

Edge-selectively functionalized graphite (EFG) without damage to the basal plane can be produced with a simple one-pot reaction between graphite and 4-ethylbenzoic acid (EBA) in viscous PPA/P_2O_5 under mild conditions. The EFG could be dispersed in various organic solvents. Among 13 different organic solvents tested in this study, dichloromethane, THF, DMAc, and NMP were good solvents for dispersing EFG and this is attributed to high chemical affinity with these solvents. The EFG was dispersed in dichloromethane and exfoliated into EFG thin platelets. Edge-selective functionalization provides a pathway to exfoliation of graphite into few-layer graphene platelets without damages on their basal plane for better performance.

Dispersed platelets were drop-coated to produce a thin film that was then heat-treated at 600 ℃ under argon atmosphere, yielding a uniformly welded large-area graphene films with low sheet resistance (0.52-3.11 kΩ/sq) and comparable optical transmittance (63-90%). The EFG approach is a scalable method for the cost-effective production of high-quality graphene films.

1.7 References

1. Lee, C.; Wei, X.; Kysar, J. W.; Hone, J. Measurement of the elastic properties and intrinsic strength of monolayer graphene. *Science* **2008,** *321* (5887), 385-388.

2. Balandin, A. A.; Ghosh, S.; Bao, W.; Calizo, I.; Teweldebrhan, D.; Miao, F.; Lau, C. N. Superior thermal conductivity of single-layer graphene. *Nano Letters* **2008,** *8* (3), 902-907.

3. Novoselov, K. S.; Geim, A. K.; Morozov, S. V.; Jiang, D.; Zhang, Y.; Dubonos, S. V.; Grigorieva, I. V.; Firsov, A. A. Electric field in atomically thin carbon films. *Science* **2004,** *306* (5696), 666-669.

4. Stankovich, S.; Dikin, D. A.; Dommett, G. H. B.; Kohlhaas, K. M.; Zimney, E. J.; Stach, E. A.; Piner, R. D.; Nguyen, S. T.; Ruoff, R. S. Graphene-based composite materials. *Nature* **2006,** *442* (7100), 282-286.

5. Stoller, M. D.; Park, S.; Yanwu, Z.; An, J.; Ruoff, R. S. Graphene-Based ultracapacitors. *Nano Letters* **2008,** *8* (10), 3498-3502.

6. Mohanty, N.; Berry, V. Graphene-based single-bacterium resolution biodevice and DNA transistor: Interfacing graphene derivatives with nanoscale and microscale biocomponents. *Nano Letters* **2008,** *8* (12), 4469-4476.

7. Freitag, M. Graphene: Nanoelectronics goes flat out. *Nature Nanotechnology* **2008,** *3* (8), 455-457.

8. Geim, A. K.; Novoselov, K. S. The rise of graphene. *Nature Materials* **2007,** *6* (3), 183-191.

9. Novoselov, K. S.; Geim, A. K.; Morozov, S. V.; Jiang, D.; Katsnelson, M. I.; Grigorieva, I. V.; Dubonos, S. V.; Firsov, A. A. Two-dimensional gas of massless Dirac fermions in graphene. *Nature* **2005,** *438* (7065), 197-200.

10. Kim, K. S.; Zhao, Y.; Jang, H.; Lee, S. Y.; Kim, J. M.; Kim, K. S.; Ahn, J.-H.; Kim, P.; Choi, J.-Y.; Hong, B. H. Large-scale pattern growth of graphene films for stretchable transparent electrodes. *Nature* **2009,** *457* (7230), 706-710.

11. Tadatsugu, M. Transparent conducting oxide semiconductors for transparent electrodes. *Semiconductor Science and Technology* **2005,** *20* (4), S35.

12. Bae, S.; Kim, H.; Lee, Y.; Xu, X.; Park, J.-S.; Zheng, Y.; Balakrishnan, J.; Lei, T.; Ri Kim, H.; Song, Y. I.; Kim, Y.-J.; Kim, K. S.; Ozyilmaz, B.; Ahn, J.-H.; Hong, B. H.; Iijima, S. Roll-to-roll production of 30-inch graphene films for transparent electrodes. *Nat Nano* **2010,** *5* (8), 574-578.

13. Li, X.; Cai, W.; An, J.; Kim, S.; Nah, J.; Yang, D.; Piner, R.; Velamakanni, A.; Jung, I.; Tutuc, E.; Banerjee, S. K.; Colombo, L.; Ruoff, R. S. Large-area synthesis of high-quality and uniform graphene films on copper foils. *Science* **2009,** *324* (5932), 1312-1314.

14. De, S.; Coleman, J. N. Are There Fundamental Limitations on the Sheet Resistance and Transmittance of Thin Graphene Films? *ACS Nano* **2010,** *4* (5), 2713-2720.

15. Hummers Jr, W. S.; Offeman, R. E. Preparation of graphitic oxide. *Journal of the American Chemical Society* **1958,** *80* (6), 1339.

16. Boukhvalov, D. W.; Katsnelson, M. I. Modeling of graphite oxide. *Journal of the American Chemical Society* **2008,** *130* (32), 10697-10701.

17. Choi, E.-K.; Jeon, I.-Y.; Bae, S.-Y.; Lee, H.-J.; Shin, H. S.; Dai, L.; Baek, J.-B. High-yield exfoliation of three-dimensional graphite into two-dimensional graphene-like sheets. *Chemical Communications* **2010,** *46* (34), 6320-6322.

18. Kresse, G.; Furthmüller, J. Efficient iterative schemes for \textit{ab initio} total-energy calculations using a plane-wave basis set. *Physical Review B* **1996,** *54* (16), 11169-11186.

19. Chen, J.; Shan, J. Y.; Tsukada, T.; Munekane, F.; Kuno, A.; Matsuo, M.; Hayashi, T.; Kim, Y. A.; Endo, M. The structural evolution of thin multi-walled carbon nanotubes during isothermal annealing. *Carbon* **2007,** *45* (2), 274-280.

20. Stankovich, S.; Piner, R. D.; Chen, X.; Wu, N.; Nguyen, S. T.; Ruoff, R. S. Stable aqueous dispersions of graphitic nanoplatelets via the reduction of exfoliated graphite oxide in the presence of poly(sodium 4-styrenesulfonate). *Journal of Materials Chemistry* **2006,** *16* (2), 155-158.

21. Szabó, T.; Berkesi, O.; Dékány, I. DRIFT study of deuterium-exchanged graphite oxide. *Carbon* **2005,** *43* (15), 3186-3189.

22. Li, X.; Zhang, G.; Bai, X.; Sun, X.; Wang, X.; Wang, E.; Dai, H. Highly conducting graphene sheets and Langmuir-Blodgett films. *Nature Nanotechnology* **2008,** *3* (9), 538-542.

23. Suslick, K. S. Sonochemistry. *Science* **1990,** *247* (4949), 1439-1445.

24. Hernandez, Y.; Nicolosi, V.; Lotya, M.; Blighe, F. M.; Sun, Z.; De, S.; McGovern, I. T.; Holland, B.; Byrne, M.; Gun'ko, Y. K.; Boland, J. J.; Niraj, P.; Duesberg, G.; Krishnamurthy, S.; Goodhue, R.; Hutchison, J.; Scardaci, V.; Ferrari, A. C.; Coleman, J. N. High-yield production of graphene by liquid-phase exfoliation of graphite. *Nature Nanotechnology* **2008,** *3* (9), 563-568.

25. Li, X.; Wang, H.; Robinson, J. T.; Sanchez, H.; Diankov, G.; Dai, H. Simultaneous Nitrogen Doping and Reduction of Graphene Oxide. *Journal of the American Chemical Society* **2009,** *131* (43), 15939-15944.

26. Hashimoto, A.; Suenaga, K.; Gloter, A.; Urita, K.; Iijima, S. Direct evidence for atomic defects in graphene layers. *Nature* **2004,** *430* (7002), 870-873.

27. Blake, P.; Hill, E. W.; Castro Neto, A. H.; Novoselov, K. S.; Jiang, D.; Yang, R.; Booth, T. J.; Geim, A. K. Making graphene visible. *Applied Physics Letters* **2007,** *91* (6), 063124.

28. Stolyarova, E.; Kwang, T. R.; Ryu, S.; Maultzsch, J.; Kim, P.; Brus, L. E.; Heinz, T. F.; Hybertsen, M. S.; Flynn, G. W. High-resolution scanning tunneling microscopy imaging of mesoscopic graphene sheets on an insulating surface. *Proceedings of the National Academy of Sciences of the United States of America* **2007,** *104* (22), 9209-9212.

29. Gao, W.; Alemany, L. B.; Ci, L.; Ajayan, P. M. New insights into the structure and reduction of graphite oxide. *Nat Chem* **2009,** *1* (5), 403-408.

30. Park, S.; Ruoff, R. S. Chemical methods for the production of graphenes. *Nature nanotechnology* **2009,** *4* (4), 217-224.

31. Heersche, H. B.; Jarillo-Herrero, P.; Oostinga, J. B.; Vandersypen, L. M. K.; Morpurgo, A. F. Bipolar supercurrent in graphene. *Nature* **2007,** *446* (7131), 56-59.

II. Large-Area Two-Dimensional Porous Benzimidazole Based Polymer as Pt-Free Counter Electrode for Dye Sensitized Solar Cells

2.1Abstract

The prohibitive cost of platinum for electrocatalytic activity have hampered the widespread use or count electrode in dye sensitized solar cells (DSSCs). We report the use of two dimensional holypolybenzimidazoles (HPBIs), which is nitrogen-rich structure, as highly conductive and durable count electrode (CE) supports of iron additives for DSSCs to replace the precious platinum. We confirm the effect of thermal annealing and additives of iron from T-HPBI for electrocatalytic activity from the symmetrical dummy cell with two identical electrodes. After heat-treatment, the R_{CT} of HT-HPBI (R_{CT} = 4.247 Ω cm^2) value dramatically decreased by 99 percent compared to T-HPBI (R_{CT} = 398.5 Ω cm^2). After adding 10^{-2} wt% iron in T-HPBI supports and heating, the R_{CT} of the Fe@HT-HPBI (R_{CT} = 2.536 Ω cm^2) decreased by 40 percent compared to HT-HPBI because of the electrocatalytic activity of iron in benzimidazole based polymer.

2.2 Introduction

Dye-sensitized solar cells (DSSCs) have engaged many researcher's interest because of low-cost and easy fabrication and high power conversion efficiency (PCE).[1-2] Over the last 20 years, great progress has been accomplished in the efficiency, stability and reproducibility of DSSCs.[3] Classic DSSCs consist of a TiO_2 photoanode, a counter electrode (CE) and an electrolyte. Therefore, optimization of all components of DSSCs is required for improving performance of DSSCs. The CE is a critical component of DSSCs. Especially, Platinum (Pt) is widely used because of its high catalytic activity and high conductivity. However, Pt have limitations such as cost problem of Pt metal and scarcity of resources in nature. The limited Pt metal cannot satisfy the increasing demand for broad applications.

Requirements for high performance of CE catalytic materials in DSSCs are high catalytic activity and electrical conductivity, chemical stability, good affinity with dye and electrolyte and high surface area.[4] Various materials such as carbon based materials, transition metal compounds (TMCs), conductive polymers and hybrids have been designed to meet requirements for replacing expensive Pt CE in DSSC. Recently, carbon materials such as carbon nanotube,[5-6] graphene,[7-9] carbon nanoparticles,[10] carbon black[11] and others have attracted tremendous attention due to their high electric conductivity, chemical stability, large surface area and light weight. Especially, nitrogen-doped carbon nanomaterials such as graphene and carbon nanotube have showed superior electrocatalytic performance owing to the electron accepting ability of the nitrogen atoms, which creates a positive charge on adjacent carbon atoms.[12-17] Due to the electrocatalytic activity from nitrogen atoms in carbon material, the researches of synthesis for nitrogen contained porous polymers such as covalent triazine frameworks[18-20], Imine-based frameworks[21-23] have been reported.

Moreover, additional additives such as Co and Fe have been added in a heteroatom-doped carbon supports to enhance the electrocatalytic activity.[24-28] Additionally, nitrogen-rich polymer have taken role of the supports for holding transitional metal, additives for electrocatalytic activity, such as Co[27],

Fe[27, 29], Pd[30] and Pt[18].

Here, we report the use of two dimensional holypolybenzimidazoles (HPBIs) as highly conductive and durable count electrode (CE) supports of iron additives for DSSCs to replace the precious platinum. Two kinds of benzimidazole based polymer were synthesized in polyphorous acid (PPA) medium from hexa-aminobenzene to H-HPBI and from tetraaminobenzene to T-HPBI. We tested three kinds of T-HPBIs, T-HPBI, HT-HPBI and Fe@HT-HPBI, for CE of the organic DSSCs in conjunction with a $Co(bpy)_3^{2+/3+}$ redox couple. We confirmed the effect of annealing and additives of iron from T-HPBI for electrocatalytic activity.

2.3 Materials and Instrumentation

Hexaaminobenzene was prepared according to the literature, reported by our own group.[31] Other solvent and reagents were purchased from Sigma-Aldrich Chemical Inc.

Fourier transform infrared (FT-IR) spectra were obtained by Perkin-Elmer Spectrum 100 using KBr disks. X-Ray diffraction (XRD) patterns were analyzed by a Rigaku D/MAZX2500V/PC with Cu-Kα radiation. X-ray photoelectron spectroscopy (XPS) was performed on X-ray Photoelectron Spectroscopy Thermo Fisher K-alpha (UK). Elemental analysis (EA) was measured with Thermo Scientific Flash 2000. Themogravimetric analysis (TGA) was recorded on a TA Q200 (TA instrument) under air and nitrogen at a heating rate of 10 °C/min. The field emission scanning electron microscopy (FE-SEM) was obtained by FEI Nanonova 230. The surface area was taken by nitrogen adsorption-desorption isotherms using Brunauer-Emmett-Teller (BET) method on Micromeritics ASAP 2504N.

2.4 Experiment Section

2.4.1. Synthesis of 1,5-dichloro-2,4-dinitrobenzene

m-Dichlorobenzene (50 g, 0.34 mol) was put with sulfuric acid (50 mL, H_2SO_4) in three-necked round flask under nitrogen atmosphere and was stirred until become homogeneous mixture. The exceed potassium nitrate (100 g, 0.98 mol) was added drop wise slowly into well-mixed solution at room temperature. The temperature was increased automatically until 110 °C because nitration is exothermic reaction. After dropping was completed, the transparent solution kept stirred at 130 °C for 1 h and was cooled down at 90 °C to precipitate from ice water. The precipitation was collected by suction filtration, vacuum-dried and recrystallized into yellow needle crystal from boiling ethanol to give 65.65 g (81.5 % yield) of 1,5-dichloro-2,4-dinitrobenzene.

2.4.2. Synthesis of 1,5-diamino-2,4-dinitrobenzene

In round-bottom flask, 1,5-dichloro-4,6-dinitrobenzene (25 g, 0.11 mol) was stirred in 180 mL of ethylene glycol at 140 °C until mixture became clear light-yellow solution. Ammonia gas was bubbled at a regular rate to absorb into solution enough. Within 5 min, the color of solution was changed to deep red and, then the orange colored powder was precipitated out from the reaction mixture. The resultant was filtered with hot ethanol and water in several times to purify the compound having poor solubility. The yield was 18 g (83 %) with orange powder after dried at 80 °C under vacuum.

2.4.3. Synthesis of 1,2,4,5-tetraaminobenzene

1,2,4,5-tetraaminobenzene (TAB, 5.0 g, 0.025 mol) was synthesized by reduction in a high-pressure hydrogenation bottle with 10 % Pd/C (0.67 g) and 300mL of 5 % hydrochloride (5 v/v % HCl) as a solvent. The reaction flask was placed tightly in hydrogenation apparatus and filled out hydrogen (H_2, 4.5 bar) for 3days until the orange colored precursor disappeared completely. The resultant solution was filtered into concentrated HCl (conc. HCl or 37% HCl) located bottom under reduced pressure over celite to eliminate the Pd/C catalyst. The obtained powder was recrystallized with water/conc.HCl mixture as solvent under nitrogen (N_2) to prevent oxidation of amine. Final product was whitish small crystal to afford 4.5223 g (63.2 %).

2.4.4. Synthesis of Holy-polybenzimidazole from hexaaminobenzene (H-HPBI)

For synthesis of H-HPBI, 1,2,3,4,5,6-Hexaaminobenzene (1 g, 3.603 mmol) was placed with a high torque mechanical stir with polyphosphoric acid as a solvent in resin flask under nitrogen inlet and outlet. To remove the HCl which is used for reducing the amine reactivity, the medium was stirred at R.T and 50 °C for 12 h and 12 h until the color of mixture became transparent blue. After prior step was completed, the trimesic acid (0.76 g, 3.617 mmol) was put in the cold flask and, then the flask was heated up at 100 °C, 150 °C and 180 °C for 2 h, 24 h and 6h, respectively. The color was darker and darker with the course of time during reaction before high viscosity occurred. The medium have high viscosity at 180 °C after 5h at the same time forming high molecular weight. Then, the black resultant was poured into the D.I water to make the precipitation and washed using Soxhlet extractor with water and methanol for 2 and 3days, respectively. The black product was freeze dried under low pressure with yield of 1.0742 g (97.42 %).

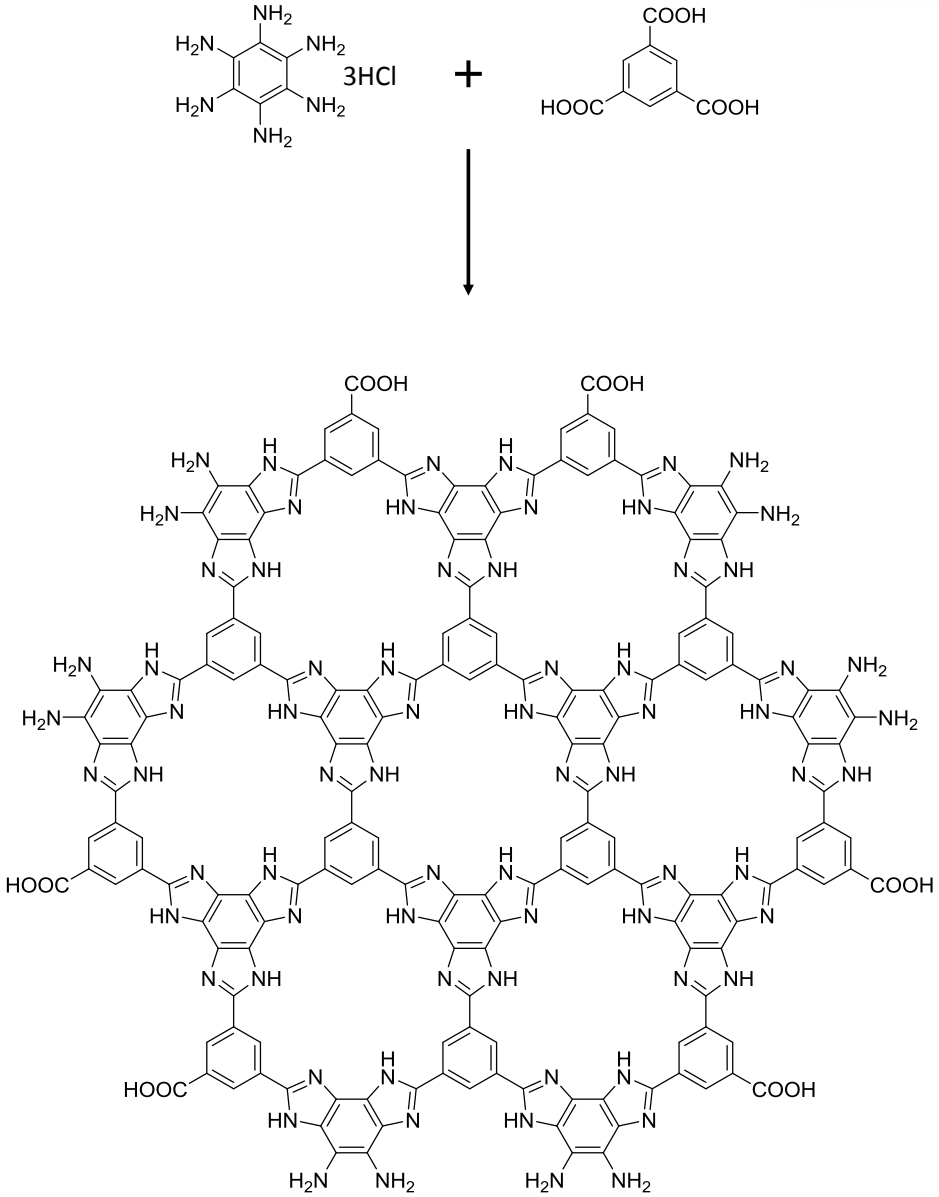

Figure 2.1. Schematic presentation for the formation of H-HPBI in PPA. The condensation reaction between hexaaminobenzene and tricarboxylic was conducted in PPA medium.

2.4.5. Synthesis of Holey-polybenzimidazole from tetraaminobenzene (T-HPBI)

T-HPBI was prepared using tetraaminobenzene and trimesic acid in 60 g of polyphosphoric acid (PPA, 83 % P_2O_5 assay) in resin flask under nitrogen atmosphere with a high torque mechanical stirrer. In first step, tetraaminobenzene (2.0 g, 7.042 mmol) was mechanically stirred in PPA at room temperature, 40 °C and 60 °C for 24 h, 24 h and 20 h, respectively, to completely remove the HCl in the TAB molecules. The light and transparent brown medium was cooled down at R.T after getting rid of the HCl perfectly and trimesic acid (0.991 g, 4.718 mmol) was added one portion into flask. Then, the temperature was increased to 60 ℃ for 2h, 100 °C for 5h and 150 °C for 3 h to make the homogeneous medium and polyamide as transition state before formation of polybenzimidazole. Ring closure of imidazole, the reddish brown medium kept at 170 ℃ 1h 20 min until it became dark brownish gel-like resultant due to high molecular weight. The resultant was precipitated in D.I water and extracted with water in Soxhlet for 2 days and methanol for 3 days to purify from acidic solvent and unreacted monomer as well as small molecular impurities. The brownish final compound was obtained by freeze drying at -120 °C under reduced pressure to afford 1.4123 g (92.5 %).

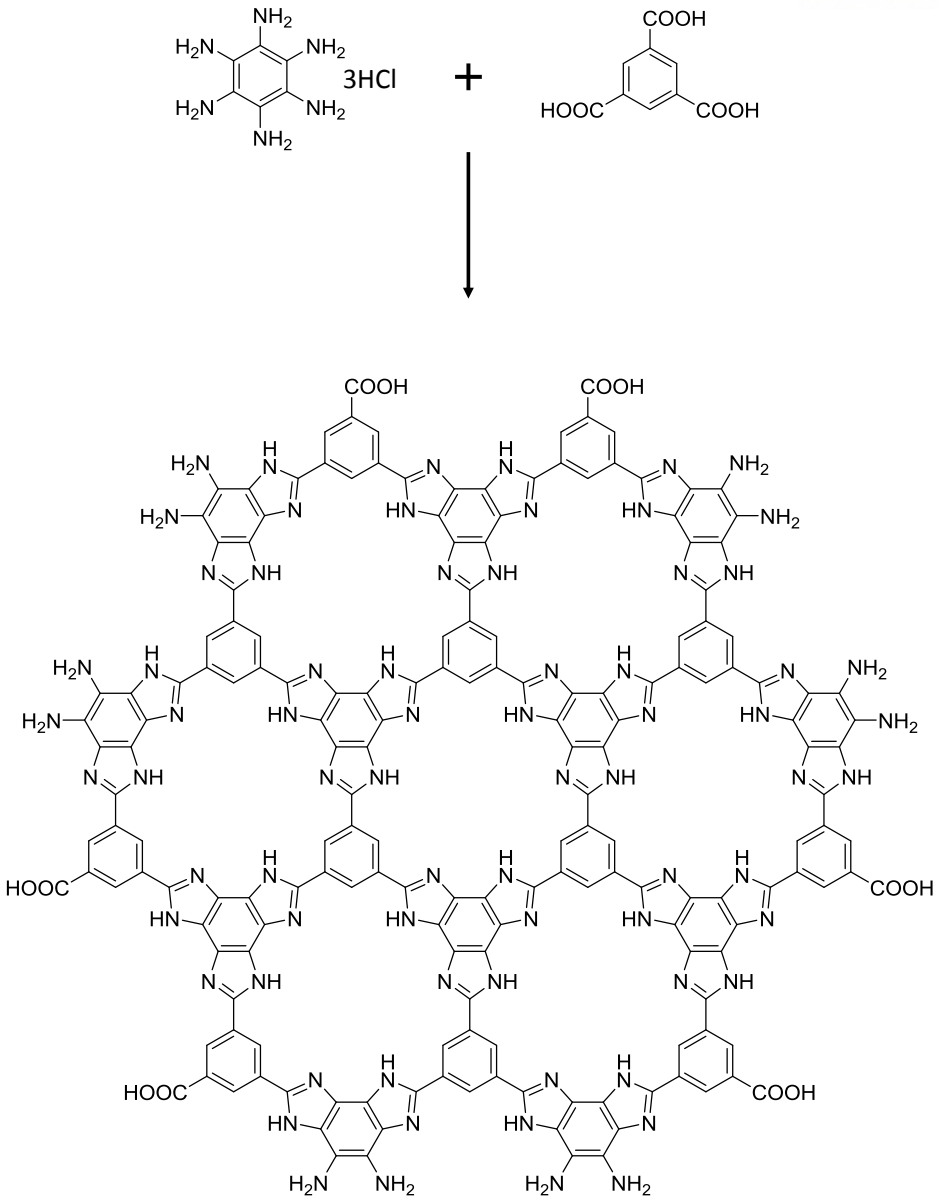

Figure 2.2. Schematic presentation for the formation of H-HPBI in PPA. The condensation reaction between hexaaminobenzene and tricarboxylic was conducted in PPA medium.

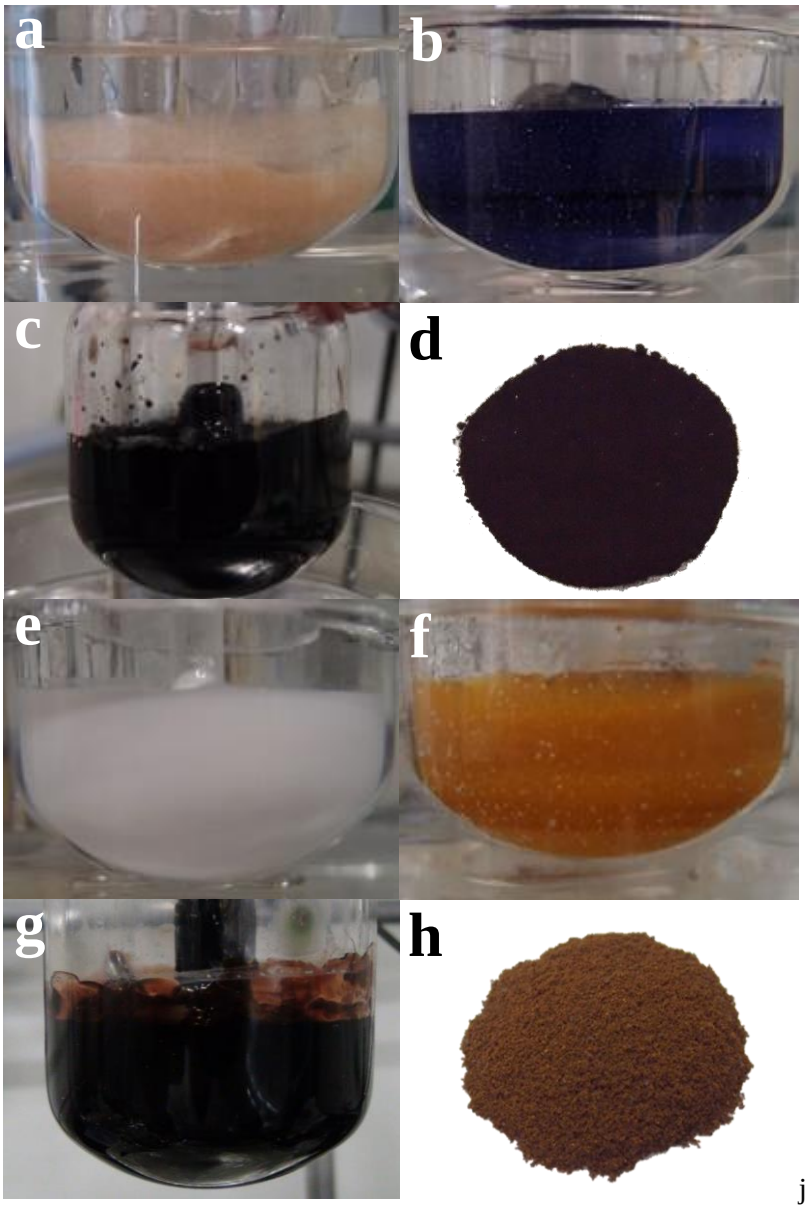

Figure 2.3. Photographs of reaction of HPBIs in PPA. (a-d) H-HPBI: (a) Hexaaminobenzene in PPA at room temperature, (b) Changing of color from peach to blue and addition of trimesic acid after removing HCl, (c) Reaction flask at the final stage of reaction with high viscosity, (d) Black powder after post-treatment. (e-h) T-HPBI: (e) Tetraaminobenzene in PPA at room temperature, (f) Changing of color from white to orange and addition of trimesic acid after removing HCl, (g) Reaction flask at the final stage of reaction with high viscosity, (h) Brown powder after post-treatment.

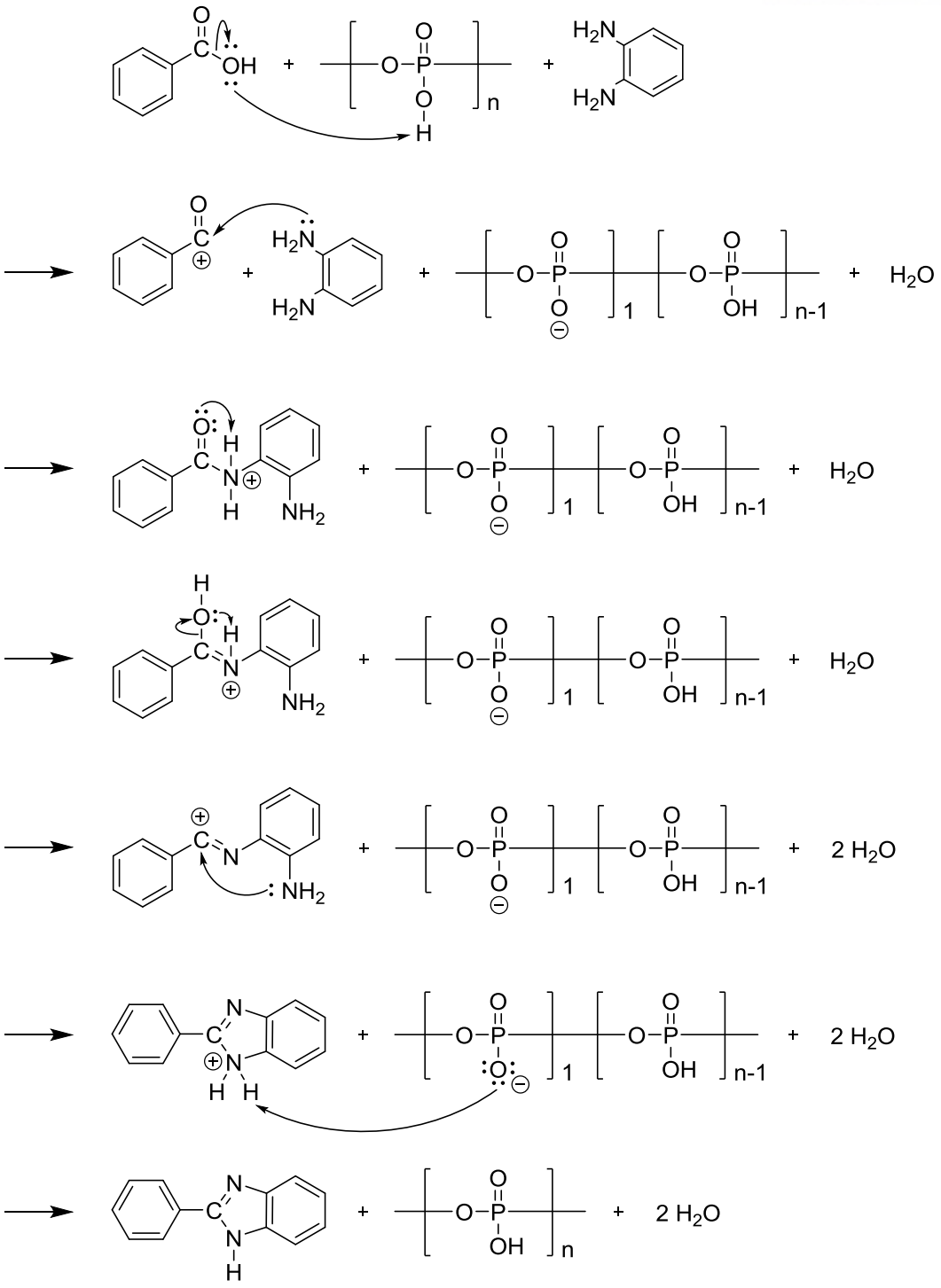

Figure 2.4. The mechanism of benzimidazole compounds in polyphosphoric acid.

2.4.6. Fabrication of T-HPBI film and HT-HPBI film

0.25 g/L T-HPBI solution in 2-propanol was prepared and deposited directly on FTO using an e-spray technique. A plastic syringe contained the T-HPBI solution with a 30-gauge stainless steel hypodermic needle was prepared and a high voltage power (~ 5 kV) supply (ESN-HV30) applied to the needle at syringe. The distance between a metal orifice and the conducting substrate is 10 cm and a constant flow rate of T-HPBI solution was 150 μL min^{-1}. Heat-treated T-HPBI (HT-HPBI) from T-HPBI film by e-spray technique was prepared though annealing at 400 ˚C for 1 hr in Ar atmosphere.

2.4.7. Fabrication of Fe@HT-HPBI film

0.0001 wt% iron chloride ($FeCl_2$) was added in 0.25 g/L T-HPBI solution in 2-propanol. The resulting solution was deposited directly on FTO using an e-spray technique. A plastic syringe contained the T-HPBI solution with a 30-gauge stainless steel hypodermic needle was prepared and a high voltage power (~ 5 kV) supply (ESN-HV30) applied to the needle at syringe. The distance between a metal orifice and the conducting substrate is 10 cm and a constant flow rate of T-HPBI solution was 150 μL min^{-1}. Heat-treated Fe@T-HPBI (Fe@HT-HPBI) from Fe@T-HPBI film by e-spray technique was prepared though annealing at 400 ˚C for 1 hr in Ar atmosphere.

2.4.8. Fabrication of symmetrical dummy cells for electrochemical catalytic activities

The symmetrical sandwich dummy cell was fabricated from four identical NGnP-FTO or Pt-FTO sheets, which were separated by 60 μm thick Surlyn (Solaronix, Switzerland) tape as a seal and spacer leaving 0.6 × 0.6 cm^2 active area. The cell was filled with an electrolyte solution through a hole in one FTO support which was finally closed by a Surlyn seal. The FTO sheet edges were coated by ultrasonic soldering (USS-9200, MBR Electronics) to improve electrical contacts.

2.5 Results and Discussion

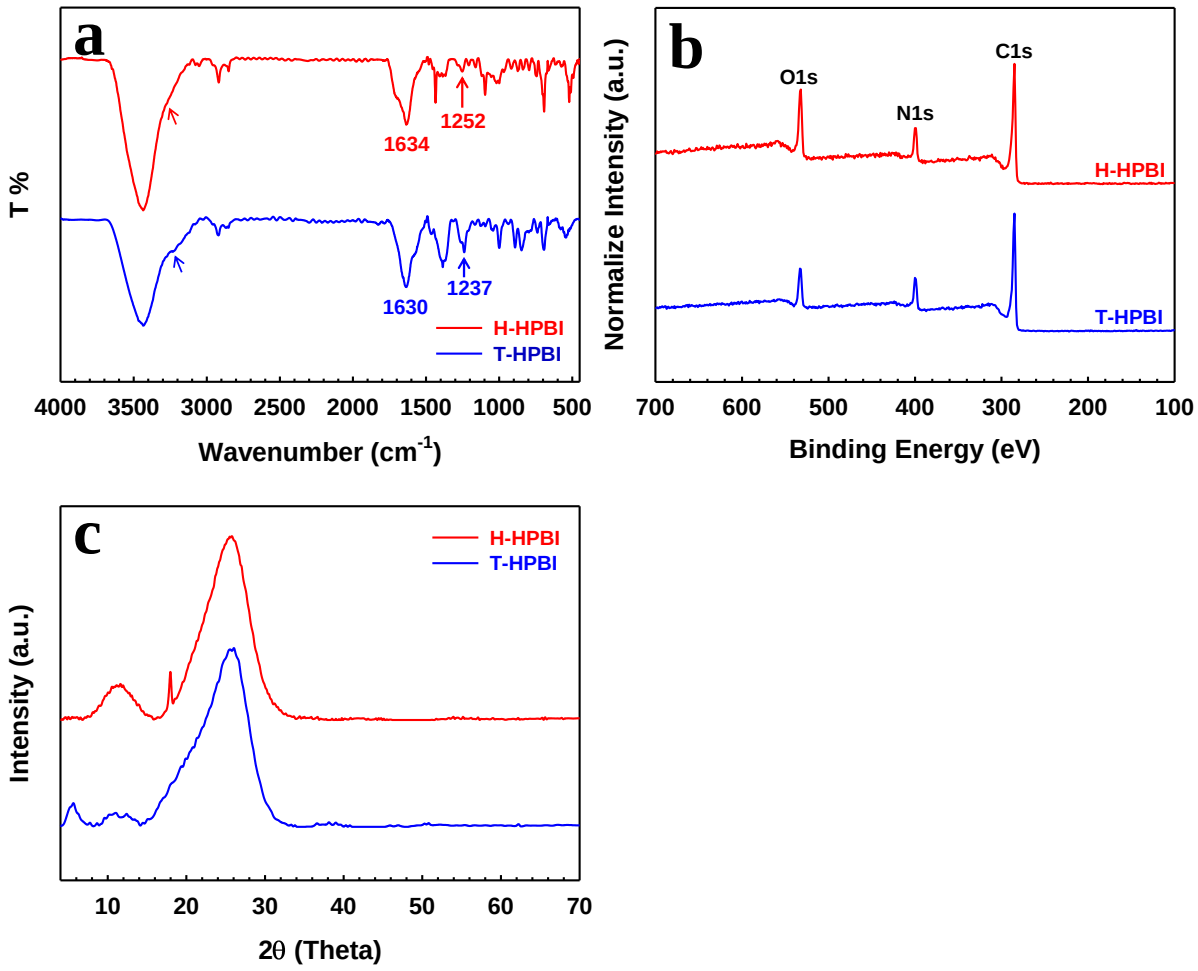

Figure 2.5. (a) FT-IR (KBr pellet) spectra of HPBIs confirming the formation of benzimidazole linkage. (b) XPS survey spectra of HPBIs. (c) Powder XRD diffraction patterns of HPBIs.

As schematically shown in **Figure 2.1** and **Figure 2.2**, two-dimensional polybenzimidzoles was synthesized from hexaaminobenzene and from tetraaminobenzene in PPA (see experimental details in experimental section). In the reaction, PPA, which is week acid, act as catalyst for condensation polymerization and as solvent for homogenous condition.

The chemical connectivity and the formation of the benzimidazole ring was confirmed by FT-IR and XPS. The spectra of HPBIs show in **Figure 2.5a**. The broad band at 3431 cm^{-1} (H-HPBI), 3427 cm^{-1}

(T-HPBI) is presumably due to the overlap of free N-H stretching at edge of HPBIs and hydroxyl group (-OH) from trapped water in HPBIs. The shoulder peaks at around 3270 cm^{-1}(H-HPBI) and 3233 cm^{-1} (T-HPBI) is assigned to hydrogen bonded N-H stretching. The band at 1630 cm^{-1} and 1252 cm^{-1} in H-HPBI are due to the stretching of C=N and stretching of C-N respectively. The same stretching are founded in T-HPBI at 1635 cm^{-1} [32] and 1237 cm^{-1} [33]. Skeleton vibration of benzimidazole ring at 1437 cm^{-1} (H-HPBI) and 1383 cm^{-1} (T-HPBI) [34-35]. The bends ranging 2830-2950 cm^{-1} are due to aromatic C-H stretching. X-ray photoelectron spectroscopy (XPS) measurements were performed to estimate the chemical composition of HPBIs. The XPS survey spectra of HPBIs (**Figure 2.5b**) present three dominant peaks centered at 284.5, 339.5 and 532.4 eV, corresponding to the presence of C1s, N1s and O1s, respectively. As shown in **Figure 2.6**, the C1s XPS spectra of HPBIs consist of three peaks arising from C=C (284.6 eV), C-N (285.6 eV) and O=C-OH (288.4 eV). The bonding configurations of nitrogen atoms in HPBIs were further investigated by high-resolution N1s XPS spectra in **Figure 2.6b and e**. The N1s peaks of both H-HPBI and T-HPBI could be fitted as two peaks, which correspond to C-N and C=N from benzimidazole ring in HPBIs.

Elemental composition of HPBIs was measured by elemental analysis (EA) and XPS. As a result, nitrogen content of T-HPBI is well matched with calculated from repeating unit but that of H-HPBI is not matched with calculated value. Although nitrogen content of H-HPBI is theoretically higher than T-HPBI, the nitrogen contents of H-HPBI is lower than that of T-HPBI because of structural stereo hindrance of H-HPBI during the reaction. Due to unreacted carboxylic acid in H-HPBI, oxygen content increased nitrogen content decreased. The same phenomena was observed in energy dispersive X-ray spectroscopy (EDS) and element mapping in **Figure 2.10** (H-HPBI) and **Figure 2.11** (T-HPBI).

Wide-angle X-ray diffraction (XRD) patterns (**Figure 2.5c**) were applied to H-HPBI and T-HPBI to determine the crystallinity of HPBIs. The highest peaks are shown at 25.78 º (3.45 Å) in H-HPBI and 25.77 º (3.45 Å) in T-HPBI. As a result, we can expect the two dimensional HPBIs are stacked like as graphite[36] with d-spacing of 3.35 Å between interlayer and as nitrogenated holy two-dimensional

structures[37] with d-spacing of 3.28 Å . The well stacked sheets of both HPBIs can be founded from field-emission scanning electron microscopy (SEM) in **Figure 2.9.**

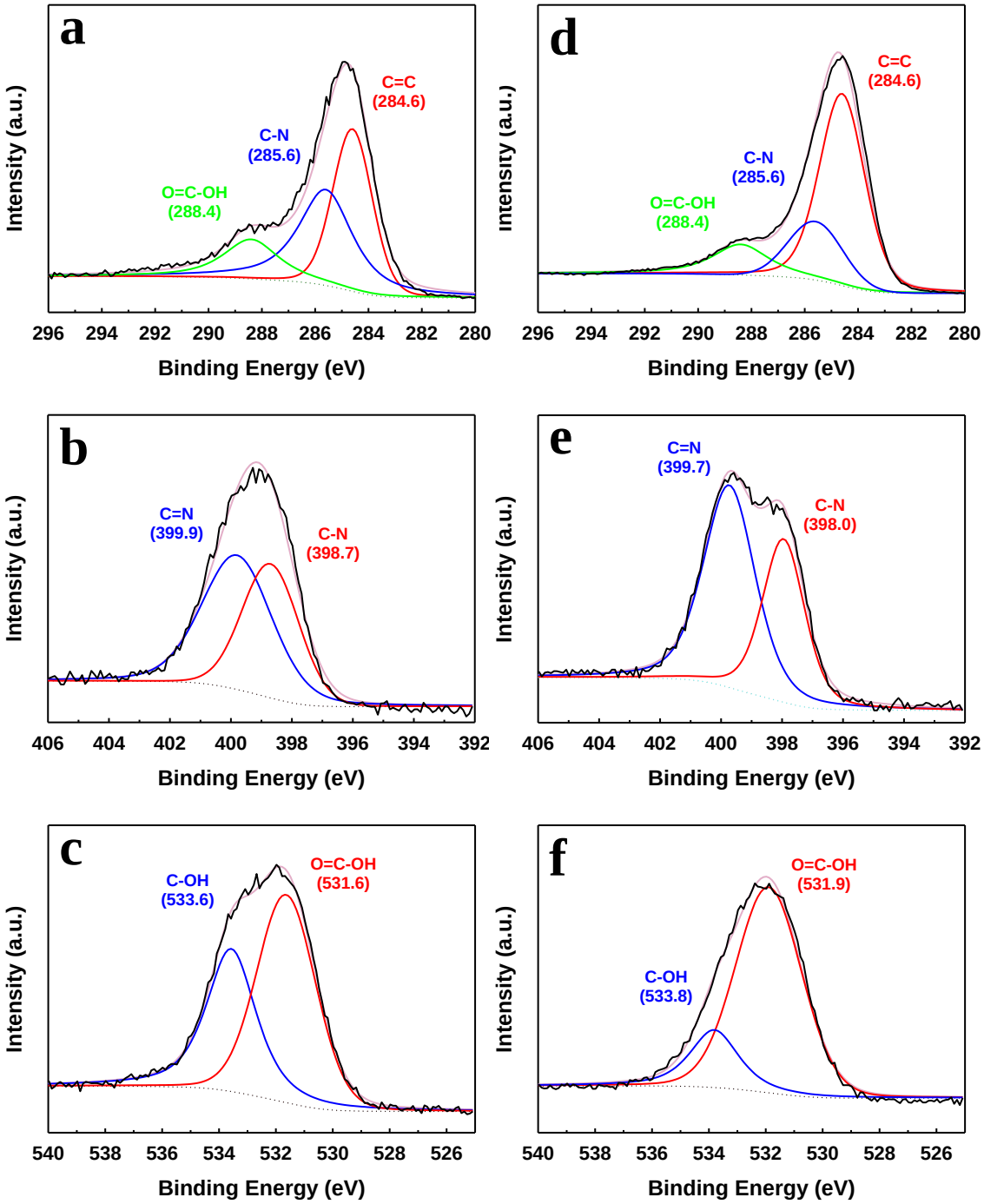

Figure 2.6. (a-c) High resolution XPS spectra of H-HPBI: (a) C1s, (b) N1s and (c) O1s. (d-f) High resolution XPS spectra of T-HPBI: (a) C1s, (b) N1s and (c) O1s.

Table 2.1. Elemental composition of HPBIs from Elemental analysis and XPS.

Sample		Elemental analysis[b] (wt %)				XPS[c] (at %)		
		C	H	N	O	C	N	O
H-HPBI	Calcd.[a]	58.52	3.29	27.44	10.45	65.22	26.09	8.69
	Found	57.59	2.37	17.08	22.37	70.91	11.12	17.91
T-HPBI	Calcd.[a]	66.05	3.39	25.68	4.89	72.00	24.00	4.00
	Found	61.34	3.18	22.88	10.75	74.31	12.83	12.73

[a] Calculation from repeating unit (see **Figure 2.7**)

[b] EA is most reliable element counts for bulk sample. The more oxygen content of HPBIs is induced by adsorbed moisture and oxygen.

[c] XPS is more sensitivity to surface chemical composition.

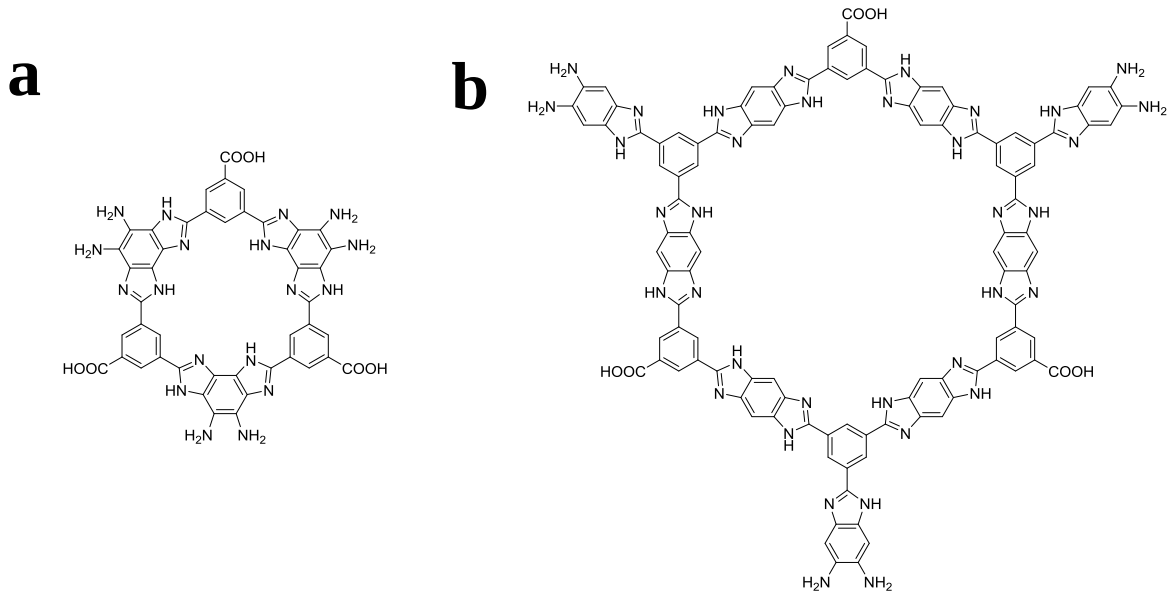

Figure 2.7. Repeating units of HPBIs: (a) H-HPBI and (b) T-HPBI

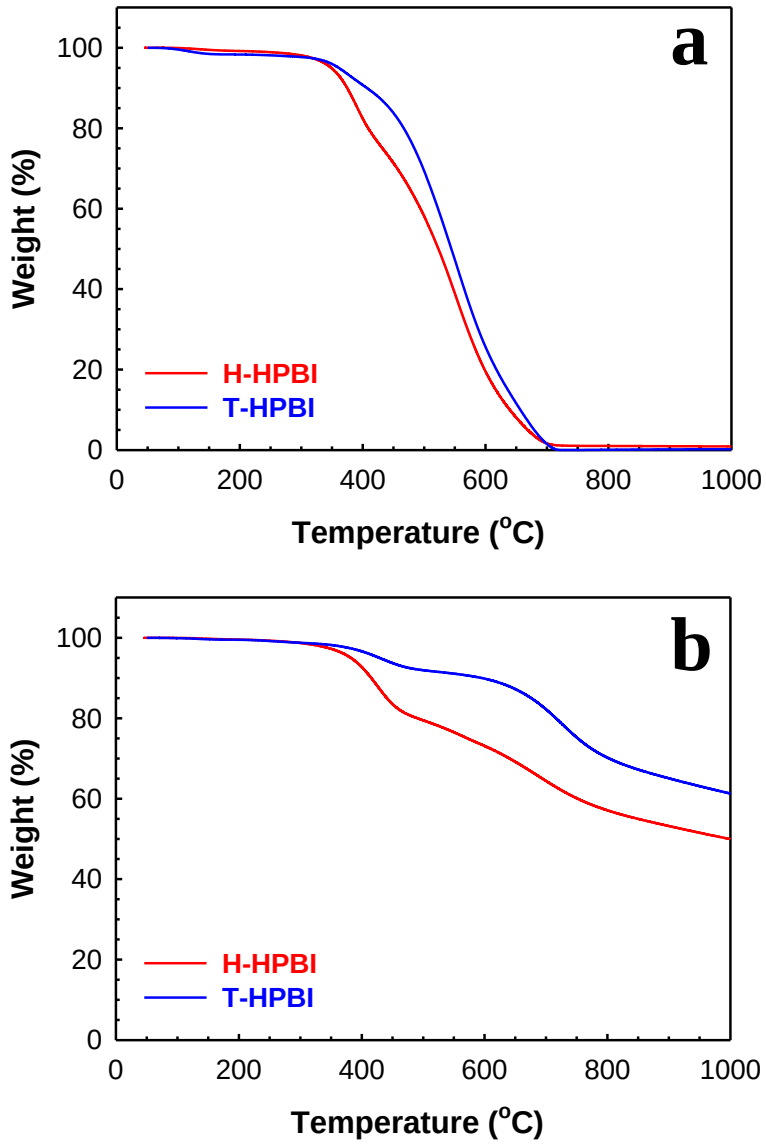

Figure 2.8. TGA thermograms of HPBIs in air (a) and nitrogen (b) atmosphere. Which was measured after pre-annealing to 200 ℃ (20 ℃/min) to remove trapped water in materials and the heating rate is 10 ℃/min.

The thermal stabilities of HPBIs were determined by TGA and the test performed under air and nitrogen atmosphere. HPBIs for TGA analysis were preheated to 200 ℃ at 20 ℃/min and gradually cooled to room temperature for moisture removal. As can be seen in **Figure 2.8a**, we found that the degradation temperature (T_d) of T-HPBI is higher than H-HPBI (T_d of H-HPBI = 354 ℃, T_d of T-HPBI = 375 ℃) in air atmosphere. Both HPBIs show quite high thermo-oxidative stability because of the effect of strong molecular packing structure induced by both hydrogen bonds and π-π interaction between 2-dimensional HPBI sheets [38]. The degradation of HPBIs displayed two steps in nitrogen atmosphere as shown in **Figure 2.8b**. The first weight loss region around 340-460 ℃ was assigned to result from decomposition of the carboxylic acid at the edge of HPBIs. In the region, the high char yield of T-HPBI (93.1 wt %) was much higher than that of H-HPBI (82.8 wt %) due to higher oxygen content. The result agreed well with the EA, XPS and EDS spectra (see **Table 2.2, Figure 2.5b and Figure 2.10 and 2.11**). In the second weight loss region, benzimidazole ring were further degraded at around 460-800 ℃, which corresponds to the decomposition of the main structure of HPBIs. At 1000 ℃, char yield of H-HPBI and T-HPBI was 50.1 wt % and 61.6 wt % respectively.

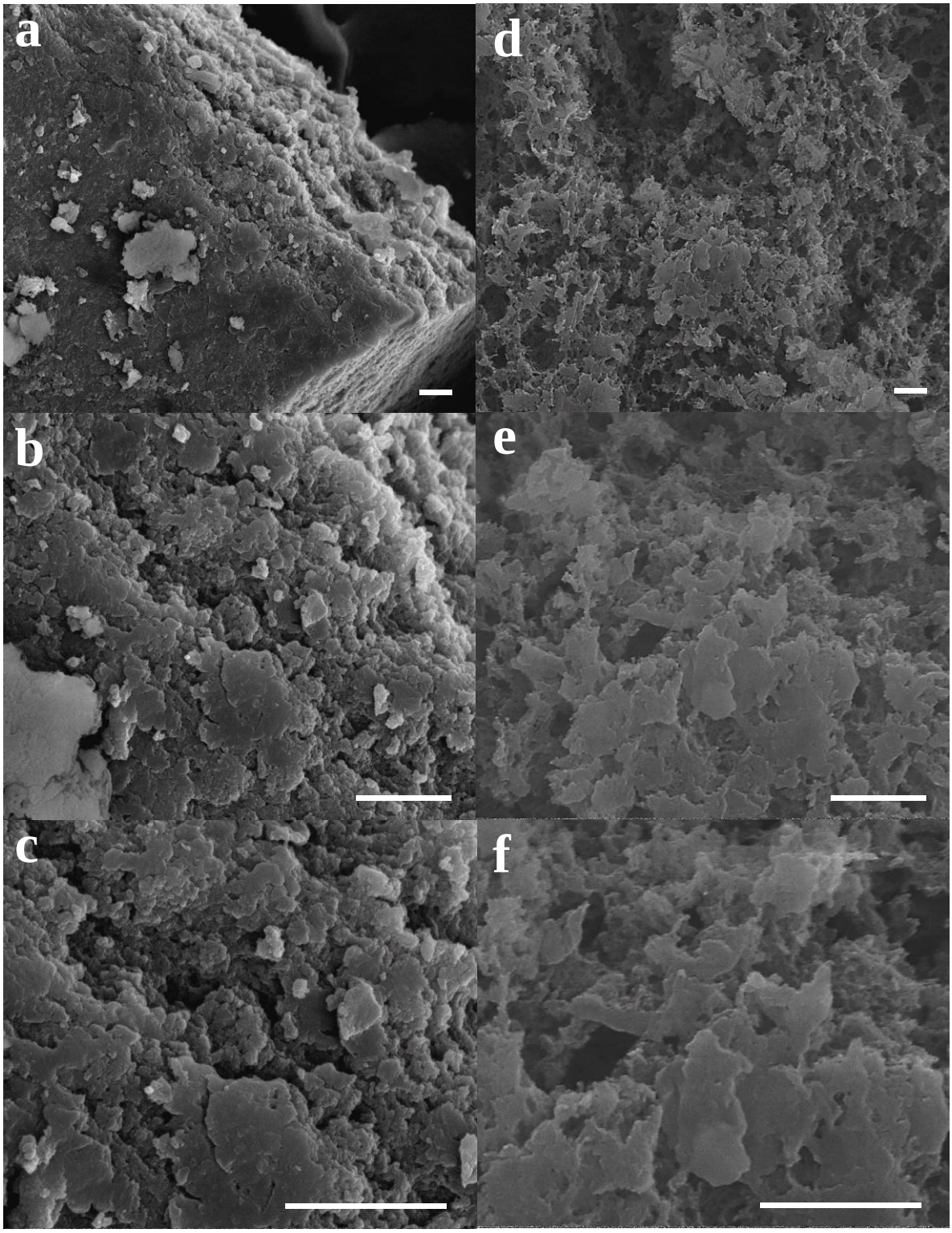

Figure 2.9. SEM images of HPBIs: (a-c) H-HPBI and (d-f) T-HPBI. Scale bars are 1 μm.

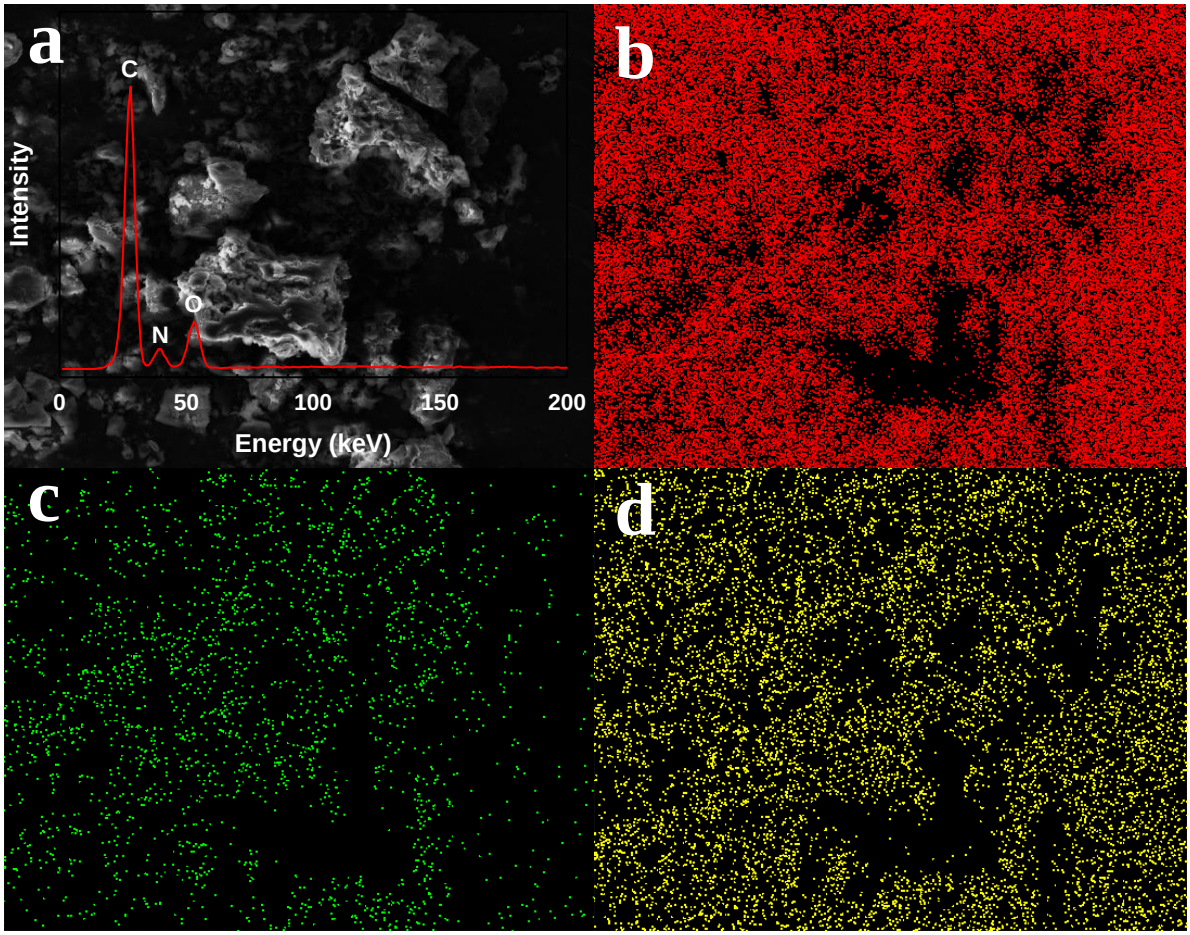

Figure 2.10. (a) SEM image and EDAX spectrum without Platinum (Pt) of H-HPBI. (b-d) The corresponding mapping of image (a).

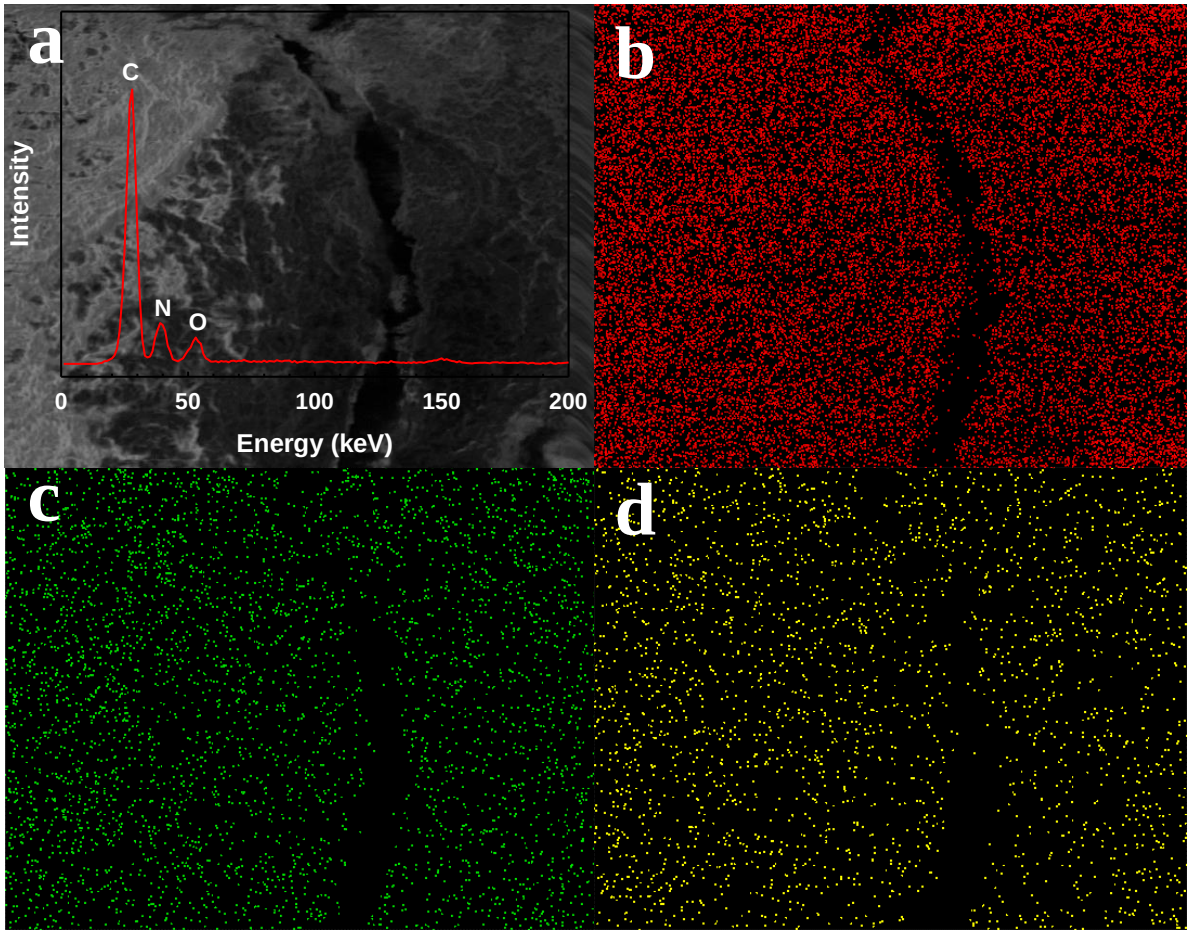

Figure 2.11. (a) SEM image and EDAX spectrum without Platinum (Pt) of T-HPBI. (b-d) The corresponding mapping of image (a).

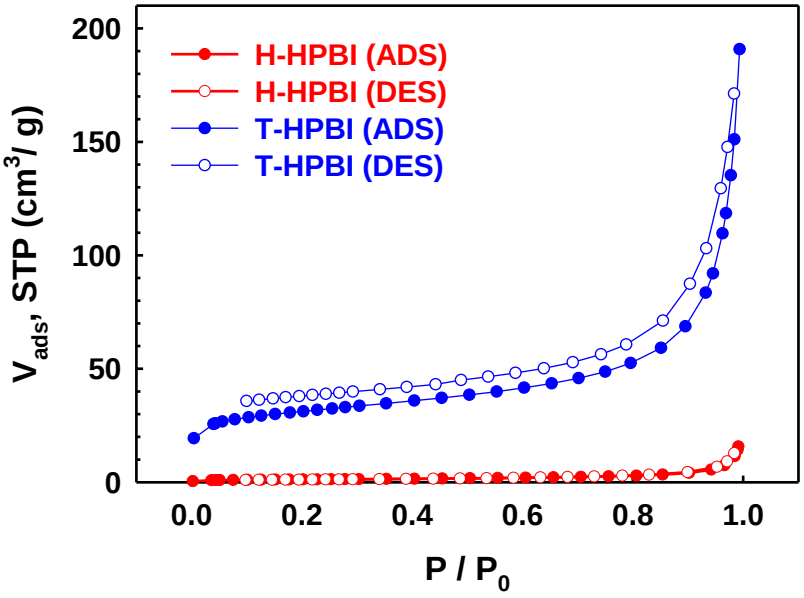

Figure 2.12. Nitrogen adsorption (solid) and desorption (open) isotherms of H-HPBI (red) and T-HPBI (blue) at 77 K.

As shown in **Figure 2.12**, nitrogen gas adsorption/ desorption isotherms of HPBIs at 77 K was collected. The Brunauer-Emmett-Teller specific surface area (S_{BET}) of H-HPBI and T-HPBI were 4.338 m^2/g and 113.0 m^2/g, respectively. Surface area of H-HPBI is smaller than that of T-HPBI because unreacted carboxylic acid in H-HPBI occupied most of the room in hole. T-HPBI with large surface area is expected to bring good electrochemical and device performance due to its large active area. The sorption isotherm of T-HPBI is a type III, which indicate mesopores.[39]

Table 2.2. Specific surface areas, pore volumes and pore sizes of HPBIs.

	Surface Area (m^2/g)	**Pore Volume (mL/g)**	**Pore Size (Å)**
H-HPBI	4.338	0.022	202.9
T-HPBI	113.0	0.272	96.27

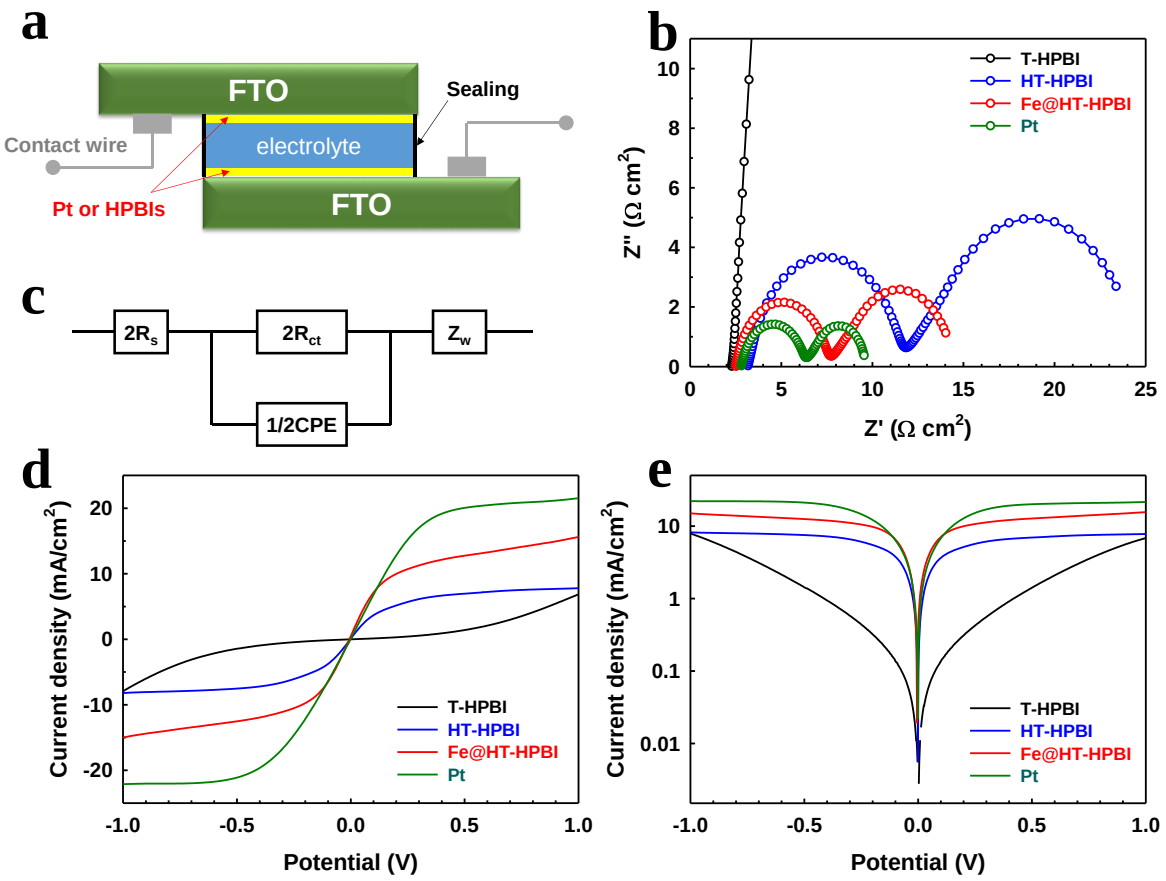

Figure 2.13. (a) Typical structure of a symmetrical dummy cell with two identical electrodes, (b) Nyquist plots of EIS measured at 0V from 10^6 Hz to 0.1 Hz on the symmetrical dummy cells with the Pt and HPBIs, (c) Equivalent circuit diagram for fitting the EIS data, (d) Cyclic voltamograms obtained at a scan rate of 10 mV/s, (e) Tafel polarization curves of PT and HPBIs dummy cells.

Electrochemical performances of HPBIs for potential application in DSSCs was evaluated. We prepared thin films of HPBIs on fluorine-doped SnO_2 (FTO)/glass by electrostatic spray (e-spray) technique.[16] Pt-coated FTO as the reference electrodes for comparison with HPBI film performance were also fabricated. The R_{CT} at the CE/electrolyte interface which is measure by electrochemical impedance spectroscopy (EIS) using a dummy cell (**Figure 2.13a**).[40-41] is a very useful parameter to check electrocatalytic activities of CE in DSSCs.[3, 11, 40-41] As shown in equation (1), the exchange current density $J_{0,}$ varies inversely with R_{CT}, where R is the ideal gas constant, T is the absolute temperature, n is the number of electrons, and F is the Faraday constant.

$$J_0 = \frac{RT}{nFR_{CT}} \quad (1)$$

The Nyquist plots in **Figure 2.13b** obtained from the symmetrical dummy cells. The EIS parameters were calculated from the semicircles appeared at the first high-frequency domain using an equivalent circuit (EC, **Figure 2.13c**) The R_{CT} of the T-HPBI (R_{CT} = 398.5 Ω cm^2) show about 93 times larger than that of the HT-HPBI (R_{CT} = 4.247 Ω cm^2), which is heat-treated at 400 ℃ for 1 hr in argon atmosphere. Such a dramatic change after heat-treatment was induced by reducing carboxyl group, hindrance of interaction between CE and electrolyte, during annealing. After adding 10^{-2} wt% iron in T-HPBI and heating at 400 ℃ for 1 hr in Ar, the R_{CT} of the Fe@HT-HPBI (R_{CT} = 2.536 Ω cm^2) decreased by 40 percent compared to HT-HPBI because of the electrocatalytic activity of iron in benzimidazole based polymer. The Fe@HT-HPBI displayed the EIS parameters, R_S = 1.24 Ω cm^2, R_{CT} = 2.54 Ω cm^2, CPE:1/B(Ss^{β}) = 4.01 × 10^5, and CPE:β = 0.57. Although the electrocatalytic activity of Fe@HT-HPBI is lower than Pt, the activity of T-HPBI dramatically improved after heating and adding additives. The corresponding J_0 values, calculated from equation (1), were 0.06 mA cm^{-2} (T-HPBI), 6.04 mA cm^{-2} (HT-HPBI), 10.12 mA cm^{-2} (Fe@HT-HPBI) and 14.77 mA cm^{-2} (Pt) in that order (**Table 2.3**).

Additional data in regard of electrocatalytic activities were examined by cyclic voltammetry (CV) in **Figure 2.13d**. The inverse slope of a voltammogram at around 0 V potential was determined to characterize the catalytic activity of a CE (**Figure 2.13d**). The overall cell resistance (R_{CV}) at low current densities can be estimated.[42] The voltammogram of the Fe@HT-HPBI dummy cell exhibits a steeper slope than that of the HT-HPBI cell.

Table 2.3. EIS parameters of symmetrical dummy cells with the Pt/- and HPBIs/FTO electrodes and exchange current density (J_0) calculated from R_{CT} values. R_S is the sheet resistance and CPE is the constant phase element.

CE	R_S [Ω cm^2]	R_{CT} [Ω cm^2]	CPE:1/B (Ssβ)	CPE:β	J_0 [mA/cm^2]
T-HPBI	1.151	398.5	1.17×10^{-5}	0.8863	0.06
HT-HPBI	1.570	4.247	1.15×10^{-5}	0.8824	6.04
Fe@HT-HPBI	1.239	2.536	1.19×10^{-5}	0.5698	10.12
Pt	1.391	1.739	4.01×10^{-5}	0.9548	14.77

2.6 Conclusion

In summary, two-dimensional holy benzimidazole based polymers (HPBIs) were well synthesized in PPA medium. H-HPBI from hexaaminobenzene was not well synthesized and have low surface area (4.338 m^2/g) because of structural stereo hindrance of H-HPBI. T-HPBI from tetraaminobenzene, on the other hand, was well synthesized and have large surface area (113.0 m^2/g). The resultant T-HPBIs were tested as cathode electrodes for $Co(bpy)_3^{3+}$ reduction reaction in DSSCs. We confirmed effect of thermal treatment and effect of 10^{-2} wt % iron additives for count electrode (CE) in dye sensitized solar cell (DSSC) to replace precious platinum (Pt). After heat-treatment at 400 ℃ for 1 hr in argon atmosphere, the R_{CT} of HT-HPBI (R_{CT} = 4.247 Ω cm^2) value dramatically decreased by 99 percent compared to T-HPBI (R_{CT} = 398.5 Ω cm^2) due to reducing carboxyl group. After adding 10^{-2} wt% iron in T-HPBI supports and heating at 400 ℃ for 1 hr in Ar, the R_{CT} of the Fe@HT-HPBI (R_{CT} = 2.536 Ω cm^2) decreased by 40 percent compared to HT-HPBI because of the electrocatalytic activity of iron in benzimidazole based polymer. Although the electrocatalytic activity of Fe@HT-HPBI is lower than Pt, the activity of T-HPBI dramatically improved after heating and adding additives. The corresponding J_0 values, calculated from equation (1), were 0.06 mA cm^{-2} (T-HPBI), 6.04 mA cm^{-2} (HT-HPBI), 10.12 mA cm^{-2} (Fe@HT-HPBI) and 14.77 mA cm^{-2} (Pt) in that order.

2.7 References

1. O'Regan, B.; Gratzel, M. A low-cost, high-efficiency solar cell based on dye-sensitized colloidal TiO2 films. *Nature* **1991,** *353* (6346), 737-740.

2. Gratzel, M. Photoelectrochemical cells. *Nature* **2001,** *414* (6861), 338-344.

3. Hagfeldt, A.; Boschloo, G.; Sun, L.; Kloo, L.; Pettersson, H. Dye-Sensitized Solar Cells. *Chemical Reviews* **2010,** *110* (11), 6595-6663.

4. Yun, S.; Hagfeldt, A.; Ma, T. Pt-Free Counter Electrode for Dye-Sensitized Solar Cells with High Efficiency. *Advanced Materials* **2014,** *26* (36), 6210-6237.

5. Yang, Z.; Chen, T.; He, R.; Guan, G.; Li, H.; Qiu, L.; Peng, H. Aligned Carbon Nanotube Sheets for the Electrodes of Organic Solar Cells. *Advanced Materials* **2011,** *23* (45), 5436-5439.

6. Han, J.; Kim, H.; Kim, D. Y.; Jo, S. M.; Jang, S.-Y. Water-Soluble Polyelectrolyte-Grafted Multiwalled Carbon Nanotube Thin Films for Efficient Counter Electrode of Dye-Sensitized Solar Cells. *ACS Nano* **2010,** *4* (6), 3503-3509.

7. Choi, H.; Kim, H.; Hwang, S.; Han, Y.; Jeon, M. Graphene counter electrodes for dye-sensitized solar cells prepared by electrophoretic deposition. *Journal of Materials Chemistry* **2011,** *21* (21), 7548-7551.

8. Jang, S.-Y.; Kim, Y.-G.; Kim, D. Y.; Kim, H.-G.; Jo, S. M. Electrodynamically Sprayed Thin Films of Aqueous Dispersible Graphene Nanosheets: Highly Efficient Cathodes for Dye-Sensitized Solar Cells. *ACS Applied Materials & Interfaces* **2012,** *4* (7), 3500-3507.

9. Kavan, L.; Yum, J. H.; Grätzel, M. Optically Transparent Cathode for Dye-Sensitized Solar Cells Based on Graphene Nanoplatelets. *ACS Nano* **2011,** *5* (1), 165-172.

10. Jia, R.; Chen, J.; Zhao, J.; Zheng, J.; Song, C.; Li, L.; Zhu, Z. Synthesis of highly nitrogen-doped hollow carbon nanoparticles and their excellent electrocatalytic properties in dye-sensitized solar cells. *Journal of Materials Chemistry* **2010,** *20* (48), 10829-10834.

11. Murakami, T. N.; Ito, S.; Wang, Q.; Nazeeruddin, M. K.; Bessho, T.; Cesar, I.; Liska, P.; Humphry-Baker, R.; Comte, P.; Péchy, P.; Grätzel, M. Highly Efficient Dye-Sensitized Solar Cells Based on Carbon Black Counter Electrodes. *Journal of The Electrochemical Society* **2006,** *153* (12), A2255-A2261.

12. Gong, K.; Du, F.; Xia, Z.; Durstock, M.; Dai, L. Nitrogen-Doped Carbon Nanotube Arrays with High Electrocatalytic Activity for Oxygen Reduction. *Science* **2009,** *323* (5915), 760-764.

13. Qu, L.; Liu, Y.; Baek, J.-B.; Dai, L. Nitrogen-Doped Graphene as Efficient Metal-Free Electrocatalyst for Oxygen Reduction in Fuel Cells. *ACS Nano* **2010,** *4* (3), 1321-1326.

14. Jeon, I.-Y.; Choi, H.-J.; Ju, M. J.; Choi, I. T.; Lim, K.; Ko, J.; Kim, H. K.; Kim, J. C.; Lee, J.-J.; Shin, D.; Jung, S.-M.; Seo, J.-M.; Kim, M.-J.; Park, N.; Dai, L.; Baek, J.-B. Direct nitrogen fixation at the edges of graphene nanoplatelets as efficient electrocatalysts for energy conversion. *Scientific Reports* **2013,** *3*, 2260.

15. Jeon, I.-Y.; Yu, D.; Bae, S.-Y.; Choi, H.-J.; Chang, D. W.; Dai, L.; Baek, J.-B. Formation of Large-Area Nitrogen-Doped Graphene Film Prepared from Simple Solution Casting of Edge-Selectively Functionalized Graphite and Its Electrocatalytic Activity. *Chemistry of Materials* **2011,** *23* (17), 3987-3992.

16. Ju, M. J.; Kim, J. C.; Choi, H.-J.; Choi, I. T.; Kim, S. G.; Lim, K.; Ko, J.; Lee, J.-J.; Jeon, I.-Y.; Baek, J.-B.; Kim, H. K. N-Doped Graphene Nanoplatelets as Superior Metal-Free Counter Electrodes for Organic Dye-Sensitized Solar Cells. *ACS Nano* **2013,** *7* (6), 5243-5250.

17. Ju, M. J.; Jeon, I.-Y.; Kim, J. C.; Lim, K.; Choi, H.-J.; Jung, S.-M.; Choi, I. T.; Eom, Y. K.; Kwon, Y. J.; Ko, J.; Lee, J.-J.; Kim, H. K.; Baek, J.-B. Graphene Nanoplatelets Doped with N at its

Edges as Metal-Free Cathodes for Organic Dye-Sensitized Solar Cells. *Advanced Materials* **2014,** *26* (19), 3055-3062.

18**.** Kuhn, P.; Forget, A.; Su, D.; Thomas, A.; Antonietti, M. From Microporous Regular Frameworks to Mesoporous Materials with Ultrahigh Surface Area: Dynamic Reorganization of Porous Polymer Networks. *Journal of the American Chemical Society* **2008,** *130* (40), 13333-13337.

19**.** Kuhn, P.; Kruger, K.; Thomas, A.; Antonietti, M. "Everything is surface": tunable polymer organic frameworks with ultrahigh dye sorption capacity. *Chemical Communications* **2008,** (44), 5815-5817.

20**.** Bojdys, M. J.; Jeromenok, J.; Thomas, A.; Antonietti, M. Rational Extension of the Family of Layered, Covalent, Triazine-Based Frameworks with Regular Porosity. *Advanced Materials* **2010,** *22* (19), 2202-2205.

21**.** Uribe-Romo, F. J.; Hunt, J. R.; Furukawa, H.; Klöck, C.; O'Keeffe, M.; Yaghi, O. M. A Crystalline Imine-Linked 3-D Porous Covalent Organic Framework. *Journal of the American Chemical Society* **2009,** *131* (13), 4570-4571.

22**.** Schwab, M. G.; Fassbender, B.; Spiess, H. W.; Thomas, A.; Feng, X.; Müllen, K. Catalyst-free Preparation of Melamine-Based Microporous Polymer Networks through Schiff Base Chemistry. *Journal of the American Chemical Society* **2009,** *131* (21), 7216-7217.

23**.** Ding, S.-Y.; Gao, J.; Wang, Q.; Zhang, Y.; Song, W.-G.; Su, C.-Y.; Wang, W. Construction of Covalent Organic Framework for Catalysis: Pd/COF-LZU1 in Suzuki–Miyaura Coupling Reaction. *Journal of the American Chemical Society* **2011,** *133* (49), 19816-19822.

24**.** Lefèvre, M.; Proietti, E.; Jaouen, F.; Dodelet, J.-P. Iron-Based Catalysts with Improved Oxygen Reduction Activity in Polymer Electrolyte Fuel Cells. *Science* **2009,** *324* (5923), 71-74.

25**.** Matter, P. H.; Zhang, L.; Ozkan, U. S. The role of nanostructure in nitrogen-containing carbon catalysts for the oxygen reduction reaction. *Journal of Catalysis* **2006,** *239* (1), 83-96.

26. Ju, Y.-W.; Yoo, S.; Kim, C.; Kim, S.; Jeon, I.-Y.; Shin, J.; Baek, J.-B.; Kim, G. Fe@N-Graphene Nanoplatelet-Embedded Carbon Nanofibers as Efficient Electrocatalysts for Oxygen Reduction Reaction. *Advanced Science* **2015**, n/a-n/a.

27. Wu, G.; More, K. L.; Johnston, C. M.; Zelenay, P. High-Performance Electrocatalysts for Oxygen Reduction Derived from Polyaniline, Iron, and Cobalt. *Science* **2011,** *332* (6028), 443-447.

28. Shui, J.-L.; Karan, N. K.; Balasubramanian, M.; Li, S.-Y.; Liu, D.-J. Fe/N/C Composite in Li–O2 Battery: Studies of Catalytic Structure and Activity toward Oxygen Evolution Reaction. *Journal of the American Chemical Society* **2012,** *134* (40), 16654-16661.

29. Chen, L.; Yang, Y.; Jiang, D. CMPs as Scaffolds for Constructing Porous Catalytic Frameworks: A Built-in Heterogeneous Catalyst with High Activity and Selectivity Based on Nanoporous Metalloporphyrin Polymers. *Journal of the American Chemical Society* **2010,** *132* (26), 9138-9143.

30. Zhang, P.; Weng, Z.; Guo, J.; Wang, C. Solution-Dispersible, Colloidal, Conjugated Porous Polymer Networks with Entrapped Palladium Nanocrystals for Heterogeneous Catalysis of the Suzuki–Miyaura Coupling Reaction. *Chemistry of Materials* **2011,** *23* (23), 5243-5249.

31. Mahmood, J.; Kim, D.; Jeon, I.-Y.; Lah, M. S.; Baek, J.-B. Scalable Synthesis of Pure and Stable Hexaaminobenzene Trihydrochloride. *Synlett* **2013,** *24* (02), 246-248.

32. Rabbani, M. G.; El-Kaderi, H. M. Synthesis and Characterization of Porous Benzimidazole-Linked Polymers and Their Performance in Small Gas Storage and Selective Uptake. *Chemistry of Materials* **2012,** *24* (8), 1511-1517.

33. Rabbani, M. G.; El-Kaderi, H. M. Template-Free Synthesis of a Highly Porous Benzimidazole-Linked Polymer for CO2 Capture and H2 Storage. *Chemistry of Materials* **2011,** *23* (7), 1650-1653.

34. Sundaraganesan, N.; Ilakiamani, S.; Subramani, P.; Joshua, B. D. Comparison of experimental and ab initio HF and DFT vibrational spectra of benzimidazole. *Spectrochimica Acta Part A: Molecular and Biomolecular Spectroscopy* **2007,** *67* (3–4), 628-635.

35. Rabbani, M. G.; Reich, T. E.; Kassab, R. M.; Jackson, K. T.; El-Kaderi, H. M. High CO2 uptake and selectivity by triptycene-derived benzimidazole-linked polymers. *Chemical Communications* **2012,** *48* (8), 1141-1143.

36. Jeong, H.-K.; Lee, Y. P.; Lahaye, R. J. W. E.; Park, M.-H.; An, K. H.; Kim, I. J.; Yang, C.-W.; Park, C. Y.; Ruoff, R. S.; Lee, Y. H. Evidence of Graphitic AB Stacking Order of Graphite Oxides. *Journal of the American Chemical Society* **2008,** *130* (4), 1362-1366.

37. Mahmood, J.; Lee, E. K.; Jung, M.; Shin, D.; Jeon, I.-Y.; Jung, S.-M.; Choi, H.-J.; Seo, J.-M.; Bae, S.-Y.; Sohn, S.-D.; Park, N.; Oh, J. H.; Shin, H.-J.; Baek, J.-B. Nitrogenated holey two-dimensional structures. *Nat Commun* **2015,** *6*.

38. Totsatitpaisan, P.; Nunes, S. P.; Tashiro, K.; Chirachanchai, S. Investigation of the role of benzimidazole-based model compounds on thermal stability and anhydrous proton conductivity of sulfonated poly(ether ether ketone). *Solid State Ionics* **2009,** *180* (9–10), 738-745.

39. Sing, K. S. W.; Everett, D. H.; Haul, R. A. W.; Moscou, L.; Pierotti, R. A.; Rouquerol, J.; Siemieniewska, T. Reporting physisorption data for gas/solid systems with special reference to the determination of surface area and porosity. *Pure and Applied Chemistry* **1985,** *57* (4), 603-619.

40. Hauch, A.; Georg, A. Diffusion in the electrolyte and charge-transfer reaction at the platinum electrode in dye-sensitized solar cells. *Electrochimica Acta* **2001,** *46* (22), 3457-3466.

41. Papageorgiou, N.; Maier, W. F.; Grätzel, M. An Iodine/Triiodide Reduction Electrocatalyst for Aqueous and Organic Media. *Journal of The Electrochemical Society* **1997,** *144* (3), 876-884.

42. Liberatore, M.; Petrocco, A.; Caprioli, F.; La Mesa, C.; Decker, F.; Bignozzi, C. A. Mass transport and charge transfer rates for Co(III)/Co(II) redox couple in a thin-layer cell. *Electrochimica Acta* **2010,** *55* (12), 4025-4029.

III. New strategy via solid-state reaction for porous polymer synthesis (Formation of porous network polymer via solid-state explosion of organic single crystals)

3.1 Abstract

Solid-state reaction has considerable advantages over liquid-state process in manufacturing industry. However, due to limited possible systems, few researches have been done compared with liquid-state process. Here, we introduce a new synthetic protocol for the formation of porous network polymer *via* instant solid-state reaction of organic single crystals below their melting temperature. The reaction was realized by explosive cyclotrimerization of the ethynyl groups on 2,3,6,7,14,15-hexaethynyl-9,10-dihydro-9,10-[1,2]benzenoanthracene (HEA). The reaction is triggered by metastable crystal lattice energy below its crystal melting temperature. The driving force for the reaction is systematically studied with single-crystal X-ray diffraction and differential scanning calorimetry. The explosively polymerized HEA (polyHEA) displays high surface area of 1176 m^2 g^{-1} with the sorption capacity of carbon dioxide (CO_2) as high as 3.93 mmol/g at 273K (1 bar). Its isosteric heat of CO_2 adsorption is found to be 31.7 kJ mol^{-1} at zero coverage.

3.2 Introduction

Solid-state reaction of organic molecules has attracted a lot of interest due to its environmental advantages and sustainability.[1-2] The reaction can result in very pure product and post-treatment for purification is sometimes not necessary.[3] For these reasons, the solid-state reaction is very useful for commercial reality. However, although the maximum concentration of reactants in solid-state reaction usually can leads to more favorable kinetics than liquid-state reaction in solution, researches have seldom been exploited due to limited possible systems.[4]

Strategies for solid-state reaction can be induced by kinetic energy,[5] radiation[6] and heat-treatment[1] below melting temperature of substances. Recently, one of the strategies for solid-state reaction has been reported for the mass production of graphene nanoplatelets *via* mechanochemical ball-milling.[7] Similarly, metal organic frameworks (MOFs) have also been investigated through different mechanochemical methodologies such as neat grinding,[8] kneading[9] and grinding-annealing.[10] In addition, the syntheses of two-dimensional network polymers from crystalline monomers were carried out by photoradiation.[11-13]

On the other hand, there are numerous reported works that utilize different synthetic strategies to produce porous network polymers, including Sonogashira-Hagihara cross-coupling,[14-15] Sonogashira-Hagihara cross-coupling,[16-17] Suzuki cross-coupling,[18] Yamamoto coupling,[19-20] Friedel-Crafts alkylation,[21-22] click chemistry,[23] Gilch reaction,[24] benzimidazole formation,[25] Schiff-base chemistry,[26] imidization,[27-28] amidization,[27] cyclization of three ethynyl groups,[29-30] cyclization of three nitrile groups[31] and cyclization of three acetyl groups.[32] All methods are hydrothermally carried out in liquid-state reaction in solution in the presence of suitable catalyst(s). However, the study on thermally induced solid-state reaction have not yet been reported elsewhere in the field of porous network polymers. The resultant network polymers are expected to have high surface area, which can be useful for gas capture[33] and storage.[34]

Here, we introduce a new synthetic methodology for the fabrication of porous network polymer with high surface area *via* solid-state reaction of organic single crystals containing trigger molecules. The reaction involves cyclotrimerization of ethynyl groups using 2,3,6,7,14,15-hexaethynyl-9,10-dihydro-9,10-[1,2]benzenoanthracene (HEA), which has six ethynyl groups at its termini. Before the reaction, the structure of HEA single crystals was revealed by single-crystal X-ray diffraction (XRD) pattern, suggesting that acetone and water as trigger molecules are regularly positioned in the HEA crystal lattice. As like click reaction between ethynyl and azide groups,[23] thermally induced solid-state reaction of HEA single crystals was instantly completed within 0.11 s. Differential scanning calorimetry (DSC) study indicated that explosively high exothermic reaction heat was released during the short reaction time. The resultant polyHEA has high specific surface area of 1176 m^2/g. Its sorption capacity of carbon dioxide (CO_2) was reached as high as 3.93 mmol/g at 273 K (1 bar) and the isosteric heats of adsorption (Q_{st}) for CO_2 was found to be 31.7 kJ/mol at zero coverage.

3.3 Materials and Instrumentation

All the solvents, chemicals and reagents were purchased from Aldrich Chemical Inc., unless otherwise stated. Anhydrous i-Pr_2NH solvent was distilled from commercial i-Pr_2NH with CaH_2.

X-ray diffraction (XRD) studies were taken on High Power X-Ray Diffractometer, Rigaku, Japan and Single-Crystal X-ray diffractometer R-AXIS RAPID II, Rigaku, Japan. Differential scanning calorimetry (DSC) were recorded on a TA, Q200. Solid state 13C magic angle spinning (MAS) NMR spectrum was taken on 600 MHz FT-NMR, WNMRS 600, Agilent. Fourier transform infrared (FT-IR) spectra were recorded on Perkin-Elmer Spectrum 100 using KBr disks. X-ray photoelectron spectroscopy (XPS) was performed on X-ray Photoelectron Spectroscopy Thermo Fisher K-alpha (UK). Scanning electron microscope (SEM) images were taken on Field Emission Scanning Electron Microscope Nanonova 230 FEI, USA. Conventional transmission electron microscopy (TEM) was performed by using JEM-2100 (JEOL, Japan) under an operating voltage of 200 keV. The samples for TEM were prepared by drop casting Acetone dispersion on Quantifoil holey carbon TEM grid and dried in oven at 80 ℃. The surface area was measured by nitrogen adsorption-desorption isotherms using the Brunauer-Emmett-Teller (BET) method on Micromeritics ASAP 2504N. Element analyzer (EA) was performed on Flash 2000, Thermo. Themogravimetric analysis (TGA) was conducted in air and nitrogen atmospheres at a heating rate of 10 ℃/min using a Thermogravimetric Analyzer Q200 TA Instrument, USA.

3.4 Experiment Section

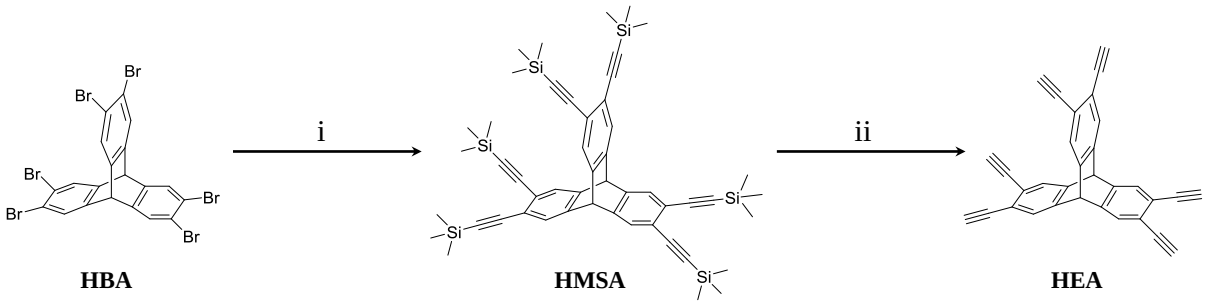

Figure 3.1. Synthesis of HEA from HBA. Reaction condition: (i) Trimethylsilylacetylene, CuI, $PdCl_2(PPh_3)_2$, PPh_3, i-Pr_2NH; (ii) NaOH / MeOH, CH_2Cl_2.

3.4.1 Synthesis of 2,3,6,7,14,15-hexabromo-9,10-dihydro-9,10-[1,2]benzenoanthracene (HBA) was prepared according to literature.[35]

3.4.2 Synthesis of 2,3,6,7,14,15-hexakis((trimethylsilyl)ethynyl)-9,10-dihydro-9,10-[1,2] (HMSA): 2,3,6,7,14,15-hexabromo-9,10-dihydro-9,10-[1,2]benzenoanthracene (2 g, 2.748 mmol), CuI (0.0312 g, 0.164 mmol), $PdCl_2(PPh_3)_2$ (0.1732 g, 0.247 mmol) and PPh_3 (0.1302 g, 0.496 mmol) was placed in a 250 mL round-bottom flask. Anhydrous i-Pr_2NH (150 mL) and trimethylsilylacetylene (4 mL, 28.1 mmol) was added. The reaction mixture was refluxed for 24 hr under a nitrogen atmosphere. After finishing of the reaction, the reaction mixture was cooled down to room temperature. The mixture was filtered through a pad of celite and washed with diethyl ether. Solvent was removed in vacuum, and CH_2Cl_2 was added to dissolve the residue and filtered through a pad of silica gel. The solution was concentrated in a rotary evaporator under vacuum and loaded to a silica gel column with ethyl acetate. Hexane/ethyl acetate (100:5 v/v) was used as an eluent. The solution was concentrated and yellow gel-type product (1.862 g, 81.7 % yield). ^{1}H NMR (400 MHz, $CDCl_3$, δ = ppm): 0.229 (26.71, Si-CH_3), 5.204 (1.00, CH), 7.396 (2.90, Ar-H). ^{13}C NMR (400 MHz, $CDCl_3$, δ = ppm): 0.146, 52.65, 98.38, 103.3, 123.6, 127.6, 143.4.

3.4.3 Synthesis of 2,3,6,7,14,15-hexaethynyl-9,10-dihydro-9,10-[1,2]benzenoanthracene (HEA): NaOH (0.7 g, 17.50 mmol) was dissolved in 20 mL methanol and added to a solution of 2,3,6,7,14,15-hexakis((trimethylsilyl)ethynyl)-9,10-dihydro-9,10-[1,2]benzenoanthracene (1 g, 1.202 mmol) in 20 mL CH_2Cl_2. The mixture was stirred for 12 h at room temperature. The solvent was removed in a rotary evaporator under vacuum. 30 mL CH_2Cl_2 was added to dissolve the residue and the white insoluble solid was filtered away. The filtrate was then washed with brine (20 mL). The organic solution was extracted with CH_2Cl_2 using a separation funnel, and then dried over anhydrous Na_2SO_4. The solution was concentrated in a rotary evaporator under vacuum and loaded to a silica gel column with ethyl acetate. Hexane/ethyl acetate (10:1 v/v) was used as an eluent, white solid powder (0.349 g, 72.9 %) was obtained after removing the solvent. As-grown HEA single crystals was conducted in slow evaporation system with the acetone/heptane at room temperature, because ethynyl group is unstable in heat. ^{1}H NMR (400 MHz, $CDCl_3$, δ = ppm): 3.266 (2.39,≡C-H), 5.330 (1.00, CH), 7.502 (2.69, Ar-H). ^{13}C NMR (400 MHz, $CDCl_3$, δ = ppm): 52.51, 82.37, 82.87, 123.6, 129.0, 145.4.

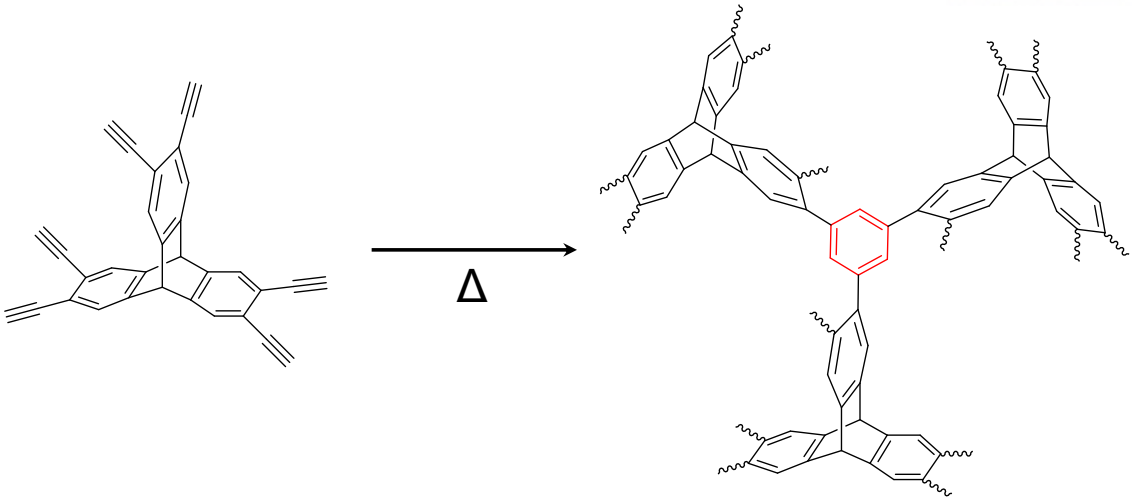

Figure 3.2. Synthesis of polyHEA from as-grown HEA single crystals.

3.4.4 Synthesis of polyHEA: as-grown HEA crystals (0.32 g) was placed in a 4L container under vacuum condition and was suddenly heated by heat-gun during a few second. At the end of the reaction, acetone was added into the flask. The resulting black polymer was collected by suction filtration, soxhlet extracted with acetone for 2 days to get rid of unreacted HEA, and then with water for 2 days. Finally, the sample was freeze-dried under reduced pressure (0.5 mmHg) at -120 ℃ for 2 days to give 0.298 g (96.2 % yield) of black powder.

3.5 Lattice energy in energy diagram

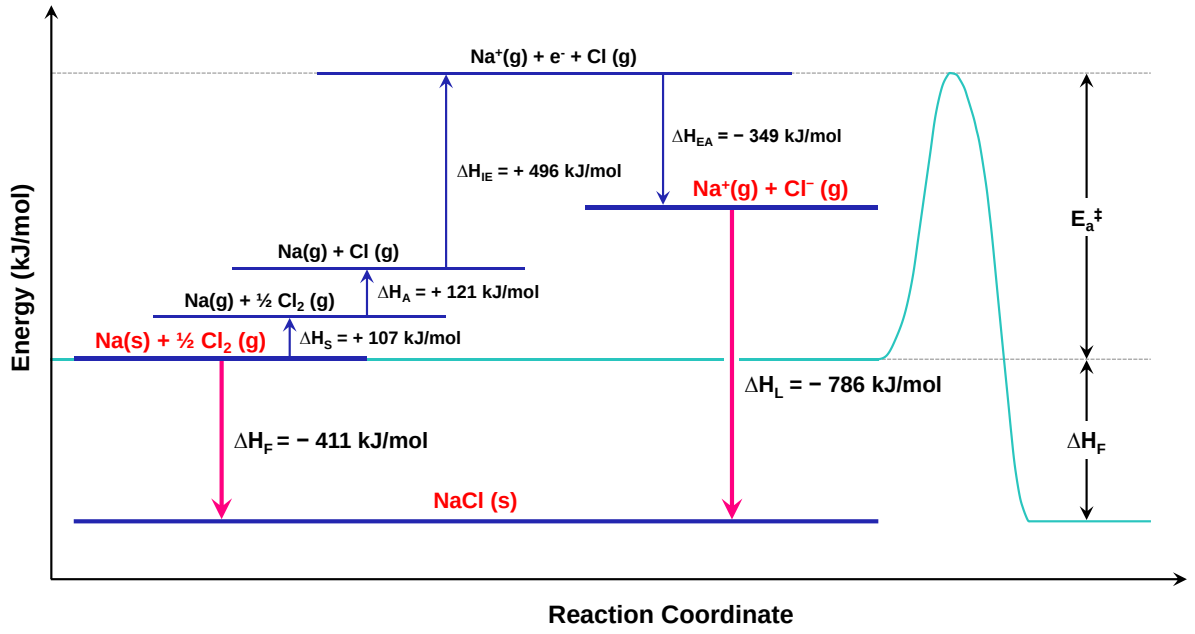

Figure 3.3. Energy diagram and Born Haber cycle for the formation of sodium chloride. ΔH_F: Enthalpy change of formation of sodium chloride; ΔH_S: Sublimation energy of sodium; ΔH_A: Enthalpy change of atomization of chlorine; ΔH_{IE}: Ionization energy of sodium; ΔH_{EA}: Enthalpy change of electron affinity of chlorine; ΔH_L: Lattice energy of sodium chloride; $E_a^{\ddagger}$: Activation energy of sodium chloride.

The definition of lattice energy is 'the energy of formation of the crystal from infinitely-separated ions'[36]. The measurement of the lattice energy may not be experimentally determined, because of the impossibility of preparing infinitely-separated ions and atoms and measuring the energy released during the formation of the crystal. However, the energy of lattice can be estimated from a thermodynamic cycling reaction (the Born-Haber cycle) theoretically.

For example, the lattice energy from ions of sodium and chlorine in gaseous state to ionic solid of sodium chloride can be calculated by the following equations (1) and (2):

$$\Delta H_F = \Delta H_S + \Delta H_A + \Delta H_{IE} + \Delta H_{EA} + \Delta H_L \qquad (\Delta H_F < 0) \qquad (1)$$

$$\therefore \Delta H_L = \Delta H_F - \Delta H_S - \Delta H_A - \Delta H_{IE} - \Delta H_{EA} \qquad (\Delta H_L < 0) \qquad (2)$$

As shown in Figure 3.3, the lattice energy of sodium chloride belongs to the combined regions of activation energy and formation energy of sodium chloride in energy diagram. On the other hand, as-grown HEA single crystals, which is crystals between molecules induced by molecular interaction, belongs to only activation energy region because the molecules of acetone and water in as-grown HEA single crystals not contribute to the reaction for cyclotrimerization from ethynyl group.

3.6 Crystallographic data collection and refinement of the structure

A crystal of as-grown HEA single crystals was coated with paratone oil and the diffraction data measured at 173 K with Mo Kα radiation on an X-ray diffraction camera system using an imaging plate equipped with a graphite crystal incident beam monochromator. The RapidAuto software [1] was used for data collection and data processing. Structure was solved by direct method and refined by full-matrix least-squares calculation with the SHELX software package. [37]

Nine HEAs, two acetone molecules and one water molecule are observed as an asymmetric unit. All non-hydrogen atoms are refined anisotropically; the hydrogen atoms were assigned isotropic displacement coefficients U(H) = 1.2U (C) and 1.5U (C_{methyl}), their coordinates were allowed to ride on their respective atoms. The least-squares refinement of the structural model was performed under geometry restraints and displacement parameter restraint such as DANG, DFIX, DELU, ISOR and SIMU.

Refinement of the structure converged at a final $R1 = 0.0889$ and $wR2 = 0.2391$ for 16856 reflections with $I > 2\sigma(I)$; $R1 = 01827$ and $wR2 = 0.3278$ for all 35246 reflections. The largest difference peak and hole were 0.708 and –0.363 e·Å $^{-3}$, respectively.

A summary of the crystal and some crystallography data is given in **Table 3.1**. CCDC-****** contains the supplementary crystallographic data for this paper. The data can be obtained free of charge at www.ccdc.cam.ac.uk/conts/retrieving.html or from the Cambridge Crystallographic Data Centre, 12, Union Road, Cambridge CB2 1EZ, UK.

[1] Rapid Auto software, R-Axis series, Cat. No. 9220B101, Rigaku Corporation.

Table 3.1. Crystal data and structure refinement for as-grown HEA single crystals

Empirical formula	$C_{294}H_{140}O_3$
Formula weight	3720.05
Temperature	173(2) K
Wavelength	0.71073 Å
Crystal system	Triclinic
Space group	*P*1
Unit cell dimensions	a = 13.739(3) Å α = 80.76(3)° b = 13.973(3) Å β = 78.58(3)° c = 32.901(7) Å γ = 61.52(3)°
Volume	5426(2) $Å^3$
Z	1
Density (calculated)	1.139 Mg/m^3
Absorption coefficient	0.066 mm^{-1}
F(000)	1928
Crystal size	0.320 x 0.300 x 0.170 mm^3
Theta range for data collection	3.018 to 24.999°.
Index ranges	–15<=h<=16, –16<=k<=16, –39<=l<=39
Reflections collected	69913
Independent reflections	35246 [R(int) = 0.0597]
Completeness to theta = 24.999°	99.4 %
Absorption correction	Semi-empirical from equivalents
Max. and min. transmission	0.989 and 0.979
Refinement method	Full-matrix least-squares on F^2
Data / restraints / parameters	35246 / 216 / 2666
Goodness-of-fit on F^2	1.029
Final R indices [I>2sigma(I)]	R1 = 0.0889, wR2 = 0.2391
R indices (all data)	R1 = 0.1827, wR2 = 0.3278
Absolute structure parameter	4.5(10)
Largest diff. peak and hole	0.708 and –0.363 e·$Å^{-3}$

3.7 Results and Discussion

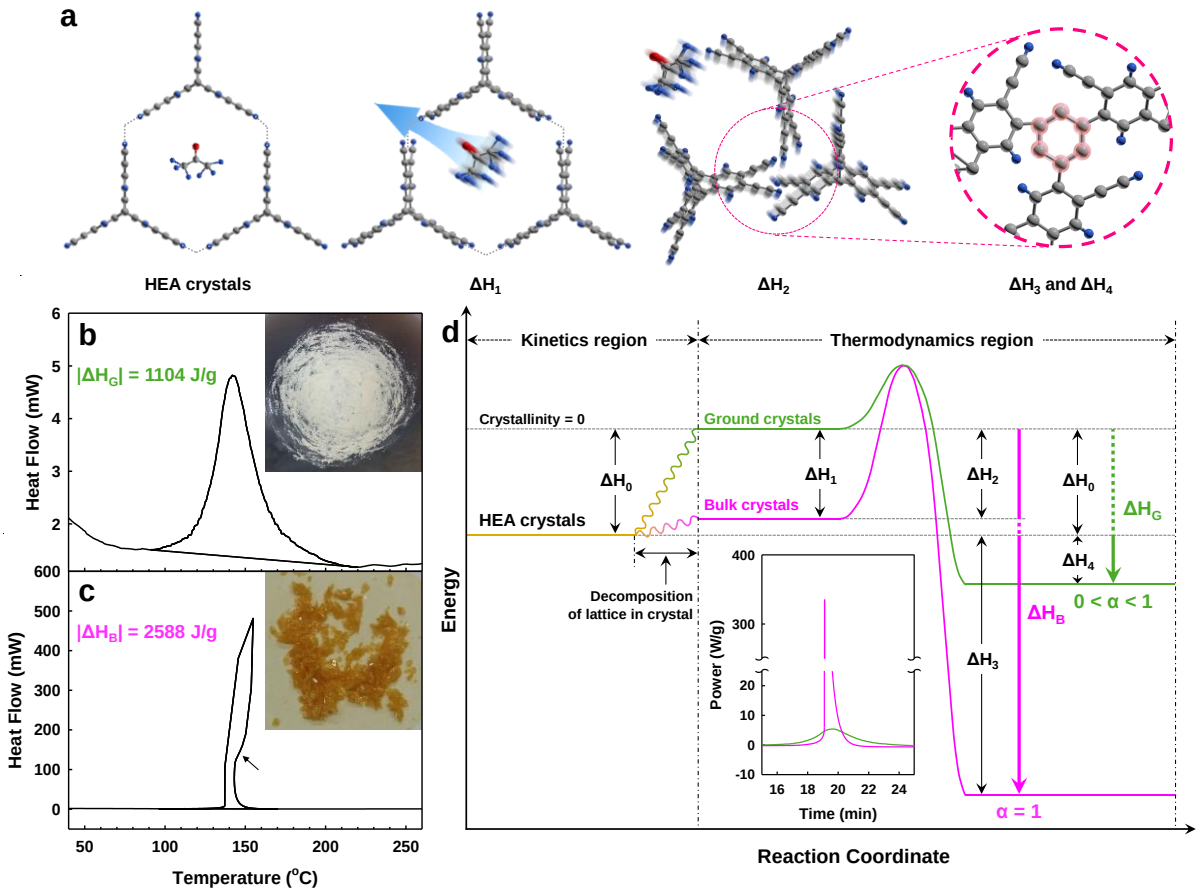

Figure 3.4. (a) Schematic representation of the reaction from as-grown HEA single crystals to polyHEA (gray: carbon, red: oxygen, blue: hydrogen). The dotted line represents lattice energy in crystal of as-grown HEA single crystal. DSC thermograms of samples obtained with a heating rate of 10 ℃ min^{-1}: (b) 1st heating scan of ground HEA crystals after grinding of as-grown bulk HEA single crystals. Inset is photograph of ground HEA crystals. (c) 1st heating scan of as-grown bulk HEA single crystals. Inset is photograph of bulk HEA single crystals. (d) Energy diagrams of as-grown bulk and ground HEA single crystals based on DSC thermograms. ΔH_0: Lattice energy in bulk and ground HEA single crystals. In case of ground HEA crystals with high surface area, the lattice is completely decomposed but the lattice of bulk HEA crystals is partially decomposed during heating with 10 ℃/min. Consequentially, lattice energy between ground and bulk HEA crystal is different at the moment of reaction due to

kinetics difference according to difference of crystal size. ΔH_1: Included lattice energy in bulk HEA crystals at the time of reaction. In this step, the lattice in crystal absorb kinetic energy from trapped acetone and water during heating. ($\Delta H_1 > 0$, ΔH_1: enthalpy change in state 1) ΔH_2: Absorbed lattice energy in bulk HEA crystals is released as heat energy and kinetic energy of molecules ($\Delta H_2 < 0$). ΔH_3: Cyclotrimerization of entire ethynyl groups in HEA occur ($\Delta H_3 < 0$, $\alpha = 1$, α: conversion ratio of ethynyl groups in HEA). ΔH_4: Cyclotrimerization of neighboring ethynyl groups in HEA occur ($\Delta H_4 < 0$, $0 < \alpha < 1$, $|\Delta H_4| << |\Delta H_3|$). ΔH_B is enthalpy change of as-grown bulk HEA crystals ($\Delta H_B = \Delta H_2 + (\Delta H_0 - \Delta H_2) + \Delta H_3$, $|\Delta H_B| = 2.34|\Delta H_G|$). ΔH_G is enthalpy change of ground HEA crystals ($\Delta H_G = \Delta H_0 + \Delta H_4$). Inset is DSC thermograms of as-grown bulk (pink) and ground (green) HEA single crystals showing amount of exothermic heat with respect to time.

The key monomer, 2,3,6,7,14,15-hexaethynyl-9,10-dihydro-9,10-[1,2]benzenoanthracene (HEA), was prepared in three steps (see experimental details in Supporting Information). In brief, the bromination of triptycene[38] and subsequent ethynylation to yield unique three-dimensional HEA structure. The single crystals of HEA for solid-state reaction were obtained from very slow recrystallization in heptane/acetone mixture. The color of as-grown HEA single crystals is light yellow (inset, **Figure 3.4c**).

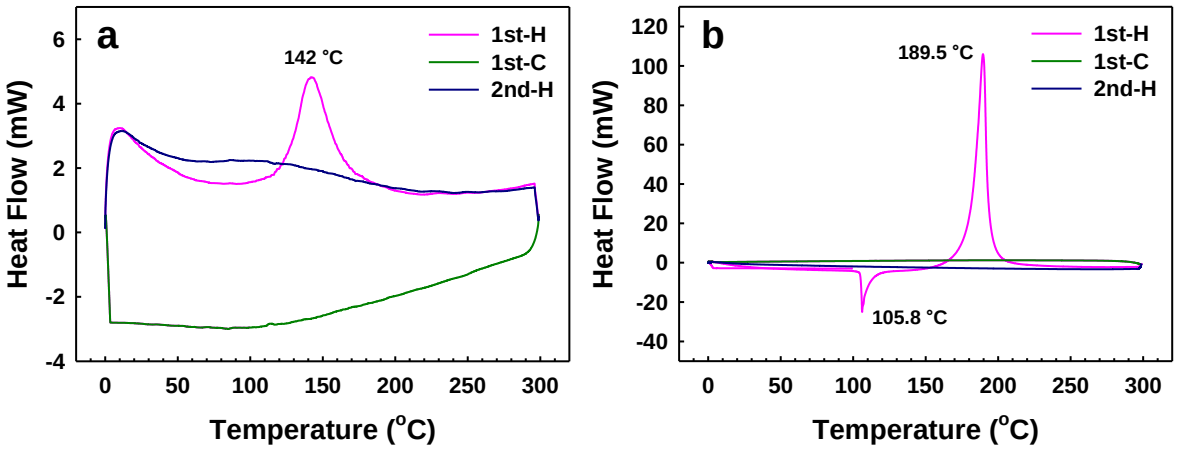

Figure 3.5. DSC thermograms obtained with a ramping rate of 10 ℃/min under nitrogen: (a) Ground HEA crystals and (b) Triethynylbenzene.

Thermal behaviors of HEA single crystals were studied by differential scanning calorimetry (DSC). Typical organic single crystals display a sharp and narrow endothermic crystal melting peak. For example, 1,3,5-triethynylbenzene, which is representative monomer for cyclotrimerization of ethynyl groups, shows endothermic melting peak at 105.8 ℃ and then exothermic cyclization peak at 189.5 ℃ (**Figure 3.5b**). However, as-grown bulk HEA single crystals display unusual thermal behavior, showing a strong exothermic peak at 137.5 ℃ before its melting (**Figure 3.4c**). To figure out the origin of unusual thermal behavior of HEA, as-grown bulk HEA single crystal was subject to be characterized using single-crystal X-ray diffraction (XRD, see detailed information in Supporting Information). The crystallographic asymmetric unit of single crystal consists of nine HEA molecules with two acetone molecules and one water molecule in the lattice (**Figure 3.6a**). The powder XRD pattern of HEA crystals is in good agreement with simulated XRD pattern (**Figure 3.6b**).

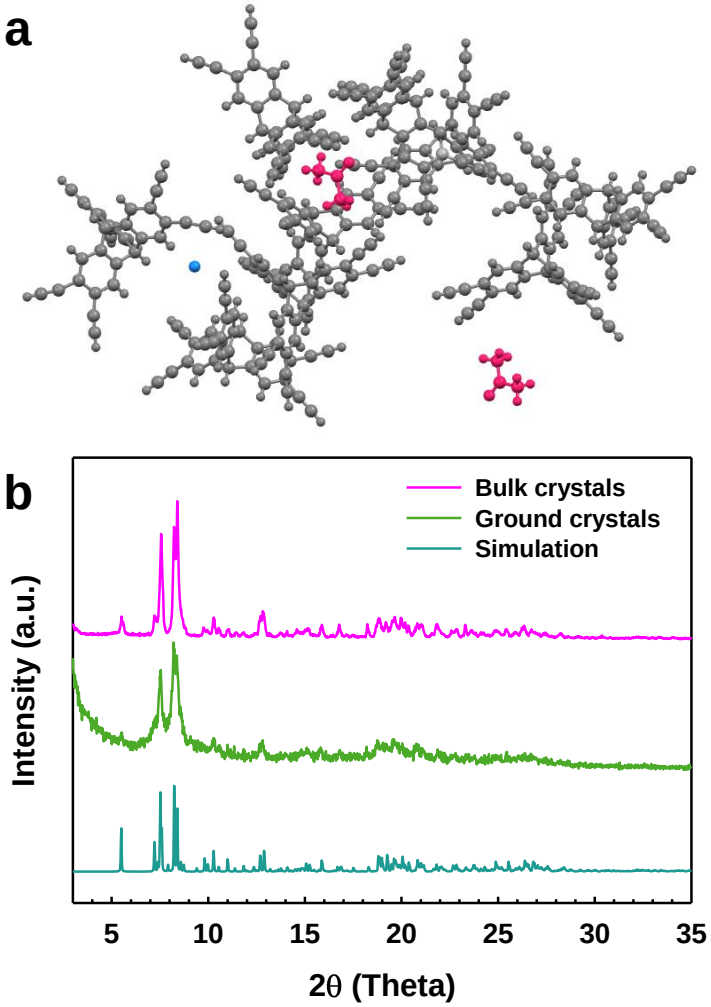

Figure 3.6. (a) Ball and Stick style diagram of crystallographic asymmetric unit of the HEA from single-crystal X-ray diffraction. (gray: HEA, red: acetone, blue: water) (d) Experimentally determined and simulated powder XRD patterns of HEA.

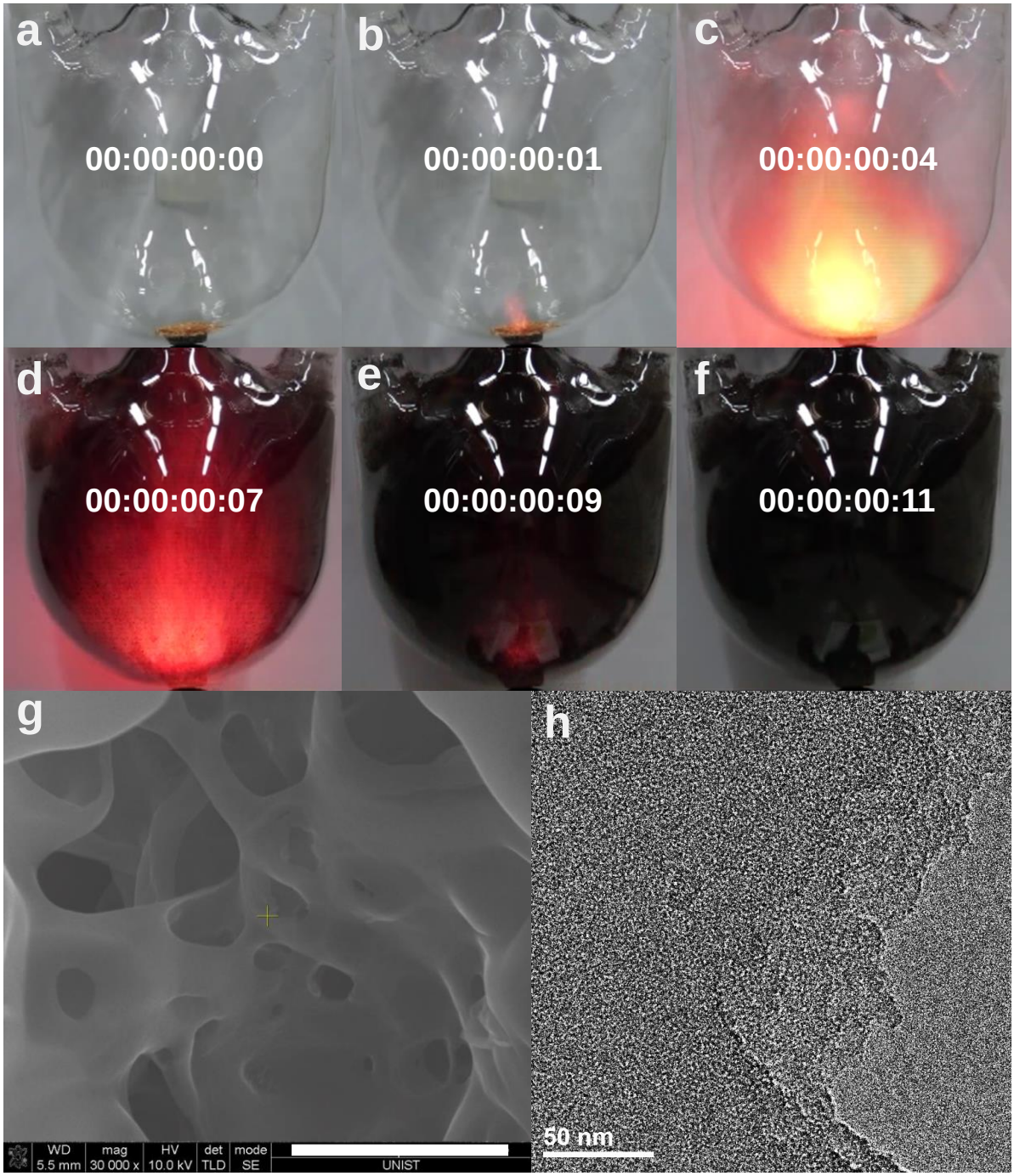

Figure 3.7. (a-f) Photographs of reaction from HEA to polyHEA at different timeframes. The images were captured by high-speed camera. (g) SEM images of polyHEA (Scale bar is 2 μm). (h) TEM image of polyHEA.

As-grown bulk HEA single crystals was utilized for thermal polymerization in solid state. As schematically presented in **Figure 3.2**, the cyclotrimerization of ethynyl groups in HEA produces three-dimensional network polymer. Generally, the reaction condition for cyclotrimerization of ethynyl groups is liquid-state solution in dried dioxane in the presence of dicobalt octacarbonyl as catalyst.[30] In this work, the explosive solid-state polymerization of HEA single crystals can be triggered by heat-treatment in the absence of solvent and catalyst. Due to dramatic volume expansion during the solid-state reaction, small amount of HEA (0.32 g) was placed in 4 L three-necked round-bottom flask. The bottom of flask, where HEA was located, was heated by heat-gun. The cyclotrimerization was instantly completed in 0.11 s (**Figure 3.7a-f**).

The unconventional reaction in solid-state was induced by lattice energy of HEA crystals. The lattice energy (see **Figure 3.3**) of HEA crystals could be speculated by comparing calorimetric heat between as-grown bulk HEA single crystals and ground HEA crystals from grinding of bulk HEA single crystals (**Figure 3.4b and 3.4c**). After thoroughly grinding of bulk HEA single crystals, the amount of acetone is reduced because some crystals in bulk HEA single crystals are splintered (see **Figure 3.8**). Although the crystallinity of ground HEA crystals is slightly decreased, ground HEA crystals also have same crystals with as-grown bulk HEA single crystal as shown in **Figure 3.6b**. Although lattice energy (ΔH_0) in both bulk and ground HEA crystals is same the kinetics of bulk and ground HEA crystals is different during heating (10 ℃ min^{-1}). The reason is that the lattice in ground HEA crystals with high surface area is more efficiently decomposed than that in bulk HEA crystals (**Figure 3.4a and 3.4d**). Consequently, in case of ground HEA crystals, the lattice is completely decomposed, the crystallinity is almost zero, at the reaction temperature. On the other hand, small part of the lattice of bulk HEA crystals is decomposed. Thus, the bulk HEA crystals has enough lattice energy (ΔH_1) for explosive solid state reaction at the moment of reaction.

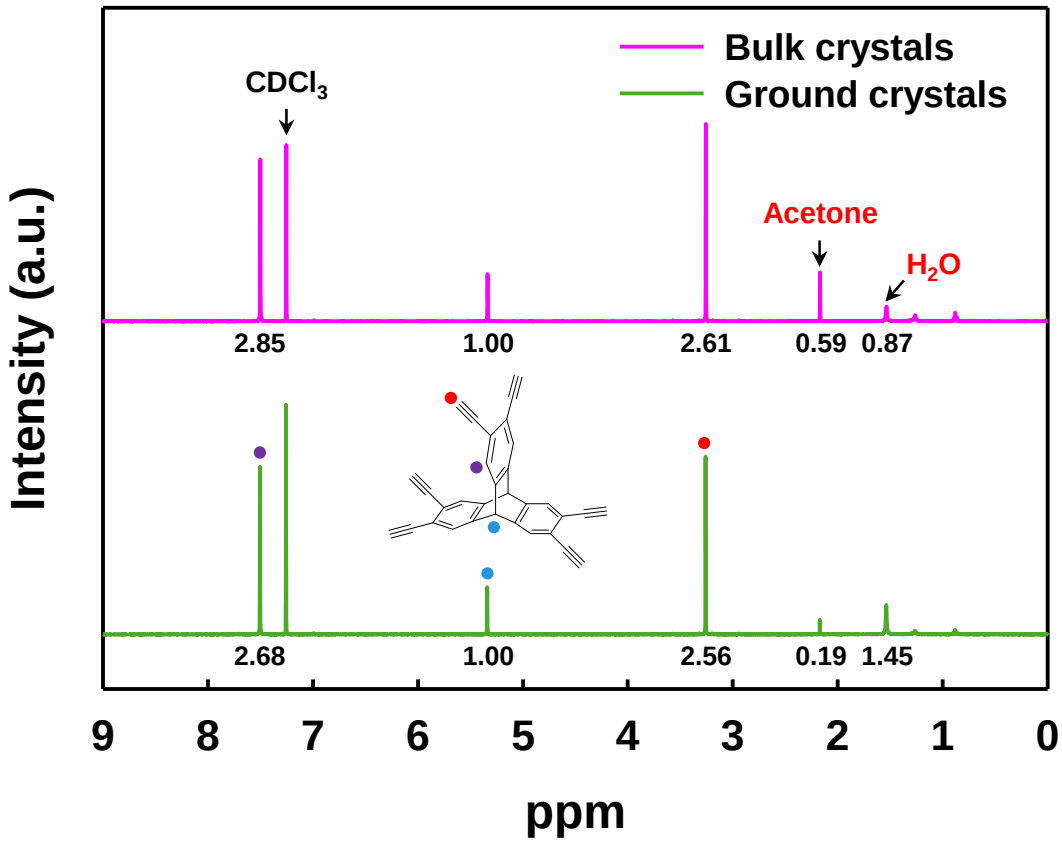

Figure 3.8. NMR spectra of as-grown bulk HEA crystal and ground HEA crystal from grinding bulk HEA crystal. After grinding, the amount of acetone is decreased but the quantity of water is increased due to large surface area of ground HEA crystal for trapping the moisture in air. 400 MHz 1H NMR of bulk HEA crystals ($CDCl_3$, δ = ppm): 1.538 (0.87, H_2O), 2.171 (0.59, Acetone), 3.260 (2.61, ≡C-H), 5.341 (1.00, CH), 7.508 (2.85, Ar-H). 400 MHz 1H NMR of ground HEA crystals ($CDCl_3$, δ = ppm): 1.537 (1.45, H_2O), 2.171 (0.19, Acetone), 3.259 (2.56, ≡C-H), 5.342 (1.00, CH), 7.508 (2.68, Ar-H).

When heat is applied to as-grown bulk HEA crystals, regularly positioned acetone and water generate kinetic energy in the HEA crystal lattice. At the same time, the lattice absorb the kinetic energy of acetone and water (ΔH_1). When the reaction temperature reached approximately 140 ℃, absorbed lattice energy from acetone and water is explosively released at the time of lattice breakage. The released energy is transferred to heat energy and kinetic energy of molecules (ΔH_2). Due to generated kinetic energy of HEA from lattice energy, HEA molecules can be rearranged for explosive cyclotrimerization of entire ethynyl groups (ΔH_3). Emitted lattice energy (ΔH_2) plays an important role to complete cyclotrimerization ($\alpha = 1$) of ethynyl groups in HEA (ΔH_3). Dramatic temperature decrease from 151 ℃ to 143 ℃ upon starting reaction (arrow, **Figure 3.4c**) occur due to the evacuation of trapped acetone and water from the HEA crystal lattice.

On the other hand, ground HEA crystals with little crystallinity at the reaction temperature cannot generate enough lattice energy to rearrange HEA molecules and thus to complete cyclotrimerization of ethynyl groups. Cyclotimerization only occurs among neighboring ethynyl groups in HEA, because ground HEA crystals has limited mobility. As a result, the color of resultant polyHEA from ground HEA crystals in oil-bath (heating rate: 1.4 ℃ s^{-1}) is orange (**Figure 3.9d**). However, in case of the ground HEA crystals upon rapid heating by heat-gun with ramping rate of 23 ℃ s^{-1}, explosive solid-state reaction occurs (**Figure 3.9c**) because ground HEA crystals with enough lattice energy to rearrange HEA molecules is suddenly reached to reaction temperature.

On the basis of these results, the released energy (ΔH_4) induced by cyclotrimerization of ethynyl groups in ground HEA crystals is much less than that (ΔH_3) in bulk HEA crystals. The tremendous difference in specific calorimetric heat changes between as-grown bulk (2588 J/g) and ground HEA crystals (1104 J/g) results from the difference of conversion ratio of ethynyl groups ($|\Delta H_3| - |\Delta H_4|$) induced by difference of lattice energy (ΔH_2) at the moment of reaction in **Figure 3.4b and 3.4c**.

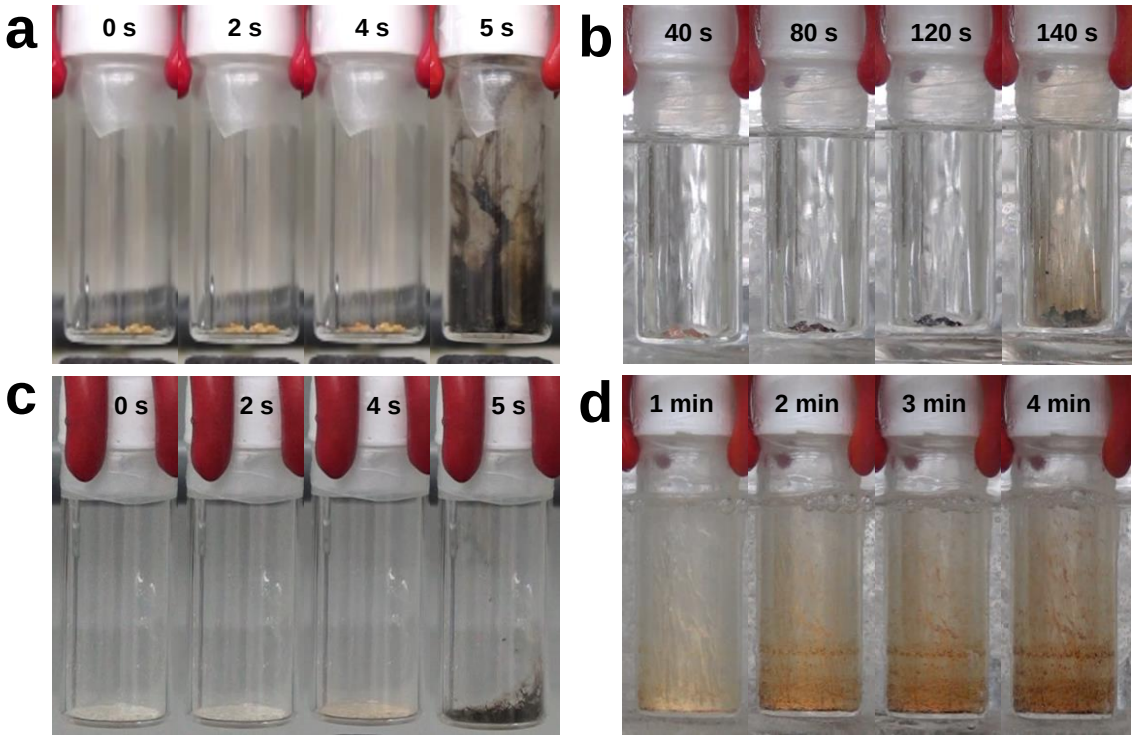

Figure 3.9. Photographs of reactions: (a) Morphology change of as-grown bulk HEA single crystals by heat-gun according to time in argon atmosphere. Heating rate of heat-gun is 23 ℃/s. (b) Morphology change of as-grown bulk HEA single crystals in oil-bath according to time in argon atmosphere. Heating rate of oil-bath is 1.4 ℃/s. (c) Morphology change of ground HEA crystals by heat-gun according to time in argon atmosphere. Heating rate of heat-gun is 23 ℃/s. (d) Morphology change of ground HEA crystals in oil-bath according to time in argon atmosphere. Heating rate of oil-bath is 1.4 ℃/s.

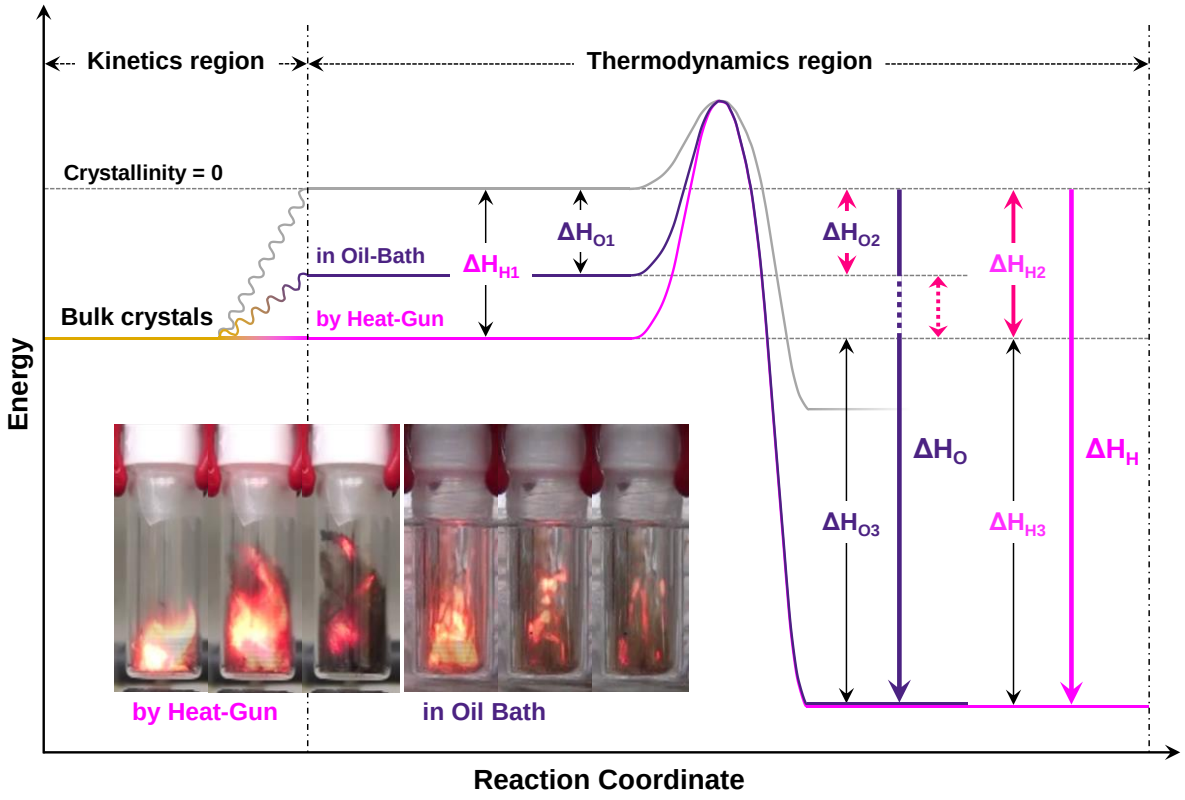

Figure 3.10. Energy diagrams of as-grown bulk HEA single crystals with different heating rate by heat-gun and in oil bath. ΔH_{H1}: Lattice energy of as-grown bulk HEA at the moment of reaction by heat gun. ΔH_{O1}: Lattice energy of as-grown bulk HEA crystals at the moment of reaction in oil bath. In oil bath for gradually heating, lattice in crystal is slowly decomposed and lattice energy reduced. ($\Delta H_{H1} > \Delta H_{O1}$) ΔH_{H2}: Absorbed lattice energy (ΔH_{H1}) is released to heat energy and kinetic energy of molecules. ΔH_{O2}: Absorbed lattice energy (ΔH_{O1}) is released to heat energy and kinetic energy of molecules. ($|\Delta H_{H2}| > |\Delta H_{O2}|$) ΔH_{H3} and ΔH_{O3}: Cyclotrimerization of entire ethynyl group in HEA occur ($\alpha = 1$, α: conversion ratio of ethynyl group in HEA, $\Delta H_{H3} = \Delta H_{O3}$). Inserts are photographs of the moment of cyclotrimerization of reaction by heat-gun and in oil bath. Crucial difference of released energy between by heat-gun (instant heating) and in oil bath (gradually heating) is lattice energy difference between ΔH_{H2} and ΔH_{O2} at the moment of trigger reaction.

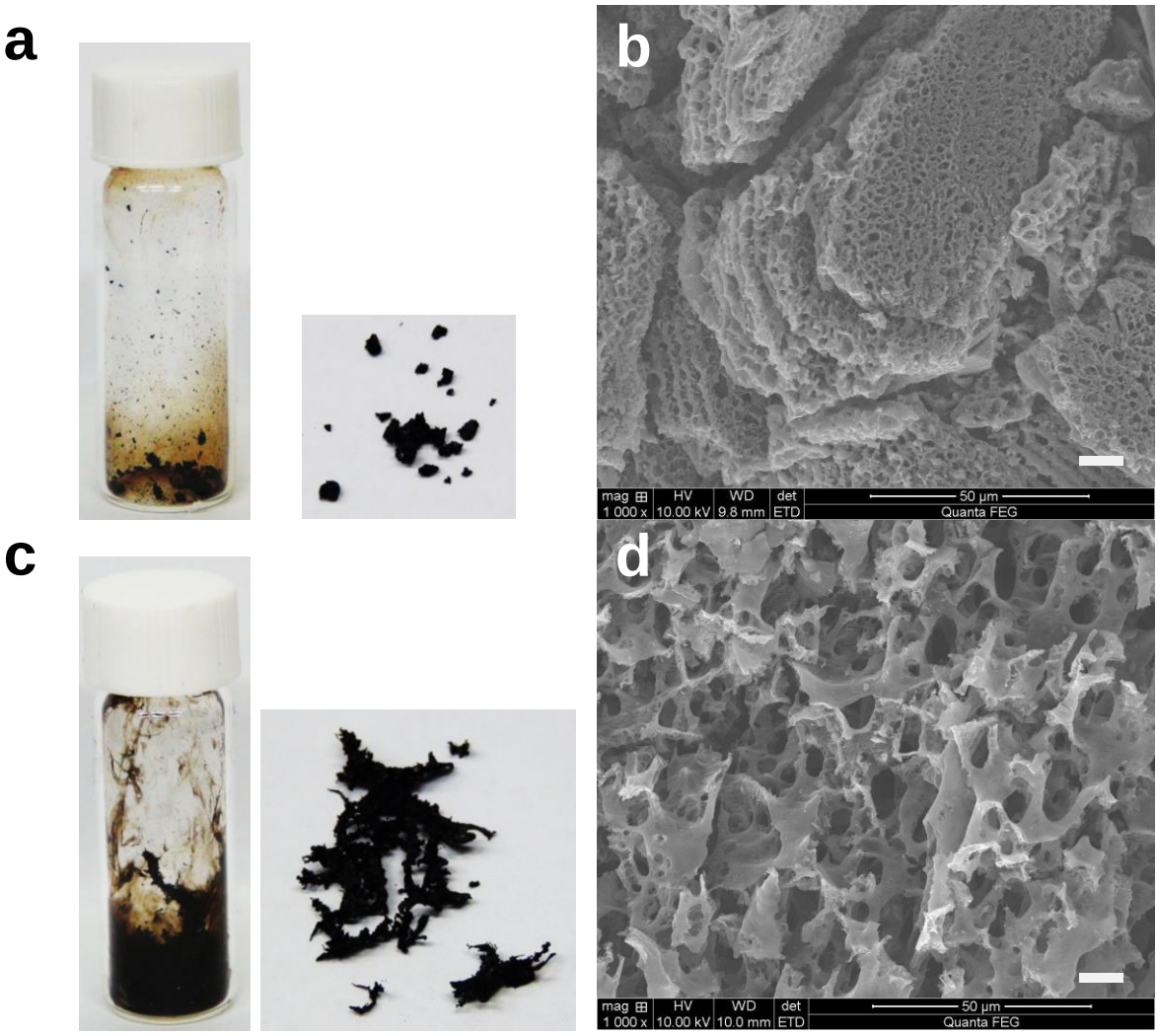

Figure 3.11. The reaction of as-grown bulk HEA single crystals under gradually elevated temperature in oil bath: (a) Photograph and (b) SEM image. The reaction of as-grown bulk HEA single crystals under suddenly elevated temperature using heat-gun. (c) Photograph and (d) SEM image. (Scale bar: 10 μm) The morphology of heating in oil-bath is smaller pore size and denser than the morphology of heating by heat-gun.

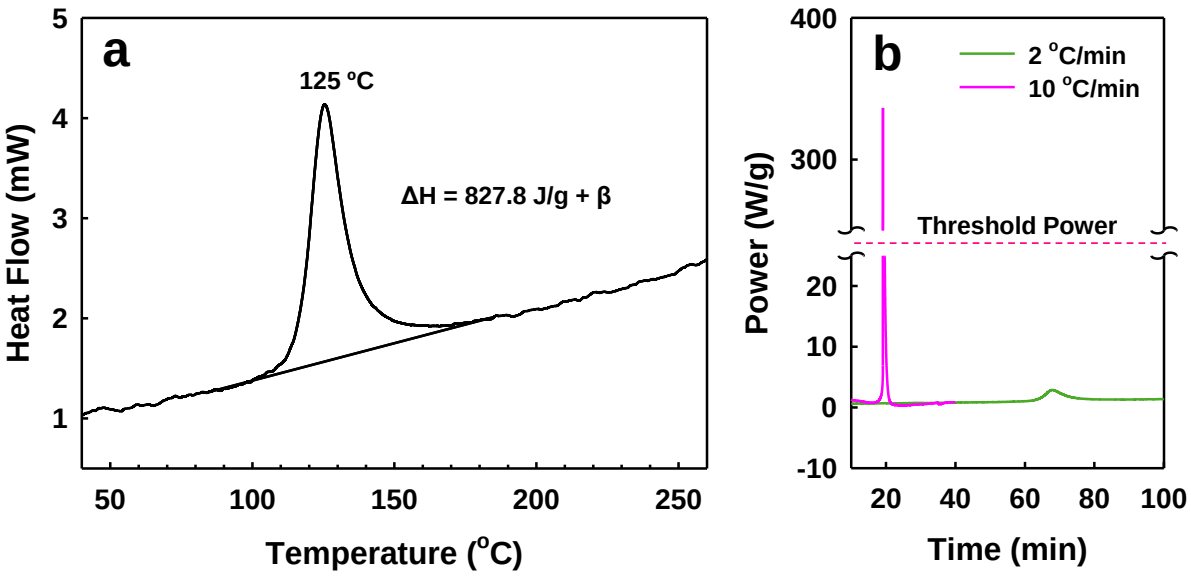

Figure 3.12. (a) DSC thermogram of 1st heating scan of as-grown bulk HEA single crystals obtained with a heating rate of 2 ℃/min. In case of a heating rate of 2 ℃/min, the reaction temperature is lower than that of 10 ℃/min about 12 ℃ because the measurement with heating rate of 2 ℃/min give enough time to absorb heat. Same phenomenon can be found in literature (10 ℃/min *vs.* 1 ℃/ min in TGA).[39] (b) DSC thermograms of as-grown bulk HEA single crystals showing amount of exothermic heat with respect to time according to different heating rate.

Further experiments was conducted to confirm the relationship between lattice energy and chemical kinetics (**Figure 3.9a and Figure 3.9b**). To have an insight of reaction kinetics related to the lattice energy changes according to heating rate, bulk HEA crystals were heated by two different types of heating sources, such as heat-gun for rapidly increasing temperature and oil bath for gradually increasing temperature. Upon rapid heating by heat-gun with ramping rate of 23 ℃ s^{-1}, the color of as-grown HEA crystals remains yellow for 4 s and suddenly explosive reaction occurred with volume expansion and color change into dark black (**Figure 3.9a**). In the case of slow heating in oil-bath with ramping rate of 1.4 ℃ s^{-1}, the color of HEA crystals was gradually changed from yellow to black while maintaining initial morphology (**Figure 3.9b**), Interestingly, exothermic heat and kinetic energy of molecules at the moment of cyclotrimerization is quite different (inserts in **Figure 3.10**). Instantly generated reaction heat upon rapid heating by heat-gun is much higher than that by gradual heating in oil-bath. Such a phenomenon could be induced by difference of lattice energy changes in bulk HEA crystals at the moment of reaction. As shown the energy diagrams in **Figure 3.10**, the lattice energy (ΔH_{O1}) of heating in oil-bath is gradually decreased according to decomposition of lattice in crystals. Consequently, released lattice energy (ΔH_{O2}) by heating in oil-bath is less than that by heating with heat-gun (ΔH_{H2}). Although released energy from cyclotrimerization of entire ethynyl groups ($\Delta H_{H3} = \Delta H_{O3}$, $\alpha = 1$) should be the same, generated heat and kinetic energy at the time of reaction is different due to the gap of lattice energy at the time of reaction. To prove this scenario, as-grown bulk HEA crystals was scanned at very slow ramping rate of 2 ℃ min^{-1}, allowing enough time for the gradual release of lattice energy in crystals. In this case, explosive solid-state cyclotrimerization not occurred, because of insufficient energy to overcome activation energy, which allows enough driving force for molecular motion of HEA molecules and cylotimerization of entire ethynyl groups (**Figure 3.12a**). On the basis of this senario, sufficient lattice energy change at given time period is necessary to overcome threshold point for evacuation of acetone and water, inducing rearrangement of HEA molecules and thus explosive cyclotrimerization of ethynyl groups in solid-state (**Figure 3.12b**).

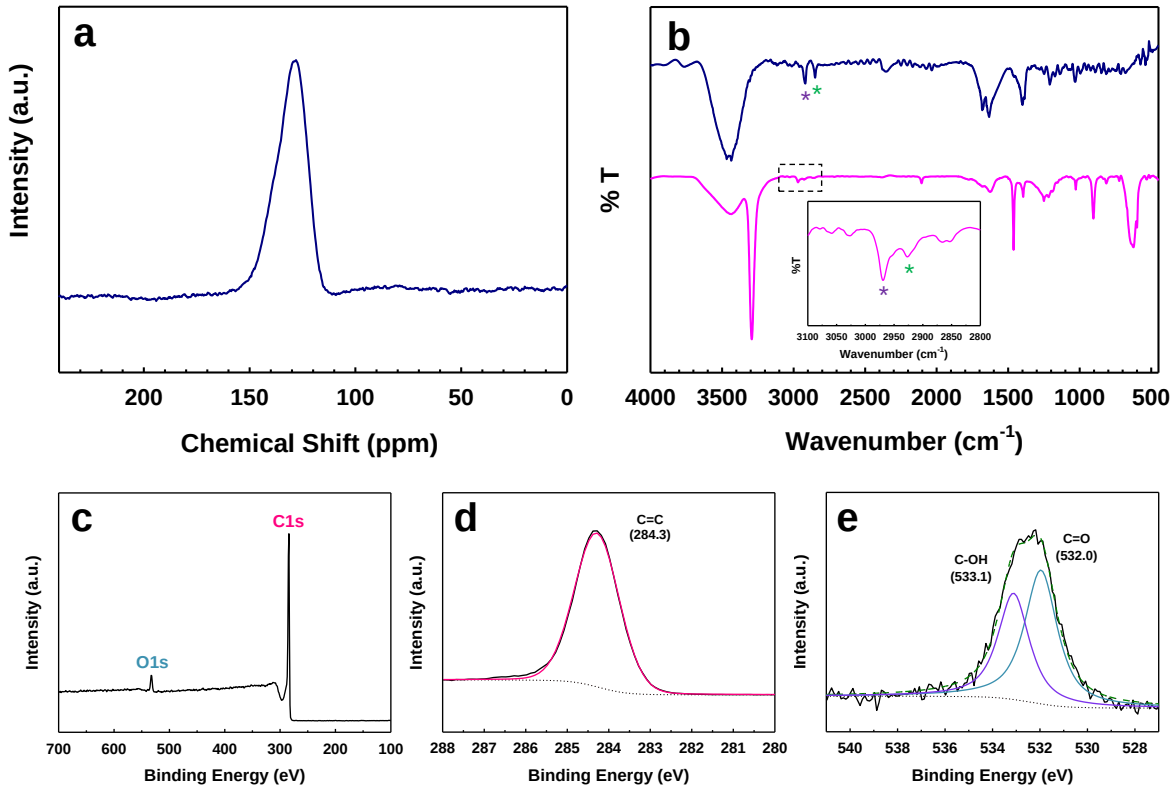

Figure 3.13. (a) Solid-state ^{13}C NMR spectrum of polyHEA. (b) FT-IR (KBr pellet) spectra of polyHEA (blue) and HEA (red). Inset is a magnification of the black dot rectangle area. XPS survey spectra of polyHEA: (c) full spectrum, (d) C1s and (e) O1s.

Table 3.2. Elemental composition of the polyHEA from different characterization techniques.

Technique	C	H	O	Total
Theoretical (wt%)	96.46	3.54	0.00	100
EA (wt%)	90.59	1.97	7.35	99.91
XPS (at%)	96.75	-	3.25	100
SEM EDS (at%)	96.61	-	3.39	100
SEM EDS (wt%)	95.53	-	4.47	100

The oxygen content of polyHEA in elemental analysis is higher than XPS and EDS from SEM about 3 wt% because the measurement of elemental analysis is accomplished by combustion analysis. As shown in **Figure 3.14**, the thermogram of polyHEA demonstrate that mass gain occur in range of about 250 ℃ to 400 ℃ in air atmosphere.

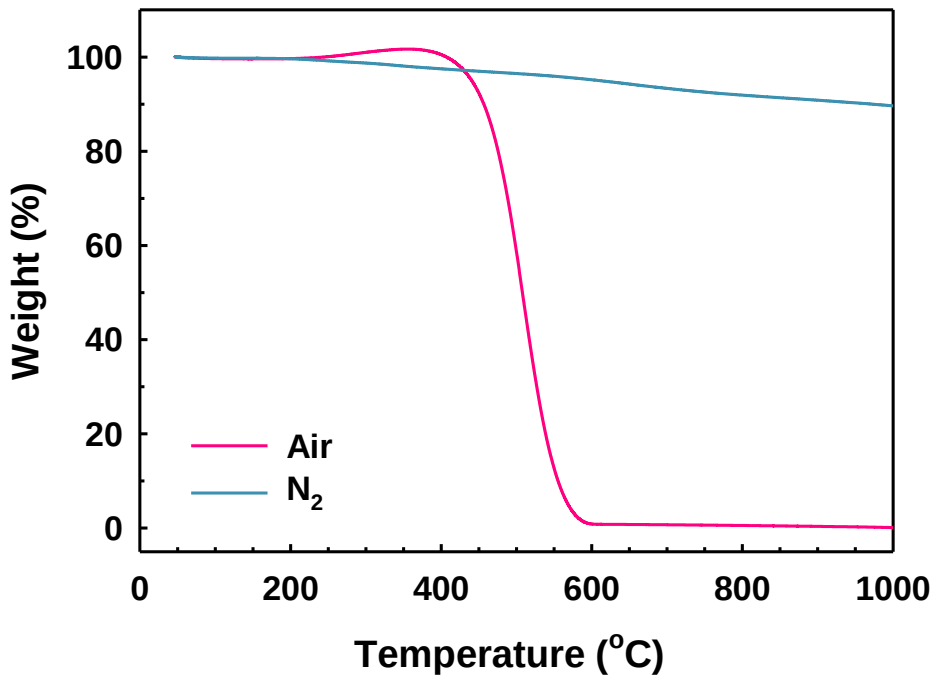

Figure 3.14. TGA thermograms of polyHEA obtained with ramping rate of 10 ℃/min in air and nitrogen.

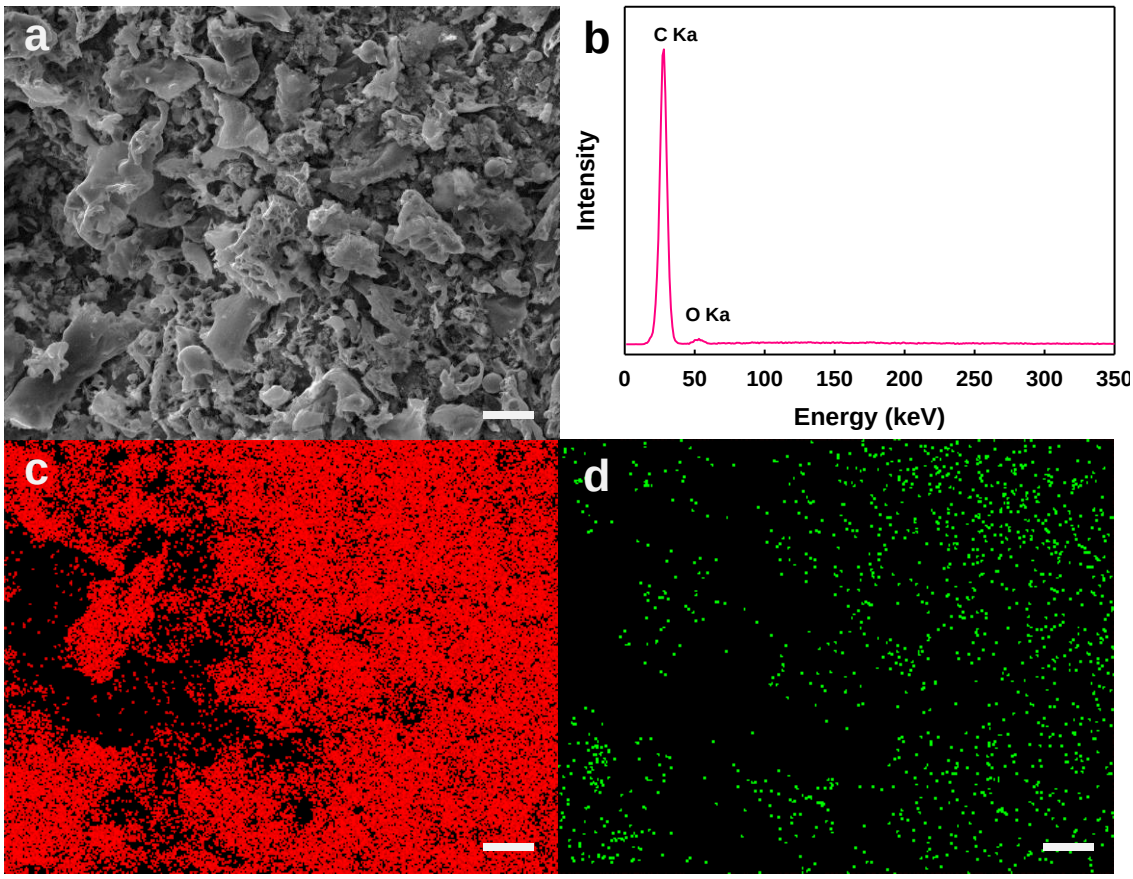

Figure 3.15. (a) SEM image of polyHEA. (b) EDAX spectrum of polyHEA. (c-d) The corresponding mapping of image (a): (c) Carbon and (d) Oxygen. (Scale bar: 20 μm)

To investigate the chemical structure of the resultant polyHEA, solid-state magic-angle carbon thirteen nuclear magnetic resonance (^{13}C NMR) was utilized. The solid ^{13}C NMR spectrum of the polyHEA in **Figure 3.13a** shows a single broad peak at 137.4 ppm, which is associated with aromatic carbon. However, aliphatic tertiary carbon was not detected by ^{13}C NMR spectrum, because the relative content of tertiary carbon in HEA exists below detected limit.

X-ray photoelectron spectroscopy (XPS) spectrum shows only C 1s and O 1s peaks (**Figure 3.13c**). High-resolution survey spectrum of C 1s indicated a single peak at 284.3 eV (C-C sp^2) (**Figure 3.13d**), which agrees well with ^{13}C NMR result. In addition, polyHEA contains high carbon content (96.75 at%) and low oxygen content (3.25 at%), whose value is well matched with energy dispersive spectroscopy (EDS) from scanning electron microscopy (SEM) (**Figure 3.15**). The O 1s peak can be deconvoluted into two peaks at 533.1 eV (C-OH) and 532.0 eV (C=O), associated mostly with physically absorbed moisture (**Figure 3.13e**).[40] Overall element composition of the polyHEA is summarized in **Table 3.2**.

The polyHEA was further characterized with Fourier transform infrared (FT-IR) spectroscopy (**Figure 3.13b**). In the case of as-grown HEA single crystals, the band at 3292 cm^{-1} can be assignable to sp C-H stretching. This peak disappeared after polymerization, suggesting that the reaction was completed without unreacted ethynyl moiety. As shown magnified spectrum in **Figure 3.13b**, the band at 2970 cm^{-1} and 2927 cm^{-1} are due to the stretching of C-H of aromatic carbon and tertiary carbon, respectively. The peaks centered at 2921 cm^{-1} and 2857 cm^{-1} after polymerization are characteristics of triptycene unit in polyHEA. The bands in the range of 1700-1600 cm^{-1} from polyHEA and those in the range of 1350-1500 cm^{-1} from starting HEA indicate sp^2 C-C in aromatic ring.

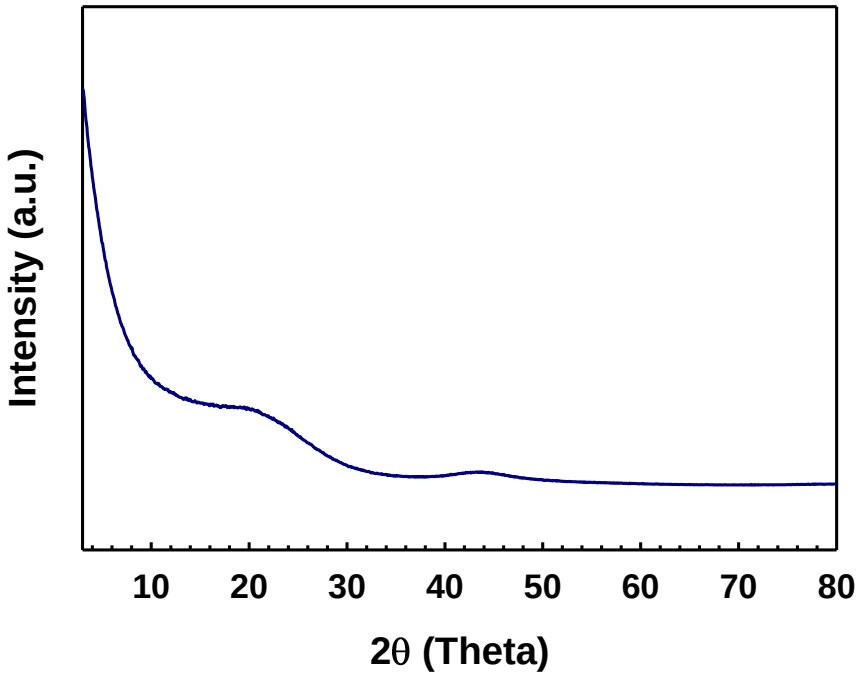

Figure 3.16. Powder X-ray diffraction pattern of polyHEA

As like most of porous network polymers are known to be amorphous solids,[41] powder XRD pattern of polyHEA is featureless, suggesting amorphous nature of polyHEA (**Figure 3.16**). Field-emission SEM (FE-SEM) and high-resolution transmission electron microscopy (HR-TEM) were utilized to investigate the morphology of polyHEA. SEM images (**Figure 3.7g**) shows the formation of fishing net-type morphology, which is different from the previously reported porous network polymers,[42-44] which are prepared from liquid-state solution polymerization and thus having spherical morphology. HR-TEM images show quite uniform dark and bright spots in the polyHEA matrice (**Figure 3.7h**), suggesting porous nature of polyHEA.

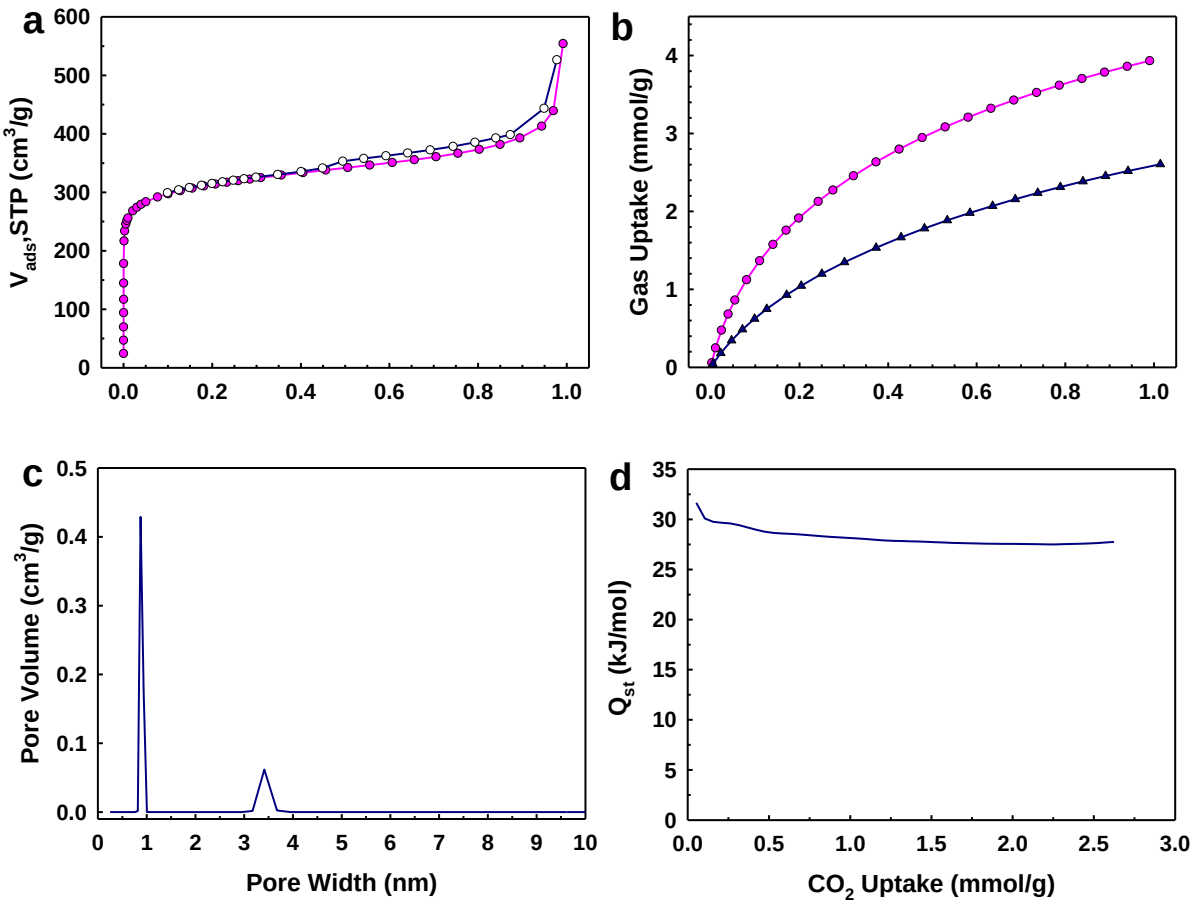

Figure 3.17. (a) Nitrogen adsorption (solid) and desorption (open) isotherms of polyHEA at 77 K. (b) CO_2 adsorption isotherms of polyHEA at 273 K (pink-circle) and 298 K (dark blue-triangle). (c) Pore-size distribution of polyHEA calculated by GCMC method. (d) Isosteric heats of adsorption of polyHEA, as calculated from the adsorption curves at 273 K and 298 K.

Nitrogen gas adsorption/desorption isotherms was collected at 77 K (**Figure 3.17a**). The specific Brunauer-Emmet-Teller surface area (S_{BET}) and total pore volume are 1176 m^2/g and 0.843 cm^3/g. polyHEA exhibited a type-1 isotherm, indicating its microporous (pore size < 2 nm) nature.[45] The apparent hysteresis around 0.45 P/P_0 between adsorption and desorption is observed, which is mesoporous (pore size 2-50 nm) materials, and may be attributed to the pore network effects.[46] **Figure 3.17c** show the pore size distribution (PSD) for polyHEA as calculated using Grand Canonical Monte Carlo method (GCMC). Two major pore widths of polyHEA is 0.89 nm and 3.43 nm.

We first collected CO_2 isotherms and calculated their isosteric heats of adsorption (Q_{st}) using the Clausius Clapeyron equation, as shown in **Figure 3.17b** and **3.17d**. polyHEA exhibits CO_2 uptake of 3.93 mmol/g at 273 K and 2.61 mmol/g at 298 K (1 bar). The Q_{st} of polyHEA for CO_2 was found to be 31.7 kJ/mol at zero coverage. CO_2 uptake is higher than porous polymers having very high surface area, such as PAF-1[47] (S_{BET}: 5460 m^2/g, 2.09 mmol/g at 273 K and 1 bar), Network-A[48] (S_{BET}: 4077 m^2/g, 2.65 mmol/g at 273 K and 1 bar), Network-1[49] (S_{BET}: 1980 m^2/g, 3.63 mmol/g at 273 K and 1 bar) and BPL carbon[48] (S_{BET}: 1150 m^2/g, 2.09 mmol/g at 273 K and 1 bar; a common reference material for CO_2 uptake). For determining the CO_2 capture capacities, surface property and tuned pore geometry of porous materials is more important than large surface area.[50]

In principle, the porous organic polymers with nitrogen-rich functionalities, such as triazine, tetrazole, imidazole, carbazole, phosphazene, imide, amine and azo compound exhibit high CO_2 adsorption capacities because of the strong electrostatic interactions between CO_2 and nitrogen sites.[44] However, CO_2 uptake and Q_{st} value of polyHEA without nitrogen are comparable to nitrogen contained porous organic polymer, such as SNW-1[51] (3.64 mmol/g at 273 K and 1 bar, Q_{st}: 35.0 kJ/mol), PECONF-3[42] (3.49 mmol/g at 273 K and 1 bar, Q_{st}: 26.0 kJ/mol), NPTN-2[52] (3.18 mmol/g at 273 K and 1 bar, Q_{st}: 37.0 kJ/mol) and azo-COP-2 (2.55 mmol/g at 273 K and 1 bar, Q_{st}: 24.8 kJ/mol) because electron rich cavity of polyHEA interact with the carbon atom of the CO_2 molecule. The porous properties of the polymers with and without nitrogen are summarized in **Table 3.3**.

Table 3.3. Summary of surface area, CO_2 uptake (at 273 K, 1 bar) and isosteric heat (Q_{st}) of various porous materials.

Porous materials	Nitrogen (wt %)	S_{BET} (m^2/g)	CO_2 uptake (mmol/g)	Q_{st} (kJ/mol)	Ref.
polyHEA	–	1176	3.93	31.7	This work
Network-1	–	1980	3.63	23.3	[49]
Network-E	–	1470	2.95	25.5	[48]
Network-A	–	4077	2.65	23.0	[48]
Network-D	–	1213	2.42	26.0	[48]
BPL carbon	–	1150	2.09	–	[48]
PAF-1	–	5460	2.07	15.6	[47]
CMP-1	–	837	2.05	27.2	[53]
FCTF-1-600	15.4[a]	1535	5.53	35.0	[54]
BILP-4	14.0	1135	5.41	28.7	[55]
ALP-1	12.5	1235	5.36	29.2	[56]
BILP-3	9.96	1306	5.11	28.6	[57]
CPOP-1	7.32[b]	2220	4.82	27.0	[58]
Cz-POF-3	5.97	1927	4.77	27.8	[59]
APOP-3	29.5	1402	4.54	27.5	[60]
BILP-7	10.9	1122	4.39	27.8	[55]
TSP-2	7.92	913	4.1	30.2	[61]
Network-C	14.6	1237	3.86	33.0	[48]
SNW-1	29.9	821	3.64	35.0	[51]
PECONF-3	24.0[b]	851	3.49	26.0	[42]
STPI-2	7.12	541	3.34	36.0	[62]
TPI-1@IC	7.09	1053	3.22	49.3	[63]
NPTN-2	10.6	1558	3.18	37.0	[52]
NPTN-1	15.3	1187	3.01	34.0	[52]
Py-1	10.9	437	2.7	36.0	[44]
azo-COP-2	14.4	702.6	2.55	24.8	[64]
azo-COP-1	14.2	608.1	2.44	29.3	[64]
NPTN-3	8.24	1055	2.22	30.0	[52]

[a]XPS measured result (at %), [b] Caculated result of structure

3.8 Conclusion

In this work, we have successfully synthesized HEA from triptycene and have obtained single crystal compound (HEA crystals) by slow evaporation. The structure HEA crystals was characterized by single-crystal XRD analysis. The polymerization of HEA crystals were realized in less than a second at low temperature (~140 ℃) in the absence of any solvent and catalyst. The principle of explosive reaction thermally induced from trapped small molecule in crystal was demonstrated through DSC results. PolyHEA with high surface areas (S_{BET}: 1176 m^2/g) was obtained from the solid-state reaction. The carbon dioxide (CO_2) sorption capacity of the polyHEA is reached up to 3.93 mmol/g at 273K (1 bar) and 2.61 mmol/g at 298 K (1 bar). The Q_{st} of CO_2 is found to be 31.7 kJ/mol at zero coverage. This new strategy of polymer synthesis will give a new dimension to solid-state reaction investigations.

3.9 References

1. Tanaka, K.; Toda, F. Solvent-Free Organic Synthesis. *Chemical Reviews* **2000,** *100* (3), 1025-1074.

2. Anastas, P. T.; Warner, J. C. *Green Chemistry: Theory and Practice*. Oxford University Press: New York, 1998.

3. Tanaka, K. *Solvent-free Organic Synthesis*. Wiley-VCH: Weinheim, 2003.

4. Baughman, R. H. Solid-state reaction kinetics in single-phase polymerizations. *The Journal of Chemical Physics* **1978,** *68* (7), 3110-3121.

5. James, S. L.; Adams, C. J.; Bolm, C.; Braga, D.; Collier, P.; Friscic, T.; Grepioni, F.; Harris, K. D. M.; Hyett, G.; Jones, W.; Krebs, A.; Mack, J.; Maini, L.; Orpen, A. G.; Parkin, I. P.; Shearouse, W. C.; Steed, J. W.; Waddell, D. C. Mechanochemistry: opportunities for new and cleaner synthesis. *Chemical Society Reviews* **2012,** *41* (1), 413-447.

6. He, D.; Susanto, H.; Ulbricht, M. Photo-irradiation for preparation, modification and stimulation of polymeric membranes. *Progress in Polymer Science* **2009,** *34* (1), 62-98.

7. Jeon, I.-Y.; Bae, S.-Y.; Seo, J.-M.; Baek, J.-B. Scalable Production of Edge-Functionalized Graphene Nanoplatelets via Mechanochemical Ball-Milling. *Advanced Functional Materials* **2015**, n/a-n/a.

8. Braga, D.; Grepioni, F. Reactions Between or Within Molecular Crystals. *Angewandte Chemie International Edition* **2004,** *43* (31), 4002-4011.

9. Braga, D.; Giaffreda, S. L.; Grepioni, F.; Pettersen, A.; Maini, L.; Curzi, M.; Polito, M. Mechanochemical preparation of molecular and supramolecular organometallic materials and coordination networks. *Dalton Transactions* **2006,** (10), 1249-1263.

10. Kuroda, R.; Yoshida, J.; Nakamura, A.; Nishikiori, S.-i. Annealing assisted mechanochemical syntheses of transition-metal coordination compounds and co-crystal formation. *CrystEngComm* **2009,** *11* (3), 427-432.

11. Bhola, R.; Payamyar, P.; Murray, D. J.; Kumar, B.; Teator, A. J.; Schmidt, M. U.; Hammer, S. M.; Saha, A.; Sakamoto, J.; Schlüter, A. D.; King, B. T. A Two-Dimensional Polymer from the Anthracene Dimer and Triptycene Motifs. *Journal of the American Chemical Society* **2013,** *135* (38), 14134-14141.

12. Kissel, P.; Murray, D. J.; Wulftange, W. J.; Catalano, V. J.; King, B. T. A nanoporous two-dimensional polymer by single-crystal-to-single-crystal photopolymerization. *Nat Chem* **2014,** *6* (9), 774-778.

13. Kissel, P.; Erni, R.; Schweizer, W. B.; Rossell, M. D.; King, B. T.; Bauer, T.; Götzinger, S.; Schlüter, A. D.; Sakamoto, J. A two-dimensional polymer prepared by organic synthesis. *Nat Chem* **2012,** *4* (4), 287-291.

14. Jiang, J.-X.; Su, F.; Niu, H.; Wood, C. D.; Campbell, N. L.; Khimyak, Y. Z.; Cooper, A. I. Conjugated microporous poly(phenylene butadiynylene)s. *Chemical Communications* **2008,** (4), 486-488.

15. Li, A.; Lu, R.-F.; Wang, Y.; Wang, X.; Han, K.-L.; Deng, W.-Q. Lithium-Doped Conjugated Microporous Polymers for Reversible Hydrogen Storage. *Angewandte Chemie International Edition* **2010,** *49* (19), 3330-3333.

16. Jiang, J.-X.; Trewin, A.; Su, F.; Wood, C. D.; Niu, H.; Jones, J. T. A.; Khimyak, Y. Z.; Cooper, A. I. Microporous Poly(tri(4-ethynylphenyl)amine) Networks: Synthesis, Properties, and Atomistic Simulation. *Macromolecules* **2009,** *42* (7), 2658-2666.

17. Dawson, R.; Laybourn, A.; Khimyak, Y. Z.; Adams, D. J.; Cooper, A. I. High Surface Area Conjugated Microporous Polymers: The Importance of Reaction Solvent Choice. *Macromolecules* **2010,** *43* (20), 8524-8530.

18. Chen, L.; Honsho, Y.; Seki, S.; Jiang, D. Light-Harvesting Conjugated Microporous Polymers: Rapid and Highly Efficient Flow of Light Energy with a Porous Polyphenylene Framework as Antenna. *Journal of the American Chemical Society* **2010,** *132* (19), 6742-6748.

19. Schmidt, J.; Werner, M.; Thomas, A. Conjugated Microporous Polymer Networks via Yamamoto Polymerization. *Macromolecules* **2009,** *42* (13), 4426-4429.

20. Xu, Y.; Chen, L.; Guo, Z.; Nagai, A.; Jiang, D. Light-Emitting Conjugated Polymers with Microporous Network Architecture: Interweaving Scaffold Promotes Electronic Conjugation, Facilitates Exciton Migration, and Improves Luminescence. *Journal of the American Chemical Society* **2011,** *133* (44), 17622-17625.

21. Wood, C. D.; Tan, B.; Trewin, A.; Su, F.; Rosseinsky, M. J.; Bradshaw, D.; Sun, Y.; Zhou, L.; Cooper, A. I. Microporous Organic Polymers for Methane Storage. *Advanced Materials* **2008,** *20* (10), 1916-1921.

22. Li, B.; Huang, X.; Liang, L.; Tan, B. Synthesis of uniform microporous polymer nanoparticles and their applications for hydrogen storage. *Journal of Materials Chemistry* **2010,** *20* (35), 7444-7450.

23. Holst, J. R.; Stöckel, E.; Adams, D. J.; Cooper, A. I. High Surface Area Networks from Tetrahedral Monomers: Metal-Catalyzed Coupling, Thermal Polymerization, and "Click" Chemistry. *Macromolecules* **2010,** *43* (20), 8531-8538.

24. Dawson, R.; Su, F.; Niu, H.; Wood, C. D.; Jones, J. T. A.; Khimyak, Y. Z.; Cooper, A. I. Mesoporous Poly(phenylenevinylene) Networks. *Macromolecules* **2008,** *41* (5), 1591-1593.

25. Rabbani, M. G.; El-Kaderi, H. M. Template-Free Synthesis of a Highly Porous Benzimidazole-Linked Polymer for CO2 Capture and H2 Storage. *Chemistry of Materials* **2011,** *23* (7), 1650-1653.

26. Schwab, M. G.; Fassbender, B.; Spiess, H. W.; Thomas, A.; Feng, X.; Müllen, K. Catalyst-free Preparation of Melamine-Based Microporous Polymer Networks through Schiff Base Chemistry. *Journal of the American Chemical Society* **2009,** *131* (21), 7216-7217.

27. Weber, J.; Antonietti, M.; Thomas, A. Microporous Networks of High-Performance Polymers: Elastic Deformations and Gas Sorption Properties. *Macromolecules* **2008,** *41* (8), 2880-2885.

28. Farha, O. K.; Spokoyny, A. M.; Hauser, B. G.; Bae, Y.-S.; Brown, S. E.; Snurr, R. Q.; Mirkin, C. A.; Hupp, J. T. Synthesis, Properties, and Gas Separation Studies of a Robust Diimide-Based Microporous Organic Polymer. *Chemistry of Materials* **2009,** *21* (14), 3033-3035.

29. Yuan, S.; Kirklin, S.; Dorney, B.; Liu, D.-J.; Yu, L. Nanoporous Polymers Containing Stereocontorted Cores for Hydrogen Storage. *Macromolecules* **2009,** *42* (5), 1554-1559.

30. Yuan, S.; Dorney, B.; White, D.; Kirklin, S.; Zapol, P.; Yu, L.; Liu, D.-J. Microporous polyphenylenes with tunable pore size for hydrogen storage. *Chemical Communications* **2010,** *46* (25), 4547-4549.

31. Ren, H.; Ben, T.; Wang, E.; Jing, X.; Xue, M.; Liu, B.; Cui, Y.; Qiu, S.; Zhu, G. Targeted synthesis of a 3D porous aromatic framework for selective sorption of benzene. *Chemical Communications* **2010,** *46* (2), 291-293.

32. Rose, M.; Klein, N.; Senkovska, I.; Schrage, C.; Wollmann, P.; Bohlmann, W.; Bohringer, B.; Fichtner, S.; Kaskel, S. A new route to porous monolithic organic frameworks via cyclotrimerization. *Journal of Materials Chemistry* **2011,** *21* (3), 711-716.

33. Xiang, S.; He, Y.; Zhang, Z.; Wu, H.; Zhou, W.; Krishna, R.; Chen, B. Microporous metal-organic framework with potential for carbon dioxide capture at ambient conditions. *Nat Commun* **2012,** *3*, 954.

34. Côté, A. P.; Benin, A. I.; Ockwig, N. W.; O'Keeffe, M.; Matzger, A. J.; Yaghi, O. M. Porous, Crystalline, Covalent Organic Frameworks. *Science* **2005,** *310* (5751), 1166-1170.

35. Hilton, C. L.; Jamison, C. R.; Zane, H. K.; King, B. T. A Triphenylene-Based Triptycene with Large Free Volume Synthesized by Zirconium-Mediated Biphenylation. *The Journal of Organic Chemistry* **2009,** *74* (1), 405-407.

36. Johnson, D. A.; Clark, G. *Metals and Chemical Change (Molecular World)* Royal Society of Chemistry: 2002.

37. Sheldrick, G. Crystal structure refinement with SHELXL. *Acta Crystallographica Section C* **2015,** *71* (1), 3-8.

38. Zhao, L.; Li, Z.; Wirth, T. Triptycene Derivatives: Synthesis and Applications. *Chemistry Letters* **2010,** *39* (7), 658-667.

39. Bae, S.-Y.; Jeon, I.-Y.; Yang, J.; Park, N.; Shin, H. S.; Park, S.; Ruoff, R. S.; Dai, L.; Baek, J.-B. Large-Area Graphene Films by Simple Solution Casting of Edge-Selectively Functionalized Graphite. *ACS Nano* **2011,** *5* (6), 4974-4980.

40. Jeon, I.-Y.; Shin, Y.-R.; Sohn, G.-J.; Choi, H.-J.; Bae, S.-Y.; Mahmood, J.; Jung, S.-M.; Seo, J.-M.; Kim, M.-J.; Wook Chang, D.; Dai, L.; Baek, J.-B. Edge-carboxylated graphene nanosheets via ball milling. *Proceedings of the National Academy of Sciences* **2012,** *109* (15), 5588-5593.

41. McKeown, N. B.; Budd, P. M. Polymers of intrinsic microporosity (PIMs): organic materials for membrane separations, heterogeneous catalysis and hydrogen storage. *Chemical Society Reviews* **2006,** *35* (8), 675-683.

42. Mohanty, P.; Kull, L. D.; Landskron, K. Porous covalent electron-rich organonitridic frameworks as highly selective sorbents for methane and carbon dioxide. *Nat Commun* **2011,** *2*, 401.

43. Zhang, C.; Liu, Y.; Li, B.; Tan, B.; Chen, C.-F.; Xu, H.-B.; Yang, X.-L. Triptycene-Based Microporous Polymers: Synthesis and Their Gas Storage Properties. *ACS Macro Letters* **2012,** *1* (1), 190-193.

44. Luo, Y.; Li, B.; Wang, W.; Wu, K.; Tan, B. Hypercrosslinked Aromatic Heterocyclic Microporous Polymers: A New Class of Highly Selective CO2 Capturing Materials. *Advanced Materials* **2012,** *24* (42), 5703-5707.

45. Sing, K. S. W.; Everett, D. H.; Haul, R. A. W.; Moscou, L.; Pierotti, R. A.; Rouquerol, J.; Siemieniewska, T. Reporting physisorption data for gas/solid systems with special reference to the determination of surface area and porosity. *Pure and Applied Chemistry* **1985,** *57* (4), 603-619.

46. Budd, P. M.; Elabas, E. S.; Ghanem, B. S.; Makhseed, S.; McKeown, N. B.; Msayib, K. J.; Tattershall, C. E.; Wang, D. Solution-Processed, Organophilic Membrane Derived from a Polymer of Intrinsic Microporosity. *Advanced Materials* **2004,** *16* (5), 456-459.

47. Ben, T.; Pei, C.; Zhang, D.; Xu, J.; Deng, F.; Jing, X.; Qiu, S. Gas storage in porous aromatic frameworks (PAFs). *Energy & Environmental Science* **2011,** *4* (10), 3991-3999.

48. Dawson, R.; Stockel, E.; Holst, J. R.; Adams, D. J.; Cooper, A. I. Microporous organic polymers for carbon dioxide capture. *Energy & Environmental Science* **2011,** *4* (10), 4239-4245.

49. Yao, S.; Yang, X.; Yu, M.; Zhang, Y.; Jiang, J.-X. High surface area hypercrosslinked microporous organic polymer networks based on tetraphenylethylene for CO2 capture. *Journal of Materials Chemistry A* **2014,** *2* (21), 8054-8059.

50. Simmons, J. M.; Wu, H.; Zhou, W.; Yildirim, T. Carbon capture in metal-organic frameworks-a comparative study. *Energy & Environmental Science* **2011,** *4* (6), 2177-2185.

51. Gao, X.; Zou, X.; Ma, H.; Meng, S.; Zhu, G. Highly Selective and Permeable Porous Organic Framework Membrane for CO2 Capture. *Advanced Materials* **2014,** *26* (22), 3644-3648.

52. Wu, S.; Liu, Y.; Yu, G.; Guan, J.; Pan, C.; Du, Y.; Xiong, X.; Wang, Z. Facile Preparation of Dibenzoheterocycle-Functional Nanoporous Polymeric Networks with High Gas Uptake Capacities. *Macromolecules* **2014,** *47* (9), 2875-2882.

53. Dawson, R.; Adams, D. J.; Cooper, A. I. Chemical tuning of CO2 sorption in robust nanoporous organic polymers. *Chemical Science* **2011,** *2* (6), 1173-1177.

54. Zhao, Y.; Yao, K. X.; Teng, B.; Zhang, T.; Han, Y. A perfluorinated covalent triazine-based framework for highly selective and water-tolerant CO2 capture. *Energy & Environmental Science* **2013,** *6* (12), 3684-3692.

55. Rabbani, M. G.; El-Kaderi, H. M. Synthesis and Characterization of Porous Benzimidazole-Linked Polymers and Their Performance in Small Gas Storage and Selective Uptake. *Chemistry of Materials* **2012,** *24* (8), 1511-1517.

56. Arab, P.; Rabbani, M. G.; Sekizkardes, A. K.; İslamoğlu, T.; El-Kaderi, H. M. Copper(I)-Catalyzed Synthesis of Nanoporous Azo-Linked Polymers: Impact of Textural Properties on Gas Storage and Selective Carbon Dioxide Capture. *Chemistry of Materials* **2014,** *26* (3), 1385-1392.

57. Rabbani, M. G.; Reich, T. E.; Kassab, R. M.; Jackson, K. T.; El-Kaderi, H. M. High CO2 uptake and selectivity by triptycene-derived benzimidazole-linked polymers. *Chemical Communications* **2012,** *48* (8), 1141-1143.

58. Chen, Q.; Luo, M.; Hammershøj, P.; Zhou, D.; Han, Y.; Laursen, B. W.; Yan, C.-G.; Han, B.-H. Microporous Polycarbazole with High Specific Surface Area for Gas Storage and Separation. *Journal of the American Chemical Society* **2012,** *134* (14), 6084-6087.

59. Zhang, X.; Lu, J.; Zhang, J. Porosity Enhancement of Carbazolic Porous Organic Frameworks Using Dendritic Building Blocks for Gas Storage and Separation. *Chemistry of Materials* **2014,** *26* (13), 4023-4029.

60. Song, W.-C.; Xu, X.-K.; Chen, Q.; Zhuang, Z.-Z.; Bu, X.-H. Nitrogen-rich diaminotriazine-based porous organic polymers for small gas storage and selective uptake. *Polymer Chemistry* **2013,** *4* (17), 4690-4696.

61. Zhu, X.; Mahurin, S. M.; An, S.-H.; Do-Thanh, C.-L.; Tian, C.; Li, Y.; Gill, L. W.; Hagaman, E. W.; Bian, Z.; Zhou, J.-H.; Hu, J.; Liu, H.; Dai, S. Efficient CO2 capture by a task-specific porous organic polymer bifunctionalized with carbazole and triazine groups. *Chemical Communications* **2014,** *50* (59), 7933-7936.

62**.** Zhang, C.; Zhai, T.-L.; Wang, J.-J.; Wang, Z.; Liu, J.-M.; Tan, B.; Yang, X.-L.; Xu, H.-B. Triptycene-based microporous polyimides: Synthesis and their high selectivity for CO2 capture. *Polymer* **2014,** *55* (16), 3642-3647.

63**.** Wu, S.; Gu, S.; Zhang, A.; Yu, G.; Wang, Z.; Jian, J.; Pan, C. A rational construction of microporous imide-bridged covalent-organic polytriazines for high-enthalpy small gas absorption. *Journal of Materials Chemistry A* **2015,** *3* (2), 878-885.

64**.** Patel, H. A.; Hyun Je, S.; Park, J.; Chen, D. P.; Jung, Y.; Yavuz, C. T.; Coskun, A. Unprecedented high-temperature CO2 selectivity in N2-phobic nanoporous covalent organic polymers. *Nat Commun* **2013,** *4*, 1357.

Acknowledgement

학문의 길이 무엇인지도 모르고 시작한 석사과정을 시작으로, 길고 긴 석·박사 통합과정은 연구에 대한 많은 학문적인 갈등과 고뇌와 스스로에 대한 많은 생각을 할 수 있는 자아성찰의 시간이였습니다. 그 긴 과정은 저에게 한없이 달콤하기만 한 과정은 아니였지만 돌이켜 생각해보면 그 과정이 있었기에 지금의 '배서윤'이라는 사람이 있지 않을까 생각됩니다.

많은 사람들의 도움으로 힘들었던 과정을 무사히 마치고 졸업을 할 수 있게 된 지금, 이 자리를 빌어 감사의 말을 전합니다. 먼저, 부족한 저에게 많은 조언과 지도를 아끼지 않고, 연구에 대한 열정을 보여주신 백종범 교수님 감사합니다. 그리고 먼 거리를 오가며 많은 조언과 응원을 해 주신 장동욱 교수님 감사합니다. 학문적인 많은 조언을 해주신 나명수 교수님, 문회리 교수님, 정후영 교수님 감사합니다. 좋은 결과가 나올 수 있도록 도와주신 UCRF 선생님들께도 감사를 전합니다. 외로울 수 있는 실험 과정 중에 함께 동거동락한 인엽이 오빠, 현정이 언니, Javeed 오빠, 선민이, 정민이, 석진이, 윤광이, 선희, 수영이, 혁준이, 도형이, 지금은 졸업한 종렬이, 경주, 연란이, 경수오빠, 지예언니, 종관이 오빠, 상욱이 오빠가 있었기에 그 시간이 행복했습니다. 이 자리를 빌어서 감사를 전합니다. 10 년동안 함께 살고 옆에서 많은 힘이 되어준 명희, 늘 초긍정 에너지를 보여주는 효정이, 울산에서 만난 UMGs 영심이 언니, 미희언니, 정일이 언니, 제이슨 오빠, 희진이가 있어 즐겁고 행복했습니다. 마지막으로 멀리서 늘 응원과 사랑을 아까지 않은 부모님, 할아버지, 할머니 감사합니다. 그리고 사랑합니다. 평생 내 친구인 지윤이 언니, 정윤이, 찬우야 고마워~ 끝으로 그 동안 많은 도움을 주신 분들께 감사를 전합니다.